All-optical signal processing using the Kerr effect for fiber-based sensors

Benoit Yvon Eric Vanus

A thesis submitted in partial fulfillment of the requirements for the Doctorate in Philosophy degree in Physics

Ottawa-Carleton Intitute for Physics

Department of Physics
Faculty of Sciences
University of Ottawa

À mon grand-père

Abstract

All-optical signal processing has grown over the last decade due to the demand for high-speed and high-bandwidth data processing. The main objective of all-optical signal processing is to avoid signal conversions from the optical domain to electrical domain and then back to optical, which introduces noise and bottlenecks data transmission speeds. These conversions can be avoided by manipulating light using an optical medium, e.g. an optical fiber, and taking advantage of the nonlinear response of the medium's dipoles to an external electric field. Nonlinear effects arising from the third-order nonlinearities, such as the Kerr effect, allow for an intense light beam to modify the refractive index of a medium through which it propagates. As a consequence, the phase of the light beam changes as it propagates and new frequencies are generated; this phenomenon is referred to as self-phase modulation (SPM). Light's ability to modify not only its own properties but also the properties of other co-propagating beams has been widely applied in telecommunications to create integrated all-optical data regenerators. While optical fibers are mainly utilized to transmit data at extreme speeds, they can also act as sensors when considering the reflected signal as opposed to the transmitted signal. Surprisingly, most of the fiber sensing field relies on electrically-driven components for manipulating light and does not take advantage of all-optical signal processing capabilities.

In this thesis, we demonstrate the use of the nonlinear Kerr effect to improve aspects of both fiber point and distributed sensing. These sensing scenarios respectively refer to the use of a fiber as a single sensing element, and to the detection of external perturbations continuously along the entire length of the fiber. The sensing improvement are obtained by first

inducing a sinusoidal modulation on the light before it experiences self-phase modulation in a nonlinear medium, leading to the generation of optical sidebands. By judiciously adjusting the peak power of the light and extracting a specific sideband, multiple all-optical signal processing functions are achieved.

First, high extinction ratio pulses can be generated by extracting a higher-order sideband, which allows for extending the sensing distance of distributed fiber-based sensors. The extinction ratio refers to the ratio between the pulse peak and pedestal powers. To quantify the generated extinction ratios, we develop a measurement technique based on a single-photon counter and measure a pulse exhibiting a 120 dB extinction ratio, which was originally created by an electro-optic modulator with a 20-dB extinction ratio.

Second, all-optical peak power stabilization can be achieved by extracting the first-order SPM-generated sideband. We utilize this technique to stabilize the peak power of an optical pulse sent to a distributed fiber sensor. We demonstrate that this stabilization technique allows for the detection of applied vibrations that would otherwise remain buried in the background noise.

Third, we demonstrate an all-optical scheme, based on sinusoidally-modulated light experiencing SPM, that enables the magnification of fluctuations in the peak power intensity of a pulsed signal. The light's peak power at the entrance of the nonlinear medium is adjusted to reach a power regime yielding a magnification factor of $2m+1$, when extracting the m^{th}-order SPM-generated sideband.

Finally, we propose a new sensing scheme composed of two all-optical signal processing steps to allow for the detection of environmental perturbations previously too small to be detected by a given intensity-based fiber sensor.

Acknowledgements

I would like to thank my supervisor, Professor Xiaoyi Bao, for giving me the opportunity to pursue a PhD in her research group. With her critical thinking, profound and vast knowledge of physics, she provided me with valuable advices and insights to best pursue my research goals. I will always regard her dedication and true passion for physics, and optical fibers in particular, with great admiration. I would also like to deeply thank Dr. Chams Baker without whom this thesis would not had been possible. His help and guidance both in the lab and in writing are invaluable to me, and I am honoured to now have him as a friend.

While experimental work does not always go your way, I am truly thankful to have been surrounded by incredibly supportive labmates during the last few years, and I would like to thank Dr. Bhavaye Saxena, Dr. Song Gao, Dr. Liang Zhang, Mr. Robert Chutu Li, Mr. Zichao Zhou, Mr. Yuan Wang, Mr. Haiyang Wang, Ms. Wenwen Ma, Mr. Chen Chen and Mr. Ole Krarup.

I would like to acknowledge the support provided by the Ontario Trillium scholarship and the NSERC CREATE SERA program. I thank the program director, Prof. Mark Green from Queen's university, for giving me the opportunity to be involved in the program, as well as Mr. Terry Gerritsen and Ms. Susan Derrah for their support and guidance during my internship with Hatch.

I shall sincerely and profoundly thank Annie Russell, Luc Robichaud, Erin Tonita, Ras-Jeevan Obhi, Gavin Forcade, Kayden Kaller, Clément Estève, Benjamin Wasilewski, Torie Hatfield, Julien Navaux and Myriam Beaudry for their constant support throughout this journey, and for always being there for me during the best and worst of times. I also thank

Erin Flanningan, Alan Godfrey, Spencer Sterling, and Daisy Xia for their time and precious feedbacks.

Last, I would like to thank my family for their support and encouragement. Also, and especially, I would like to thank Geoff and Maree Baker who welcomed me into their family and made me feel at home here in Canada. Meeting them has been one the best thing that has ever happened to me and I will forever be grateful for all they have provided me.

Contents

List of Figures

List of Acronyms

ε	Extinction Ratio.
Φ-OTDR	Phase-sensitive Optical Time Domain Reflectometry.
ΠSG	π-Shifted FBG.
2R	Re-amplifying and Reshaping.
2xEDFA	Dual-stage EDFA.
APC	Angled Physical Contact.
ASE	Amplified Spontaneous Emission.
BPF	Band-Pass Filter.
CW	Continuous Wave.
DC	Direct Current.
DSF	Dispersion-Shifted Fiber.
EDFA	Erbium-Dopped Fiber Amplifier.
EOM	Electro-Optic Modulator.
FBG	Fiber Bragg Grating.
FPI	Fabry-Pérot Interferometer.
FUT	Fibre Under Test.
HG-EDFA	High-Gain EDFA.
HP-EDFA	High-Power EDFA.
KM	Kerr Medium.
MI	Michelson Interferometer.
MZI	Mach-Zehnder Interferometer.
OEO	Optical Electrical Optical.
OSA	Optical Spectrum Analyzer.
OSC	Oscilloscope.
OTDR	Optical Time-Domain Reflectometry.
PBC	Polarization Beam Combiner.
PBS	Polarization Beam Splitter.
PC	Polarization Controller.
PD	Photodetector.
PM	Polarization Maintaining.
PMF	Polarization Maintaining Fiber.
PSD	Power Spectral Density.
QAM	Quadrature-Amplitude Modulation.
SMOS	Sinusoidally-Modulated Optical Signal.
SNR	Signal-to-Noise Ratio.
SPM	Self-Phase Modulation.
UV	Ultraviolet.

Chapter 1

Introduction

The study and understanding of light have had tremendous repercussions on modern society, not only for communications but across all fields of science. The branch of science studying light is called "Photonics", as light is composed of elementary particles named photons. Although their true nature is still to be determined, photons can be seen as packets of energy, commonly referred to as quanta. Photons are known to behave both like a wave and a particle, as demonstrated respectively by Young in the early 1800s and by Einstein a little over 100 years ago [1, 2]. Since then, the generation, propagation and detection of light have been widely investigated. Originally, light was only manipulated using mechanical systems, such as mirrors to change its direction of propagation, lenses to focus or spread it, and shutters to control the intensity of light propagating. Materials and electro-mechanical devices were later engineered to allow for amplifying or attenuating light intensity and filtering certain frequencies (or colours). The invention of lasers, which consistently generate photons in the same direction of propagation with identical frequency, phase and polarization – the three main properties of light, revolutionized the field of photonics and many other fields including material science, chemistry, biology, and the medical domain (laser eye surgery for example). When lasers were combined with optical waveguides (e.g. optical fibers), which intrinsically rely on total internal reflection of light, communication systems became capable of transmitting information at the speed of light.

In our natural desire to always explore further, transmission distances were extended and the signal power had to be increased to combat the natural attenuation occurring when light propagates in a medium. It was soon discovered that not only external devices can manipulate light, but high intensity light can manipulate itself as well as other co- and counter-propagating light beams [3]. This interaction of photons through matter opened a new field of research in photonics called nonlinear optics, which paved the way for all-optical signal processing.

1.1 All-optical signal processing

All-optical signal processing is an area of research at the intersection of nonlinear optics and telecommunications that aims to manipulate signals, such as modulated data streams, in their optical form instead of their electrical form. All-optical signal processing has significantly grown over the last decade due to the increasing demand for high-speed and high-bandwidth data applications and needs for high-speed data processing. The main objective of all-optical signal processing is to avoid the conversion from optical signal to electrical signal and back to the optical domain (OEO conversion). With all-optical signal processing, operations such as signal amplification, bit regeneration, wavelength conversion and signals correlation can be performed all optically and thus significantly increase the speed of the operation compared to their electrical counterparts [4]. By performing data manipulation in the optical domain, the added noise introduced during the OEO conversion is also eliminated. Modern light modulation schemes, such as quadrature-amplitude modulation (QAM), also include phase-modulation on top of the conventional intensity-based and frequency-based modulations. While an OEO conversion can be utilized to regenerate signals and reduce amplitude fluctuations, it usually comes at the expense of phase-noise which limits its practicality with modern light modulation techniques. To allow for higher data transmission rates, narrower pulses with stable frequency, phase and amplitude are required. Moreover, because the trans-

mitted optical information takes the form of picosecond pulses with high repetition rate, in the GHz or THz domain, wide bandwidth photodetectors are required for properly converting light to an electrical signal. However, high repetition rates limit the practical use of electronic equipment to manipulate optical data because the bandwidth of high-speed photodetector and modulators is conventionally below 50 GHz, although a 100-GHz modulator was recently reported [5]. Moreover, the use of high-speed detectors induces either additional phase noise or intensity noise [6]. Therefore, all-optical signal processing is necessary to reliably monitor the performance of a network and allow for higher data rates without the bandwidth and added noise limitations arising from using the electrical domain [4, 7].

Nonlinear phenomena, such as the Kerr effect or Raman and Brillouin scatterings, are usually seen as detrimental in data transmission as they modify the light spectrum and/or change the light's temporal profile. However, most all-optical signal processing schemes are based on nonlinear phenomena with response time of femtoseconds [8], which can thus accommodate modern data transmission rates. All-optical schemes have allowed to regenerate a signal's temporal profile, change an optical signal's frequency profile as well as characterize the properties of a laser source and transmission lines [9]. Schemes based on all-optical intensity limitation can be utilized to restore the shape of an optical pulse and stabilize the light intensity [10]. However, because these schemes commonly rely on the gain saturation of a semiconductor optical amplifier, small-amplitude signal variation cannot be eliminated. The frequency changes induced by nonlinear effects were also advantageously utilized to create copies of a signal while keeping the same data rate [11], to allow for Tb/s transmission [12], to add a tunable pulse delay [13] and to switch between amplitude-based data formats [13]. More complex mathematical functions have also been successfully realized all-optically, such as time differentiation, integration, time reversal of an optical signal, and information storage [14, 15]. As data, in the form of optical pulses, are transmitted through the optical fiber, the light intensity decreases and the temporal profile of the pulses broadens due to attenuation, chromatic dispersion and polarization dispersion. Optical amplifiers are therefore

used to compensate the attenuation but, unfortunately, also introduce a broadband amplified spontaneous emission (ASE) noise on top of the amplified signal, which can distort the signal's temporal profile. Therefore, in-line data regenerators are essential components of optical networks as they can perform pulse re-amplification, reshaping and/or retiming [16]. All-optical regenerators are based on nonlinear effects such as four-wave mixing, stimulated Raman scattering, cross-phase modulation or self-phase modulation (SPM). SPM occurs when a high-intensity beam propagates through a medium and the beam intensity changes the refractive index of said medium. This refractive index modification in turn modifies the phase of the light and eventually broadens (or compresses) the light spectrum proportionally to the light intensity. The advantage of SPM-based regenerators is that no pump or probe light is required and environmental perturbations do not have a significant impact on their performance [16, 17].

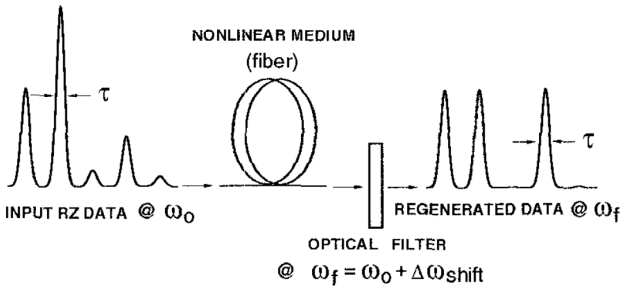

Figure 1.1: 2R regenerator (re-amplifier and reshaper), with ω_0 the initial carrier frequency and ω_f the filtered frequency and τ the pulse width [17].

An example of SPM-based regenerator is shown in Fig. 1.1, where re-amplifying and reshaping (2R) is performed [17]. Self-phase modulation allows for inducing a broadening of the initial signal bandwidth, and the broadening is proportional to the input pulse peak power. If sufficient broadening is induced, the pulse can then pass through a band-pass filter located away from the original central wavelength $\omega_f = \omega_0 + \Delta\omega_{\text{shift}}$, where ω_f is the filter frequency, ω_0 is the initial signal frequency and $\Delta\omega_{\text{shift}}$ is the frequency difference between the ω_f and ω_0. This wavelength-shifted filter removes the noise accumulated by the pulse pedestal since the low power of the pedestal does not induce a sufficient frequency shift at the output of the nonlinear medium to pass through the optical filter. Self-phase modulation can

also be utilized to compensate the dispersions accumulated during a pulse propagation by compressing the pulses using a dispersion-compensation fiber [18]. Because the compression step increases the pulse pedestal, an additional pulse reshaper is necessary to retrieve the original pulse shape and extinction ratio [19]. The pulse extinction ratio (ε) is defined as the ratio of the peak power P_p and pedestal power of the pulse P_Δ, as shown in Fig. 1.2 where T_0 is the pulse width. The pulse ε can be increased in a 2R regenerator by adding an interferometer [20] or by adding an imbalanced nonlinear optical loop mirror [21].

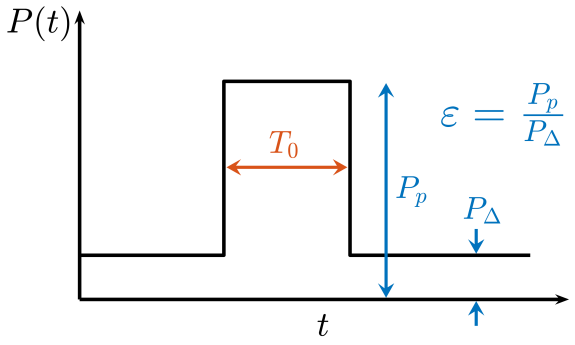

Figure 1.2: Sketch of an optical pulse power profile as a function of time. The sketch illustrates the definition of the pulse extinction ratio $\varepsilon = P_p/P_\Delta$, where P_p is the pulse peak power, P_Δ is the pulse pedestal power and T_0 is the pulse width.

All-optical signal processing has been extensively used in telecommunications but not much in other areas such as sensing. However, all-optical signal processing is a promising tool for optical sensors and particularly for fiber-based sensors as it could allow for overcoming current limitations, such as signal stability and background noise reduction.

1.2 Fiber-based sensors and their limitations

Fiber-based sensors are increasingly utilized due to their many advantages over other types of sensors, such as compactness, immunity to electro-magnetic irradiations, waterproofness and suitability for harsh-condition environments [22–24]. Fiber sensors have been utilized in various fields of research and industries, including in the oil and gas industry for pipeline monitoring [25], in seismology as seismic sensors [26], in medical diagnostics [27] and in the

metal industry for corrosion measurement [28]. Depending on their application, fiber-based sensors can be classified as either point sensors or distributed sensors. Point sensors are defined as using the whole length of the sensing element for a single measurement and are commonly up to a meter long. Distributed sensors allow for measurements to be performed at different locations along the sensing element and usually span distances from several tens of meters to hundreds of kilometers. Both types of sensors are commonly utilized to detect strain, temperature, humidity and acoustic perturbations [29, 30]. A more in-depth analysis of each type of fiber-based sensor that will be utilized later in this thesis is presented in Chap. 2.

While fiber sensors have many advantages and are compatible with the equipment used in the telecommunications world, they suffer from the noises arising from that equipment and from unwanted external perturbations. The noises existing in a fiber-sensing system can be separated into three main categories: detection noise, environmental noise and optical noise. The detection noise can either originate from the electrical power system of the detector or be caused by shot and thermal noises occurring at the detector and the oscilloscope. Electrical noises, arising from carrier fluctuations, are unavoidable with existing technology as light must be converted to an electrical signal to be observed. Small environmental perturbations, such as temperature or strain, also induce intensity and phase noises since they modify refractive index of the fiber proportionally to the amplitude of the perturbation [31–34]. These refractive index changes in turn modify the scattered light temporal profile in a distributed sensor or the interference pattern in a point sensor (see Chap. 2), and become part of the detected background noise. Aside from perturbations generated by nonlinear effects due to the use of high peak powers [35–37], optical noises also arise from the laser source noises. The laser intensity, frequency and phase noises form the base of the noise floor when sensors' responses are collected at the detector. These noises originate in carrier density fluctuations, spontaneous emission in the gain medium, thermal fluctuations, mechanical vibrations and acoustic perturbations occurring within the laser cavity [38].

To mitigate the impact of laser noises, various stabilization techniques have been proposed but mostly rely on external control loops, which in turn tend to increase other laser noises as will be shown in the next few examples. A phase noise compensation system has been proposed [39] and allows to extend the range in distributed sensing by introducing auxiliary interferometers at the cost of impairing the signal-to-noise ratio outside of the interferometer phase-compensation range. Feedback compensation loops are also utilized to reduce intensity noise in semiconductor lasers [40, 41] but rely on introducing another laser signal which hinders the phase and frequency noises of the overall system. Another phase and frequency stabilization technique [42] utilizes a phase modulation on the laser to drive the locking loop controlling the laser current, which allows for laser linewidth reduction. The downside of this technique is that the shot noise of the photodetectors prevents the long-term stability of the system because the noise cannot be distinguished from the loop's response to a small frequency shift. Other more recent examples [43, 44] utilize separate interferometers and data processing to compensate the laser frequency drift but need to use a laser already exhibiting low noises or are limited to short periods of time due to the dependence on the laser's frequency drift direction, thus resulting in an increase of intensity noise. For fiber sensing schemes based on pulsed-light, the extinction ratio of the pulse has to be considered as it directly contributes to the background noise. Indeed, a lower ε introduces a higher pulse pedestal power which can induce a coherent background scattering signal, and be detrimental in both point and distributed sensing [45, 46]. For example, in Brillouin- and Raman-based distributed sensors, the leaked continuous wave (CW) light from the lasers depletes the pump signal and induces extra frequency shifts in the detected spectrum, which in turn decreases the accuracy of strain or temperature measurement [47, 48].

All-optical signal processing has only recently begun to be applied to optical fiber sensing, mostly focusing on frequency-chirped applications [49]. Frequency chirp manipulations are conventionally utilized in telecommunications to generate optical solitons [8], but also proved

to allow for improving the sensitivity of fiber-Bragg grating sensors [50] and increasing the spatial resolution in optical frequency domain reflectometry [51]. The work presented in this thesis aims at extending the capabilities of both point and distributed fiber-based sensors using all-optical signal processing.

1.3 Thesis Contributions

This thesis introduces the use of all-optical signal processing to enhance the performances of a wide range of fiber sensing schemes. We demonstrate that the use of the nonlinear Kerr effect on sinusoidally modulated optical signals (SMOS) allows for the generation of different sensing performance enhancement regimes with very little dependence on the laser and optical components utilized. Moreover, the ultrafast response time of the Kerr effect also allows for potential applications in optical telecommunications. This work presents four fiber sensing applications and advantages of all-optical signal processing using the nonlinear Kerr effect. First, the nonlinear Kerr effect is utilized to generate high-extinction ratio optical pulses based on pulse-shaped SMOS. The predicted theoretical value for the extinction ratio can be as high as 200 dB. To verify such a high value, we provide a technique for characterizing high-ε pulses using a single-photon counting technique, as conventional techniques would not be sufficient. This technique can also allow for the verification of multiple high-extinction ratio claims made in the literature that have not been experimentally verified, such as in reference [52]. Second, we demonstrate an all-optical light-intensity stabilization technique based on the Kerr effect to reduce the peak power fluctuations of nanosecond pulses. This technique allows for the detection of external vibrations applied on a fiber-based distributed sensor which would otherwise be undetectable without intensity stabilization. Third, we present an all-optical technique based on SMOS undergoing SPM to magnify an optical sensor's response to an environmental perturbation. We also demonstrate that a magnification of a factor $2m + 1$ is achievable for small signals, with m being the order of the extracted SPM-generated sideband at the output of the nonlinear medium (see Chap. 3). Fourth, we

propose and demonstrate that a combination of both light stabilization and magnification allows for the detection of environmental perturbations previously undetectable using a given fiber point sensor. As our new sensing scheme is independent from the sensor and detection scheme, it could also be utilized on various fiber point-sensing setups without the need to modify the sensor. Finally, we introduce the possibilities of utilizing SMOS undergoing the Kerr effect to create an intensity-stabilized pulsed laser, and to enhance the event location accuracy in distributed fiber sensing.

1.4 Thesis Outline

This thesis adopts a "*thesis by paper*" format and contains three published (Chap. 4 to 6) and one submitted (Chap. 7) manuscripts. An introduction to each manuscript is provided as well as a link between the different papers. The manuscripts are presented in their published or submitted formats with self-contained references.

Chapter 2 introduces the point and distributed fiber-based sensors utilized in the following chapters.

Chapter 3 introduces the physical description and derivation of sinusoidally modulated optical signals undergoing the nonlinear Kerr effect, and serves as a basis for the following chapters.

Chapter 4 describes a novel technique that allows for the measurement of the extinction ratio of high-ε optical pulses based on single-photon counting.

Chapter 5 demonstrates the intensity stabilization provided by SMOS propagating through a nonlinear medium. External vibrations are applied to two distributed sensing systems with identical parameters and we demonstrate that the vibrations can only be fully recovered utilizing our intensity-stabilized scheme.

Chapter 6 demonstrates the interest of all-optical signal magnification applied to fiber-based sensors and shows that a $2m+1$ magnification factor can be obtained for small signals, with m being the order of the extracted SPM-generated sideband.

Chapter 7 proposes a new sensing schemes composed of two all-optical signal processing steps to allow for the detection of environmental perturbations previously too small to be detected.

Finally, chapter 8 concludes the conducted work and introduces other applications based on SMOS experiencing the nonlinear Kerr effect for future research.

Chapter 2

Fiber-based sensors

In this chapter, we describe fiber-based point and distributed sensors utilized in the later chapters to better understand their behaviour and how all-optical signal processing will be beneficial for improving their performances. The first part of this chapter focuses on an intensity-based point sensor called a polarimetric sensor, as one will be utilized in Chap. 7 to detect strain. The Mueller matrix analysis [53] of this polarimetric sensor is presented to obtain the optical transfer function. As a polarimetric sensor conceptually resembles a Mach-Zehnder interferometer (MZI) and possesses a similar transfer function, we first introduce and demonstrate the cosine-square shaped optical transfer function of an MZI. We also operate the sensor at the quadrature point of the transfer function, defined as a constant phase-bias introduced to place the unperturbed sensor output power at half of its maximum value, to ensure that the measured output power is linearly proportional to the external perturbation. The second part of this chapter introduces distributed sensing and focuses on phase-sensitive optical time domain reflectometry (Φ-OTDR) as vibration will be detected utilizing a Φ-OTDR setup in Chap. 5. While many detection schemes exist in a Φ-OTDR system, we only utilize the conventional direct-direction scheme as performance improvements made utilizing this detection method will, most generally, yield performance improvements in other more complex detection schemes.

2.1 Point sensors

The vast majority of fiber-based point sensors rely on an interferometric mechanism. An exception can be made when detecting power changes due to fiber bending, which can in turn be related to an external displacement [54]. An interferometer is a device forcing light beams to interfere, and was first discovered by Albert A. Michelson at the end of the 19^{th} century. Those light beams can originate from different light sources or from a single source from which they are separated (by a coupler or a beam splitter) and sent down different optical paths, as shown in the conceptual Michelson interferometer (MI) presented in Fig. 2.1. The combination of light beams, generally two beams, generates the apparition of constructive and destructive interference between the respective electric fields. If one of the path lengths of the interferometer is altered, for example by an external perturbation, the arm length is modified which induces a phase change on the light beam propagating through that arm. Thus, once the beams are recombined, the interference pattern observed at the detector changes. Interferometer-based sensors can be utilized to measure environmental perturbations such as strain and temperature [30, 32, 55, 56], but also allow for soil moisture and liquid level detection [57].

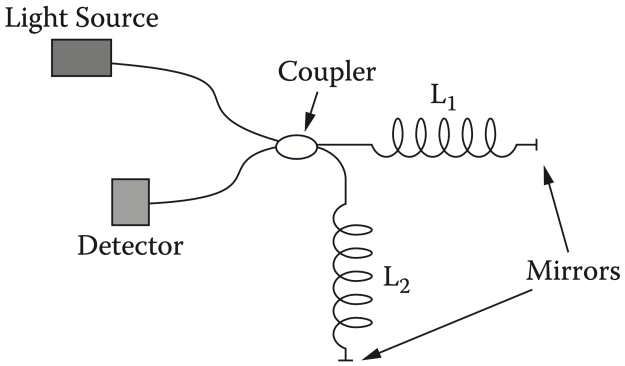

Figure 2.1: Schematic of a Michelson interferometer where an optical coupler separates the light into two arms of lengths L_1 and L_2 respectively. The light is reflected by the mirrors in each arm, propagates back to the coupler where it interferes and is eventually measured by the detector [58].

When using optical fibers, interferometers based on optical mirrors are less common, except for Fabry-Pérot interferometers (FPIs). The interference is commonly generated by

separating light into different fiber-based arms and recombining using two couplers, such as in a Mach-Zehnder interferometer. Another type of interferometer relies on periodic modulation of the fiber's refractive index and is referred to as a fiber-Bragg grating (FBG). The interferences produced by an FBG are observed in the frequency domain, as shown in Fig. 2.2 where the spectrum of the light is illustrated. The reflected wavelength peak of an FBG shifts when the interferometer is subjected to external perturbations [59], which allows for sensing applications. FBGs can also be utilized as optical filters when they remain in a stable environment. FBG-based filters are utilized in the following chapters to prevent certain light frequencies from entering a nonlinear medium.

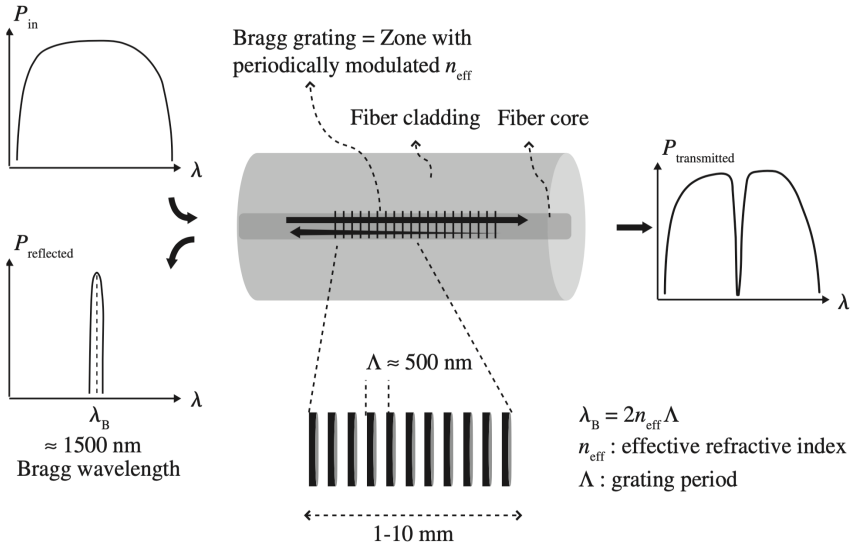

Figure 2.2: Schematic of a fiber Bragg grating and its transmission and reflection spectrum when subjected to an incident broadband light [60]. The refractive index modulation of the fiber core, forming the grating depicted by the black vertical lines, is created using an external phase-mask and shining the fiber with UV light taking advantage of the photosensitivity of fiber at those wavelengths [61]. λ is the wavelength, $P_{\text{in}}, P_{\text{reflected}}$ and $P_{\text{transmitted}}$ are respectively the input, reflected and transmitted power, λ_{B} is the Bragg reflection wavelength, n_{eff} is the effective refractive index of the fiber core and Λ is the grating period.

Because we are focusing on an MZI sensor, we will use a narrow linewidth laser light whose intensity will vary according to the perturbations applied on the sensor. External perturbations occurring on the sensor induce a refractive index change within the fiber as the fiber is stretched and/or compressed, for example by strain. The refractive index changes can either modify the effective cavity length (e.g. in an FPI) or induce additional phase-shifts

between lights propagating through the reference and sensing arms of the interferometer (e.g. in an MZI and MI). This results in a modification of the transmission and reflection spectra, which can be monitored at a specific wavelength to determine the presence of an external perturbation [55, 62]. Figure 2.3 shows a conceptual setup of a Mach-Zehnder interferometer, which will serve as a base for the polarimetric sensor introduced later in this chapter. The coupler located after the laser in Fig. 2.3 splits the signal between the sensing and reference arms of the interferometer. The second coupler recombines the two signals and make them interfere. The output signal of the interferometer is then measured by a photodetector and can be later analyzed to determine whether a perturbation occurred on the sensing arm.

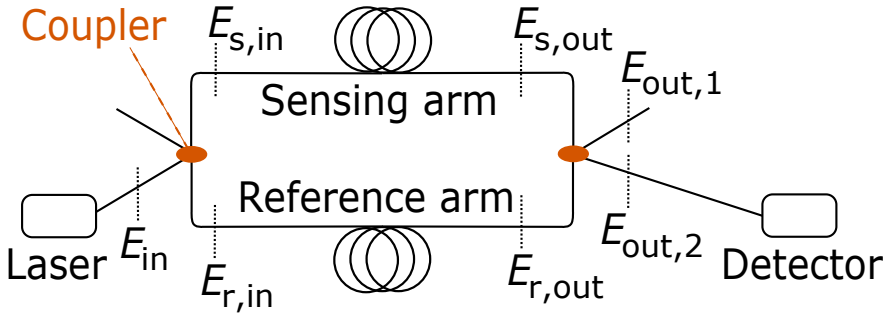

Figure 2.3: Schematic of a Mach-Zehnder interferometer. The interferometer is composed of a reference arm and a sensing arm. The latter is exposed to external perturbations which lead to modifications of the interference pattern measured at the detector. E_{in} is the electric field at the input of the interferometer, $E_{\text{r,in}}$ is the electric field at the input of the reference arm, $E_{\text{s,in}}$ is the electric field at the input of the sensing arm, $E_{\text{r,out}}$ is the electric field at the output of the reference arm, $E_{\text{s,out}}$ is the electric field at the output of the sensing arm, and $E_{\text{out,1}}$ and $E_{\text{out,2}}$ are the electric fields at the outputs of the second coupler, respectively.

We now determine the optical transfer function of an MZI. First defining the phase of a signal as $\phi = nkL = \frac{2\pi}{\lambda}nL$, where n is the refractive index of the medium, L is the propagation length, $k = 2\pi/\lambda$ is the propagation constant and λ is the wavelength. We also express the electric field at the input of the first coupler as $E_{\text{in}} = E_0 e^{i(\omega_0 t+\phi)}$, where E_0 is the amplitude of the field and ω_0 is the frequency of the field. We then assume that when the laser signal reaches the first coupler, an equal amount of power enters each arm. Moreover, we also neglect the attenuation occurring during propagation and at the interface of the optical components. The electric fields at the entrance of the sensing and reference arms of

the MZI presented in Fig. 2.3, respectively $E_{\mathrm{s,in}}$ and $E_{\mathrm{r,in}}$, can be expressed as [63, 64]

$$\begin{bmatrix} E_{\mathrm{s,in}} \\ E_{\mathrm{r,in}} \end{bmatrix} = \mathbf{C} \begin{bmatrix} E_{\mathrm{in}} \\ 0 \end{bmatrix} = \begin{bmatrix} \sqrt{1-\sigma} & i\sqrt{\sigma} \\ i\sqrt{\sigma} & \sqrt{1-\sigma} \end{bmatrix} \begin{bmatrix} E_{\mathrm{in}} \\ 0 \end{bmatrix} = \frac{1}{\sqrt{2}} \begin{bmatrix} 1 & i \\ i & 1 \end{bmatrix} \begin{bmatrix} E_{\mathrm{in}} \\ 0 \end{bmatrix} = \frac{1}{\sqrt{2}} \begin{bmatrix} E_{\mathrm{in}} \\ iE_{\mathrm{in}} \end{bmatrix}, \tag{2.1}$$

where $\mathbf{C}$ is the transfer matrix of a coupler, and σ is the splitting ratio between the two arms of the coupler. Conventionally, and in our experiments, the input laser signal is equally split between the two arms of the interferometer, leading to $\sigma = 0.5$. Using Eq. 2.1, the electric fields at the end of each arm can be expressed as

$$\begin{bmatrix} E_{\mathrm{s,end}} \\ E_{\mathrm{r,end}} \end{bmatrix} = \mathbf{D} \begin{bmatrix} E_{\mathrm{s,in}} \\ E_{\mathrm{r,in}} \end{bmatrix} = \begin{bmatrix} e^{i\phi_{\mathrm{s}}} & 0 \\ 0 & e^{i\phi_{\mathrm{r}}} \end{bmatrix} \begin{bmatrix} E_{\mathrm{s,in}} \\ E_{\mathrm{r,in}} \end{bmatrix} = \frac{1}{\sqrt{2}} \begin{bmatrix} E_{\mathrm{in}} e^{i\phi_{\mathrm{s}}} \\ iE_{\mathrm{in}} e^{i\phi_{\mathrm{r}}} \end{bmatrix}, \tag{2.2}$$

where $\mathbf{D}$ is the propagation transfer matrix, ϕ_{s} is the additional phase accumulated in the sensing arm, ϕ_{r} is the additional phase accumulated in the reference arm, and $E_{\mathrm{s,end}}$ and $E_{\mathrm{r,end}}$ are the electric fields at the end of the sensing and reference arms, respectively. Using Eq. 2.2 and the expression of $\mathbf{C}$ from Eq. 2.1, we can express the fields at the outputs of the second coupler in Fig. 2.3 as

$$\begin{bmatrix} E_{\mathrm{out,1}} \\ E_{\mathrm{out,2}} \end{bmatrix} = \mathbf{C} \begin{bmatrix} E_{\mathrm{s,end}} \\ E_{\mathrm{r,end}} \end{bmatrix} = \frac{1}{\sqrt{2}} \begin{bmatrix} 1 & i \\ i & 1 \end{bmatrix} \frac{1}{\sqrt{2}} \begin{bmatrix} E_{\mathrm{in}} e^{i\phi_{\mathrm{s}}} \\ iE_{\mathrm{in}} e^{i\phi_{\mathrm{r}}} \end{bmatrix} = \frac{1}{2} E_{\mathrm{in}} \begin{bmatrix} e^{i\phi_{\mathrm{s}}} - e^{i\phi_{\mathrm{r}}} \\ ie^{i\phi_{\mathrm{s}}} + ie^{i\phi_{\mathrm{r}}} \end{bmatrix} = iE_{\mathrm{in}} \begin{bmatrix} e^{i\phi_{\mathrm{D}}} \sin\left(\frac{\phi_d}{2}\right) \\ e^{i\phi_{\mathrm{D}}} \cos\left(\frac{\phi_d}{2}\right) \end{bmatrix},$$

with $\phi_{\mathrm{D}} = (\phi_{\mathrm{s}} + \phi_{\mathrm{r}})/2$ being the average accumulated phase, $\phi_d = \phi_{\mathrm{s}} - \phi_{\mathrm{r}}$ being the difference between the accumulated phases along the optical paths of the interferometer, and $E_{\mathrm{out,1}}$ and $E_{\mathrm{out,2}}$ respectively being the output fields in the first and second output arms of the second coupler in Fig. 2.3. Because the detector is only connected to one of second coupler's output arm, the detected power can be written as

$$P_{\mathrm{out}} = P_{\mathrm{in}} \cos^2\left(\frac{\phi_d}{2}\right), \tag{2.3}$$

assuming that the effective area A_{eff} over which the signal intensity spreads throughout the sensing setup remains constant, with $P_{\text{in}} \propto |E_{\text{in}}|^2/A_{\text{eff}}$ being the power of the light entering the interferometer, and $P_{\text{out}} = |E_{\text{out},2}|^2/A_{\text{eff}}$ being the power of the light reaching the detector.

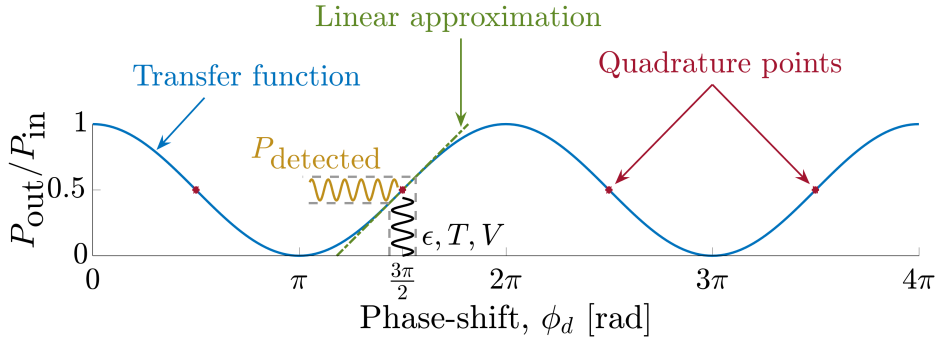

Figure 2.4: Transfer function of an interferometric intensity-based sensor, with P_{out} being the output power of the sensor, P_{in} being the input power. The measured phase-shift variations are induced by strain ϵ, temperature T or voltage V changes applied on the sensor. A linear approximation of the transfer function is shown in dashed green line, and is performed around a quadrature point marked in red.

The cosine-squared transfer function of an MZI is shown in Fig. 2.4. As depicted by the linear approximation in dashed green line, the measured light power variations are linearly proportional to the phase-shifts induced by external perturbations if the interferometer is operated at the quadrature point. When operating at the quadrature point, the output power of the interferometric sensor can be expressed as

$$P_{\text{out}} = P_{\text{in}} \cos^2\left(\frac{\phi_d}{2}\right) = \frac{1}{2}P_{\text{in}}\left[1 + \sin\left(\Delta\phi_d\right)\right] \approx \frac{1}{2}P_{\text{in}}\left(1 + \Delta\phi_d\right), \tag{2.4}$$

for $|\Delta\phi_d| < 0.1$, where $\phi_d = \Delta\phi_d \pm (\pi/2) + 2l\pi$, with l being an integer. As external strain $\Delta\epsilon$ is applied on an MZI-like sensor in Chap. 7, we express the phase difference at the output of the sensor under small strain perturbations $\phi_{d,\Delta\epsilon} = \phi_{d,0} + \Delta\phi_{d,\Delta\epsilon} + 2l\pi$, where $\phi_{d,0}$ is the initial phase difference between the arms of the unperturbed interferometer and is equal to $\pm(\pi/2)$ at the quadrature points, and $\Delta\phi_{d,\Delta\epsilon}$ is the additional strain-induced phase difference between the interferometer's arms. The relationship between the strain-induced phase difference and an externally applied strain is expressed as

$$\Delta\phi_{d,\Delta\epsilon} = \phi_{d,\Delta\epsilon} - \phi_{d,0} = k\left(L\frac{\partial n_d}{\partial\epsilon}\Delta\epsilon + n_d\frac{\partial L}{\partial\epsilon}\Delta\epsilon\right) = \phi_{d,0}\left(\frac{\partial n_d}{\partial\epsilon}\frac{1}{n_d} + \frac{\partial L}{\partial\epsilon}\frac{1}{L}\right)\Delta\epsilon = \phi_{d,0}\theta_\epsilon\Delta\epsilon, \tag{2.5}$$

where $\phi_{d,\Delta\epsilon}$ is the measured phase difference under strain, L is the length of the interferometer arms, n_d is the refractive index difference between the arms and $\theta_\epsilon = \left(\frac{\partial n_d}{\partial\epsilon}\frac{1}{n_d} + \frac{\partial L}{\partial\epsilon}\frac{1}{L}\right)$. Based on Eq. 2.5, the induced-phase difference is proportional to the applied strain. Therefore, when operating around the quadrature point, the output power variation of an MZI is proportional to the applied strain.

The point sensor utilized in Chap. 7 is a polarimetric fiber sensor. This type of sensor uses the high birefringence existing in polarization maintaining (PM) fibers to create a phase shift between the sensor's paths. Birefringence is defined as the dependence of the refractive index to the polarization of light propagating through the medium. Birefringence is expressed as the difference between the propagating constants of the medium's principal modes of polarizations $\Delta\beta = |\beta_x - \beta_y| = k|n_x - n_y| = k|\Delta n|$, where $\Delta n = n_x - n_y$ is the refractive index difference between the two principal axes (x and y) and is referred to as the degree of birefringence [65]. A PM fiber typically exhibits a degree of birefringence on the order of 5×10^{-4} while it is only on the order of 10^{-7} for a standard single-mode fiber [60]. Thus, in a birefringent medium, lights with different polarization states will travel at different velocities, leading to a phase shift between them as they propagate; and eventually leading to what is known as polarization dispersion. While birefringence in standard single mode fibers is low and varies randomly along the fiber, PM fibers exhibit a higher birefringence due to the added stress rods, made out of doped silica, inserted alongside the fiber core, as depicted in Fig. 2.5. A PM fiber therefore exhibits two main polarization axis and has for property that a linearly-polarized light sent with its polarization aligned with a principal axis will preserve its state of polarization when propagating.

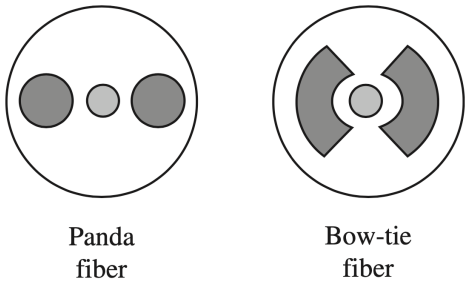

Figure 2.5: Examples of polarization-maintaining fibers where the fiber core is at the center and the two added stress rods are illustrated by the darker areas around the core [60].

A polarimetric sensor is composed of a two-arm interferometer where each arm corresponds to a principal polarization axis of a PM fiber. An intensity-based sensor is created when the PM fiber is placed between two crossed polarizers [66]. A simplified sensing setup depicting the polarimetric sensor utilized later in this thesis is shown in Fig. 2.6. A laser light is sent to a polarization controller (PC) which aligns the light's polarization with the perpendicular axis of the following polarization beam splitter (PBS). A PBS is a crystal-based device, connected with PM fibers in this fiber-based setup, that allows for the decomposition of the light polarization into two perpendicular components, respectively referred to as perpendicular $\perp$ and parallel $/\!/$ polarizations [67, 68]. The crystal in use is birefringent and thus exhibits different refractive indices for the $\perp$ and $/\!/$ components of the input light, which allows for spatially separating those components at the output of the crystal and sending each component into a different output PM fiber.

In the setup presented in Fig. 2.6, the light is sent into the PBS by the perpendicular arm; the PBS can therefore be seen as a polarization beam combiner for the forward propagating light instead of a splitter. The polarized light then exits the PBS by the common port and reaches a 45°-angled splice which splits the power evenly between the two principal polarization axes of the PM sensing fiber. The light then propagates down the PM sensing fiber, is reflected at the end facet due to Fresnel reflection, and propagates back towards the 45°-angled splice. Light from each polarization axis of the sensor then reaches the PBS at a 45° angle, and the part align with the parallel axis of the PBS is transmitted towards the

detector. The power of the parallel component is then detected by a photodetector (PD) and transmitted to an oscilloscope (OSC).

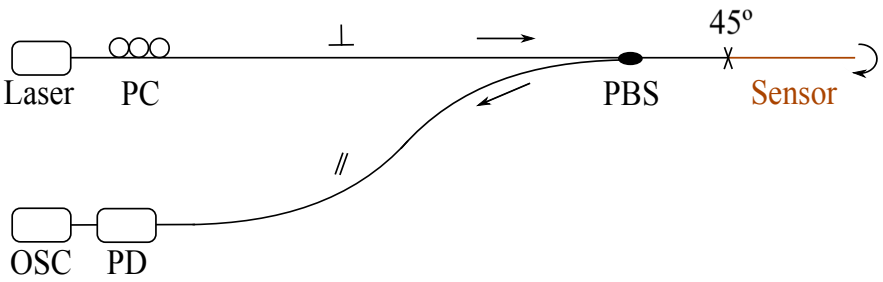

Figure 2.6: Schematic of the polarimetric sensor used in Chap. 7. The ⊥ and // signs respectively refer to polarization alignment of the propagating light with the perpendicular and parallel axis (the two main axis) of the polarizing beam splitter. OSC: Oscilloscope, PBS: Polarization Beam Splitter, PC: Polarization Controller, PD: Photodetector.

The polarization analysis of this sensing setup can be performed by assigning a Mueller matrix to each element modifying the light polarization, and using Stokes vectors to represent the light's polarization [53, 69]. We express the electric field as the sum of the x and y components:

$$\vec{E} = E_x\vec{u}_x + E_y\vec{u}_y = E_{0x}e^{i(\omega t-\beta_x z+\phi_x)}\vec{u}_x + E_{0y}e^{i(\omega t-\beta_y z+\phi_y)}\vec{u}_y,$$

where ϕ_x and ϕ_y are respectively the phases of the x and y components of the field, and where E_{0x} and E_{0y} are the amplitudes of the x and y components of the electric field, respectively. The corresponding Stokes vector $\mathbf{S}$ can be expressed as [69]

$$\mathbf{S} = \begin{bmatrix} S_0 & S_1 & S_2 & S_3 \end{bmatrix}^t, \tag{2.6}$$

where $S_0 = E_{0x}^2 + E_{0y}^2$ represents the total intensity of the light, $S_1 = E_{0x}^2 - E_{0y}^2$ represents the difference between the linear component of the polarization at 0° and the component at 90°, $S_2 = 2E_{0x}E_{0y}\cos(\phi_x - \phi_y)$ corresponds to the difference between the linear component of the polarization at 45° and the component at −45°, and $S_3 = 2E_{0x}E_{0y}\sin(\phi_x - \phi_y)$ corresponds to the difference between the right- and left-handed circular components of the polarization. In our case, the Mueller formalism [70] is chosen over the Jones formalism [71] to describe

the polarization of the light propagating through the setup shown in Fig. 2.6. While the Jones formalism is widely used with coherent light as it retains the phase information, the Mueller formalism is more adapted to our analysis because it focuses on phase differences, and the S_1 parameter in Eq. 2.6 directly relates to the measurement being performed in the setup presented in Fig. 2.6. Moreover, a Mueller matrix $\mathbf{M}$ can be obtained from a Jones matrix $\mathbf{J}$ using [72]

$$\mathbf{M} = \mathbf{A}\left(\mathbf{J} \otimes \mathbf{J}^*\right)\mathbf{A}^{-1},$$

where $\otimes$ is a direct product, and

$$\mathbf{A} = \begin{bmatrix} 1 & 0 & 0 & 1 \\ 1 & 0 & 0 & -1 \\ 0 & 1 & 1 & 0 \\ 0 & -i & i & 0 \end{bmatrix}$$

Using the setup presented in Fig. 2.6, the polarization controller aligns the polarization with the perpendicular axis of the PBS and the input stokes vector can therefore be written as

$$\mathbf{S}_{\text{in}} = \begin{bmatrix} 1 & -1 & 0 & 0 \end{bmatrix}^t.$$

The Mueller matrices for the 45-degree splice $\mathbf{M}_{45}$, the PBS extracting the parallel component $\mathbf{M}_{\parallel}$, the propagation along the sensor $\mathbf{M}_{\text{s}}$ and the reflection $\mathbf{R}$ are respectively expressed as [60]

$$\mathbf{M}_{45} = \frac{1}{2}\begin{bmatrix} 1 & 0 & 1 & 0 \\ 0 & 0 & 0 & 0 \\ 1 & 0 & 1 & 0 \\ 0 & 0 & 0 & 0 \end{bmatrix}, \mathbf{M}_{\parallel} = \frac{1}{2}\begin{bmatrix} 1 & 1 & 0 & 0 \\ 1 & 1 & 0 & 0 \\ 0 & 0 & 0 & 0 \\ 0 & 0 & 0 & 0 \end{bmatrix},$$

$$\mathbf{M}_{\mathrm{s}} = \begin{bmatrix} 1 & 0 & 0 & 0 \\ 0 & 1 & 0 & 0 \\ 0 & 0 & \cos\left(\frac{2\pi}{L_B} L_{\mathrm{s}}\right) & -\sin\left(\frac{2\pi}{L_B} L_{\mathrm{s}}\right) \\ 0 & 0 & \sin\left(\frac{2\pi}{L_B} L_{\mathrm{s}}\right) & \cos\left(\frac{2\pi}{L_B} L_{\mathrm{s}}\right) \end{bmatrix},$$

$$\mathbf{R} = \left(\frac{n-1}{n+1}\right)^2 \begin{bmatrix} 1 & 0 & 0 & 0 \\ 0 & 1 & 0 & 0 \\ 0 & 0 & -1 & 0 \\ 0 & 0 & 0 & -1 \end{bmatrix},$$

with n being the refractive index of PM fiber core, L_{s} is the sensor length and L_B is the beat length of the PM fiber utilized as a sensor. The beat length represents the length after which a polarization state has returned to its original state, and can be expressed as $L_B = 2\pi/\Delta\beta$, with $\Delta\beta = \Delta n\,(\omega/c)$ being the difference of propagation constant between the x and y polarized modes of the PM fiber (or two principal polarization axis of the fiber). A graphical interpretation of the beat length is shown in Fig. 2.7.

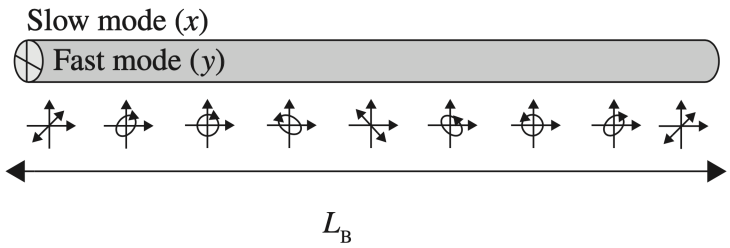

Figure 2.7: Illustration of the beat length L_B [60], where the two perpendicular axes are the main polarization axes of the fiber (x and y) and the other curve represents the state of polarization of the light as it propagates along the fiber.

The Stokes vector of the light reaching the photodetector in Fig. 2.6 can therefore be expressed as

$$\begin{aligned}\mathbf{S}_{\text{out}} &= \mathbf{M}_{\parallel}\mathbf{M}_{-45}\mathbf{M}_{\text{s}}\mathbf{R}\mathbf{M}_{s}\mathbf{M}_{45}\mathbf{S}_{\text{in}} \\ &= \frac{1}{8}\left(\frac{n-1}{n+1}\right)^2 \begin{bmatrix} 1+\cos^2\left(\frac{2\pi}{L_B}L_{\text{s}}\right)-\sin^2\left(\frac{2\pi}{L_B}L_{\text{s}}\right) \\ 1+\cos^2\left(\frac{2\pi}{L_B}L_{\text{s}}\right)-\sin^2\left(\frac{2\pi}{L_B}L_{\text{s}}\right) \\ 0 \\ 0 \end{bmatrix} = \frac{1}{4}\left(\frac{n-1}{n+1}\right)^2 \begin{bmatrix} \cos^2\left(\frac{2\pi}{L_B}L_{\text{s}}\right) \\ \cos^2\left(\frac{2\pi}{L_B}L_{\text{s}}\right) \\ 0 \\ 0 \end{bmatrix},\end{aligned} \tag{2.7}$$

where $\mathbf{M}_{-45}$ is equivalent to $\mathbf{M}_{45}$ with opposite off-diagonal elements [60]. To draw a comparison between a polarimetric sensor and an MZI, we express the content of the cosine squared in Eq. 2.7 as

$$\frac{2\pi}{L_B}L_{\text{s}} = L_{\text{s}}\Delta\beta = L_{\text{s}}\Delta n\frac{\omega}{c} = kL_{\text{s}}\Delta n = kL_{\text{s}}n_x - kL_{\text{s}}n_y = \phi_x - \phi_y. \tag{2.8}$$

The phase difference in Eq. 2.8 is equivalent to the phase difference $\phi_d/2$ in the cosine squared term of Eq. 2.3. Therefore, the previous derivation for the strain-induced additional phase difference between the arms of an MZI can be utilized with a polarimetric sensor. The measured output power is thus proportional to the applied strain when the sensor is operated at the quadrature point. This particular type of polarimetric sensor presented in Fig. 2.6 will be utilized in Chap. 7 to demonstrate minimum detectable strain enhancement.

2.2 Distributed sensing

As opposed to point sensing, distributed fiber sensing allows for the detection of perturbations along the entire length of the Fiber Under Test (FUT– also referred to as sensing fiber). Distributed fiber sensing is commonly utilized for railway monitoring [73], structural health monitoring of buildings [29, 74], as well as in medical application [75]. A more recent application gaining traction is distributed acoustic sensing, which allows for the detection of

ultrasounds [76–78], typically produced when a crack occurs in a structure. Distributed sensing utilizes scattering mechanisms occurring as light propagates down an optical fiber and interacts with the glass medium. The main scattering mechanisms differ in their frequency shift with respect to the initial light frequency, as shown in Fig. 2.8.

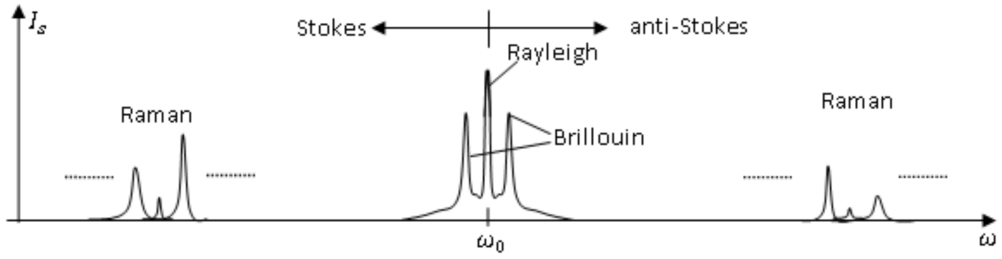

Figure 2.8: Typical spontaneous scattering spectrum from solid state matter [30]. Brillouin scattering typically exhibits a 10 GHz frequency shift in a standard optical fiber while Raman scattering exhibits a 13 THz shift in a standard fiber.

Brillouin and Raman scattering involve a frequency shift respectively peaking around 10 GHz and 13 THz in silica fibers [30], and are induced by acoustic waves present at thermal equilibrium and by molecular vibrations, respectively. Brillouin scattering was reported to allow for simultaneous strain and temperature distributed measurements [79], as well as long-distance distributed sensing (over 100 km) when amplified [80, 81]. Raman scattering also allows for long distance distributed sensing and was reported to enable event detection on a 175 km-long fiber under test when amplified [82]. The most common scattering phenomenon, and the one of interest in this thesis, is Rayleigh scattering. Rayleigh scattering occurs when the light interacts with particles much smaller than the light's wavelength λ, typically less than $\lambda/15$ [83]. As the light propagates through a medium, its electric field induces time-dependent oscillating dipoles, which in turn generate a scattered electromagnetic field. Local density fluctuations along the fiber are induced by imperfections existing within the optical fiber structure, which arise from the presence of dopants and from the fabrication process. These density fluctuations allow for the scattered light to propagate in every direction [60, 83], and therefore to propagate backward towards the light source, as depicted in Fig. 2.9. The backward propagating light can be detected, which allows for distributed sensing if time

information can be retrieved, for example when using a pulsed or frequency-swept input light.

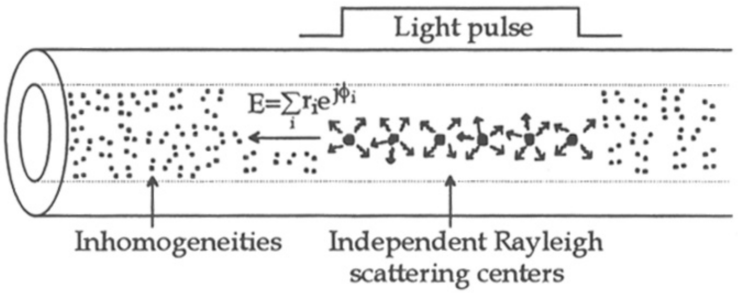

Figure 2.9: Schematic of Rayleigh scattering in optical fibers for a pulsed-light [84]. The amplitude of the backscattered electric field, with a unitary input electric field, is expressed as $E = \sum_i r_i e^{j\phi_i}$, where i scattering centers are present within the pulse, r_i is the reflection coefficients of the scattering center i and ϕ_i is the phase-shift induced by the scattering center i.

In a standard single-mode fiber, Rayleigh scattering is the main source of loss at wavelengths around 1550 nm, but it also generates the strongest back-propagating signal among the aforementioned scattering mechanism (without considering the stimulated cases of Brillouin and Raman scattering), as shown in Fig. 2.8. Rayleigh-based distributed sensing schemes are commonly based upon Optical Time-Domain Reflectometry (OTDR) and allow for temperature [85, 86], strain [87, 88] and vibration detection [89, 90] along the sensing fiber. Figure 2.10 shows an OTDR setup where a broadband laser light is pulse-modulated using an electro-optic modulator.

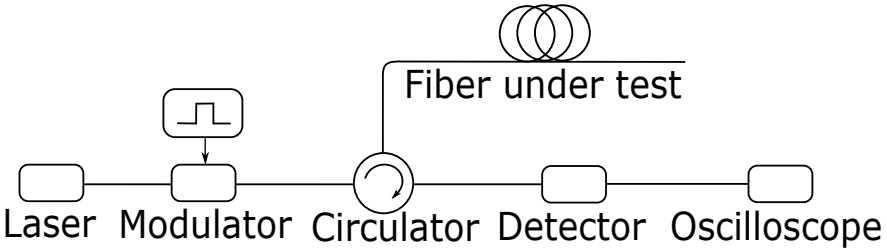

Figure 2.10: Schematic of a conventional OTDR setup, where the circulator allows for the laser signal to be launched into the fiber under test but prevents the backscattering for traveling back to the laser. Instead, the circulator deviates the backscattering of the fiber under test towards the detector.

Electro-optic modulators are usually based on a lithium niobate crystal due its high linear

electro-optic coefficient α_{EO} [91], which describes the change of refractive index $\Delta n = \alpha_{\text{EO}} E$ induced by an externally-applied electric field E. The phase-shift applied to the light passing through the crystal by an external voltage V is given by $\phi(V) = \alpha_{\text{EO}} k V L_e / d$, where L_e is the length of the electrodes applying the voltage difference and d is the distance between the electrodes [92]. The induced phase-shift is then converted into an amplitude modulation by placing the crystal in one arm on an MZI. The transfer function of an EOM therefore takes the form of a cosine squared, as shown in Fig. 2.4, and the point of operation (or initial phase shift) is determined using an external DC bias voltage. The operation point is adjusted to match the bottom end of the linear regime (presented in dashed green line in Fig. 2.4) and the maximum input voltage is adjusted to match the maximum point of the linear regime to avoid creating temporal distortions between the applied voltage shape and the generated optical signal. After the light is pulse modulated by the EOM in Fig. 2.10, the pulse is sent through a fiber under test using a circulator. A circulator is composed of polarization beam splitters, a half-wave plate and a faraday rotator [92] which allow to guide, in accordance with Fig. 2.10, the light from the laser towards the FUT and the backscattered light from the FUT towards the detector. The signal is then detected by a photodetector and acquired by an oscilloscope.

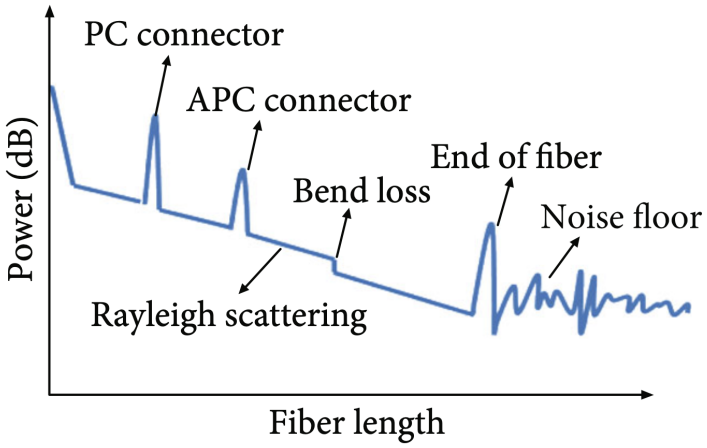

Figure 2.11: Typical OTDR trace obtained by launching a pulsed light into a fiber under test [93]. The power profile allows for the detection of connectors (PC: Physical Contact, APC: Angled Physical Contact), bending losses, and Fresnel reflections occurring at the end of the fiber under test.

A typical OTDR trace is shown in Fig. 2.11 where the slope of the linearly decreasing parts represents the attenuation of the fiber under test, which is usually around 0.2 dB/km[1] at 1550 nm in conventional single-mode fibers [94]. The backward propagating scattered signal allows for perturbation detection and location along the fiber, as shown in Fig. 2.11. The signal acquired by the oscilloscope, conventionally referred to as "trace", is initially in the time domain and can be converted to distance using the known speed of light in the fiber, as the value of fiber core's refractive index is $n = 1.46$. We express the electric field amplitude after the pulse reaches a distance z as $A(z) = A_{\text{in}} e^{-j\beta z - 0.5\alpha z}$, with A_{in} being the amplitude of the input electric field, $\beta = nk$ being the propagation constant, $k = 2\pi/\lambda$ being the wavenumber and α being the attenuation coefficient applied by the optical fiber to the power of the light propagating through at the wavelength of operation. At point z along the fiber, the light is scattered due to Rayleigh scattering and the amplitude of the reflected signal is given by:

$$A_{\text{r}}(z) = \alpha_{\text{R}}(z)\, S(\lambda, z) A_{\text{in}} e^{-j\beta z - 0.5\alpha z},$$

where $\alpha_{\text{R}} \propto \frac{1}{\lambda^4}$ is the attenuation coefficient caused by Rayleigh scattering which varies along the fiber due to the inhomogeneities present in the fiber [95], and $S(\lambda, z)$ is the backscattering capture coefficient. For a single-mode step index fiber, we can express this coefficient as $S(\lambda, z) \simeq \frac{1}{m}\left(1 - \frac{n_2^2}{n_1^2}\right)$, with n_1 and n_2 being the core and the cladding refractive indices respectively, and m being a coefficient function of the fiber refractive index profile ($m \approx 4.55$ for step-index single mode fiber) [96]. We define $\alpha_{\text{s}}(z) = S(\lambda, z)\alpha_{\text{R}}(z)$ to express the field amplitude of the backscattered light at the input end of of the fiber under test ($z = 0$) as

$$A_{\text{BS}} = \alpha_{\text{s}}(z)\, A_{\text{in}} e^{-j2\beta z - \alpha z}.$$

[1]The decibel [dB] will be the unit of reference in this thesis when referring to power ratios or power differences; $X[\text{dB}] = 10\log_{10}\frac{Y[\text{r.u.}]}{1[\text{r.u.}]}$, with r.u. being the reference unit, Y being the value in reference unit and X the value in decibel.

For a square pulse with a duration of T_0, the total electric field amplitude reflected from point z is given by

$$A_{\mathrm{BS,pulse}}(z) = \int_{z}^{z+0.5W} \alpha_{\mathrm{s}}(\zeta) A_{\mathrm{in}} e^{-j2\beta\zeta - \alpha\zeta} d\zeta \tag{2.9}$$

where $W = T_0 v_g = T_0 c/n_g$, v_g is the group velocity, and $n_g = n(\omega) + \omega\frac{\partial n}{\partial \omega}$ is the group refractive-index of the light propagating in the fiber, and ω is the frequency of operation. The integral in Eq. 2.9 is performed over a length of $W/2$ since only the backscattered fields within a half pulse width lead to backscattered signals reaching the detector at the same time t corresponding to the location z [60, 97]. We finally obtain that the magnitude of the backscattered electric field, when expressing the time and position dependence of β, is

$$\left|A_{\mathrm{BS,pulse}}(t,z)\right| = \alpha_0 \left| \int_{z}^{z+0.5W} A_{\mathrm{in}} e^{-j2\beta(t,\zeta)\zeta - \alpha\zeta} d\zeta \right|, \tag{2.10}$$

where we assumed that the Rayleigh backscattering amplitude is constant throughout the fiber $|\alpha_{\mathrm{s}}(\zeta)| = \alpha_0$.

When the coherence length, defined as the distance after which the temporal coherence function of a light beam has dropped by $1/e$, of the laser utilized in an OTDR setup is longer than the length of the pulse propagating down the fiber, the detected signal results from the coherent addition of the electric fields generated by the scattering centers located within the pulse width. The coherence length can be expressed as $L_c = c/(\pi\Delta\nu)$, with c being the speed of light, and $\Delta\nu$ being the laser linewidth. An OTDR system utilizing a highly coherent light source is referred to as a phase-sensitive OTDR (Φ-OTDR) [98, 99], and a typical Φ-OTDR trace is shown in Fig. 2.12. The y axis of Fig. 2.12 represents the voltage measured by the photodetector which is proportional to the incident optical power.

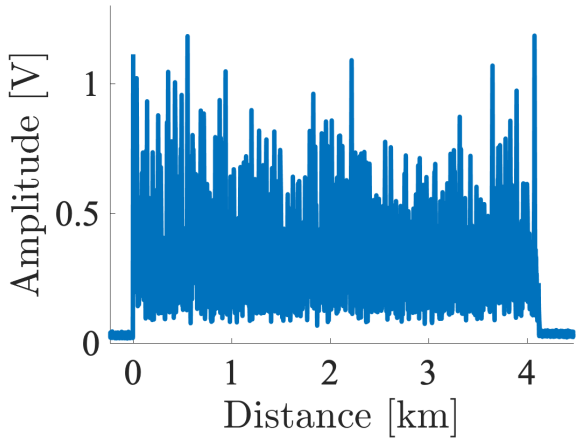

Figure 2.12: Typical Φ-OTDR trace captured by an oscilloscope and converted to distance. The trace results from the relative phase difference of the light scattered by the scattering centers located within the pulse width, as expressed in Eq. 2.12.

In a Φ-OTDR system, the fiber under test can be modelled as a series of N sections of length ΔL, composed of M distinct scattering centers exhibiting the same scattering coefficient r [100], as shown in Fig. 2.13. The Rayleigh backscattered electric field at a

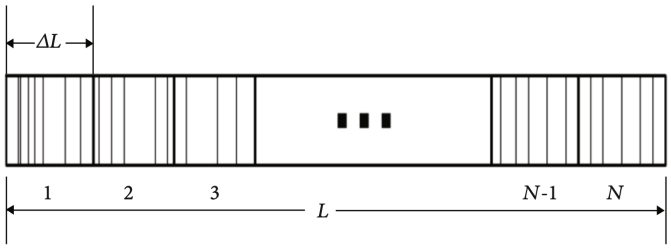

Figure 2.13: Schematic of the fiber under test of length L in a Φ-OTDR system, separated into N segments of length ΔL each containing M scattering centers [93].

distance $L_i = i\Delta L$ can be expressed as [93]

$$E_b^i = rE_0 e^{-\alpha L_i} \sum_{k=1}^{M} e^{j\phi_k}, \tag{2.11}$$

where we assume that the amplitude of the Rayleigh backscattering is equal throughout the fiber, and where ϕ_k is the phase of the k^{th} reflection center within the half pulse width. The detected signal intensity can thus be expressed as [97, 101]

$$I_b^i \propto \left|E_b^i\right|^2 = \sum_{k=1}^{M-1} \sum_{l=k+1}^{M} E_0^2 r e^{-2\alpha i \Delta L} + 2E_0^2 r^2 \sum_{k=1}^{M-1} \sum_{l=k+1}^{M} \cos\left(\phi_l - \phi_k\right). \tag{2.12}$$

The first term in Eq. 2.12 is a DC component and the second term represents the interference of the scattering centers within half of the pulse width. The intensity of a Φ-OTDR trace thus depends on the relative phase difference between scattering centers. The random nature of the scattering centers distribution leads to a detected trace exhibiting a seemingly random profile, as shown in Fig. 2.12. However, this trace is stable over time if no external perturbation occurs on the fiber, assuming that the laser noises are negligible and that a direct-detection scheme is used, as shown in Fig. 2.10. Amplitude fluctuations can still occur on the trace if the detection scheme superposes the electric fields of the initial laser signal with the backscattered signal, thus creating a so-called coherent detection scheme. In that case, the random birefringence of the fiber under test changes the polarization of the backscattered signal which, when interfering with the laser light, leads to random fluctuations of the measured power [89, 101].

When a perturbation occurs on the fiber, such as stress or temperature changes, the local refractive index changes because the density of the medium is modified. This in turn modifies the location of the scattering centers and thus the local phase of the backscattered signal. The phase variation translates into an intensity variation that can be observed at the detector. To determine the location of the event in a Φ-OTDR system, one can compute the difference between the acquired trace containing the perturbation and the original unperturbed Φ-OTDR trace, as shown in Fig. 2.14. Φ-OTDR also allows for the detection of multiple events along a fiber under test. Indeed, because the measured trace consists of relative phases between fiber sections, the intensity of the trace at locations farther than the perturbation remains stable. Different events occurring on the fiber under test can be successfully detected if the events are separated by a distance higher than the spatial resolution of the system. The spatial resolution of OTDR-based systems is defined as the minimum

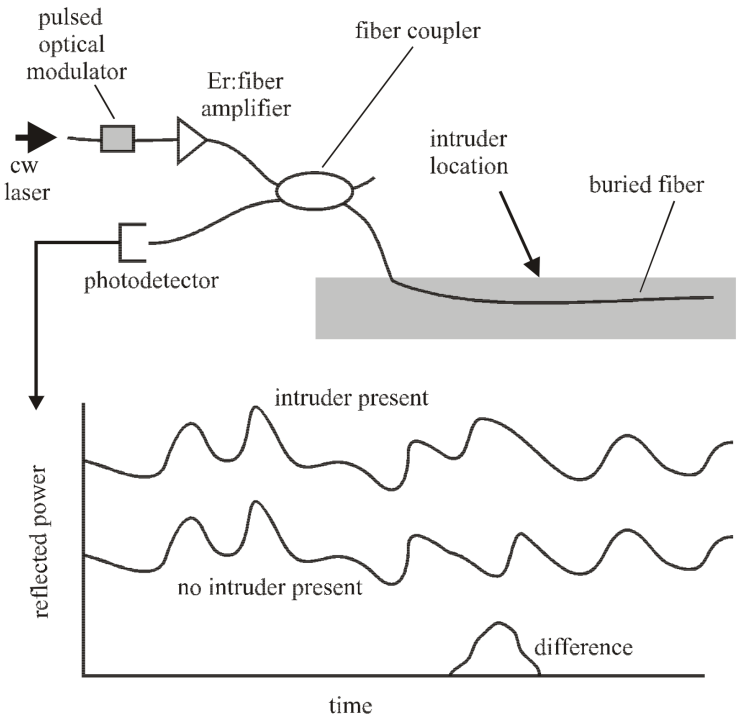

Figure 2.14: Phase-sensitive OTDR schematic intrusion system [26], where the strain applied on the fiber applied by the intruder changes the backscattered trace profile. Calculating the difference between the reference and the perturbed traces allows to determine the position of the intruder. The interrogating setup is similar to the one presented in Fig. 2.10 with a narrow linewidth laser.

distance between two distinguishable events, and expressed as $\Delta z = cT_0/2n$, where T_0 is the pulse width; for instance, a 10 ns pulse has approximately a 1 m spatial resolution in a standard single-mode fiber. Given the expression of the spatial resolution, one might simply want to decrease the pulse width to allow for higher spatial resolution (smaller Δz), but there is an inherent limitation to reducing the pulse width, which ultimately results in a detection performances tradeoff. While decreasing the pulse width increases the spatial resolution, it also decreases the intensity of backscattered signal, as expressed in Eq. 2.9. To compensate for that, one may either increase peak power at the input of the fiber or induce a high amount of amplification on the weak backscattered signal before it reaches the detector. However, increasing the pulse peak power before the pulse reaches the fiber under test leads to nonlinear effects occurring in the fiber under test. The amplification of the backscattered signal is not shown in the conceptual setup presented in Fig. 2.10, but is always present in practice

given that the backscattered power can be 40 to 60 dB lower than the input peak power, and thus outside of the detection range of conventional photodetectors. Boosting the amount of signal amplification before the detector increases the amplified spontaneous emission (ASE) noise contribution from the amplifier, especially for low input power [102], and thus ultimately increases the detection noise floor [103], which in turn limits the minimum detectable perturbation. Moreover, the amount of amplification applied before the detector must be maintained to a minimum as higher power reaching the detector also increase the shot noise [103], further limiting the minimum detectable perturbation occurring on the fiber. There is therefore a tradeoff between pulse width and input peak power in long distance distributed sensing.

To improve the performances of OTDR and Φ-OTDR systems despite this tradeoff, various light modulation and demodulation schemes have been proposed. For example, coherent detection allowed for a signal-to-noise ratio (SNR) improvement when detecting vibration in Φ-OTDR by mixing part of the original laser signal with the backscattered signal before the latter reaches the photodetector [104, 105]. A polarization diversity scheme was also proposed on top of coherent detection to prevent polarization fading and further increase the SNR by 10 dB [101]. Pulse compression and correlation techniques were also proposed to enhance the spatial resolution of OTDR-based systems [106–108]. Chirped pulse amplification [109] was also combined with Φ-OTDR and allowed to achieve a spatial resolution of 1.8 cm [110], where the conventional spatial resolution of Φ-OTDR is on the order of meters. Fiber Bragg gratings were also introduced in the FUT of a Φ-OTDR [111, 112], and proved to allow for quantitative strain measurement over kilometers when combined with frequency sweeping or interferometer-based detection schemes. More recently, focus has been shifted to the optical pulses' extinction ratios [113] since the backscattering signal in a Φ-OTDR created by the pulse pedestal power induces a background noise at the detection end [46], and can be considered as the noise floor when detecting small perturbations [114]. If an electro-optic modulator is utilized to generate the pulse, the stability of the bias voltage and

the transfer function of the modulator are necessary to minimize the CW power leaked out of the EOM [115]. The leaked power ultimately creates the pedestal the optical pulses and limits the achievable extinction ratio. Because an EOM is based on an MZI, the length of the interferometer arms and the ratio of couplers need to be adjusted precisely to also limit the leaked CW. In a Φ-OTDR system, the background noise created by the leaked CW power of the EOM originates from accumulated Rayleigh backscattering, which increases with the fiber length [116] and thus decreases the performance of Φ-OTDR over long distances. This background noise arises from additional phase fluctuations generated by the interference of backscattered signals originating from different locations along the fiber [117]. When using a narrow linewidth laser with a coherent length covering the entire length of the FUT, the noise generated by the pedestal power of the optical pulse cannot be reduced by averaging. Indeed, this noise arises from the interferences of light waves along the entire fiber, as opposed to thermal and shot noises which effects can be reduced by averaging [45, 117]. Therefore, it is crucial to maximize the pulse extinction ratio in order to reduce the amount of background noise present in the detected trace and thus improve the event detection capabilities of a Φ-OTDR system.

We can determine the required pulse extinction ratio for a given fiber length in a Φ-OTDR system. Starting with Eq. 2.9 and assuming that all the factors in the integrand are in phase, we obtain that the maximum backscattered field amplitude from the peak of the pulse, with $P_{\max} = |A_{\max}|^2$, can be expressed as

$$\max\left\{\left|A_{\mathrm{BS,max}}\left(t,z\right)\right|\right\} = \left|A_{\max}\right| \left| \int_{z}^{z+0.5W} \left|\alpha_s\left(\zeta\right)\right| e^{-\alpha\zeta} d\zeta \right|,$$

where $A_{\max}$ is the field amplitude of the pulse peak power. We again assume that the magnitude of the Rayleigh backscattering coefficients is constant and equals α_0, which yields

$$\max\left\{\left|A_{\mathrm{BS,max}}\left(t,z\right)\right|\right\} = \alpha_0 \left|A_{\max}\right| e^{-\alpha z} \left(\frac{1-e^{-0.5\alpha W}}{\alpha}\right). \tag{2.13}$$

Similarly, the maximum magnitude of the total electric-field amplitude corresponding to the pedestal power of the pulse, $A_{\mathrm{BS,min}}$, where $P_{\min} = |A_{\min}|^2$, is given by

$$\max\left\{\left|A_{\mathrm{BS,min}}\left(t\right)\right|\right\} = \alpha_0 \left|A_{\min}\right| \left(\frac{1-e^{-\alpha L}}{\alpha}\right), \tag{2.14}$$

where L is the length of the fiber under test, and where we assumed that the pulse covers less than the entire length of the fiber, $W \ll L$. If a perturbation occurs at the end of the fiber, it will be distinguishable from the background noise if

$$\frac{\max\left\{\left|A_{\mathrm{BS,max}}\left(t,z\right)\right|\right\}}{\max\left\{\left|A_{\mathrm{BS,min}}\left(t\right)\right|\right\}} \geq \rho$$

with $\rho > 1$. Using Eq. 2.13 and 2.14, we obtain

$$\frac{\alpha_0 \left|A_{\max}\right| e^{-\alpha L} \left(\frac{1-e^{-0.5\alpha W}}{\alpha}\right)}{\alpha_0 \left|A_{\min}\right| \left(\frac{1-e^{-\alpha L}}{\alpha}\right)} \geq \rho,$$

from which we can reorder the terms to obtain that the required extinction ratio $\varepsilon_{\mathrm{req}} = |A_{\max}|^2 / |A_{\min}|^2$, corresponding to the worst-case scenario, is expressed as [118]

$$\varepsilon_{\mathrm{req}} = \rho^2 \frac{\left(1-e^{-\alpha L}\right)^2}{e^{-2\alpha L}\left(1-e^{-0.5\alpha W}\right)^2}$$

The value of ρ is determined from the maximum allowed power fluctuation in the backscattering trace δ_{max}, which is given by

$$\begin{aligned}\delta_{max} &= \frac{P_{max}-P_{min}}{P_{max}+P_{min}} = \frac{\left(\max\left\{\left|A_{BS,max}\right|\right\}+\max\left\{\left|A_{BS,min}\right|\right\}\right)^2 - \left(\max\left\{\left|A_{BS,max}\right|\right\}-\max\left\{\left|A_{BS,min}\right|\right\}\right)^2}{\left(\max\left\{\left|A_{BS,max}\right|\right\}+\max\left\{\left|A_{BS,min}\right|\right\}\right)^2 + \left(\max\left\{\left|A_{BS,max}\right|\right\}-\max\left\{\left|A_{BS,min}\right|\right\}\right)^2} \\ &= \frac{2\rho}{1+\rho^2}.\end{aligned}$$

We thus have that ρ can be expressed as

$$\rho = \frac{1+\sqrt{1+\delta_{max}^2}}{\delta_{max}}.$$

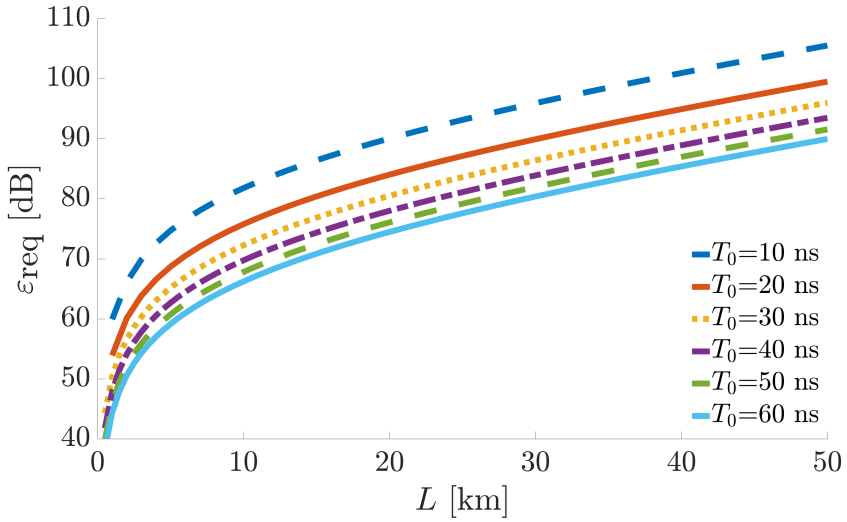

Figure 2.15: Theoretical predictions of the required pulse extinction ratio as a function of the FUT length in a Φ-OTDR system for several pulse durations when $\rho = 1$ [118].

Figure 2.15 show the minimum necessary pulse extinction ratio to allow for the detection of perturbations at the end of a fiber of length L, when assuming the limit case $\rho = 1$. As can be observed, the values of ε_{req} quickly become much higher than the extinction ratio provided by a conventional electro-optic modulator ($\sim 20\,\text{dB}$), or even a high-end modulator (40 to 50 dB). To remedy this situation, we developed a technique capable of all-optically generating high-ε pulses, which will be explained in the next chapter and demonstrated in Chap. 4. The operating principle of our technique is also utilized in the coming chapters to perform an all-optical stabilization of laser light intensity, and to perform an all-optical magnification of a fiber sensor's response to an external perturbation.

Chapter 3

Self-phase modulation of sinusoidally-modulated optical signals

The previous chapters introduced all-optical signal processing and fiber sensing, focusing on the two types of fiber sensors that will be used for vibration detection in the following chapters. In this chapter, we first introduce the Kerr effect, then derive and demonstrate the generation of optical sidebands when the Kerr effect is applied to sinusoidally-modulated optical signals (SMOS). The sidebands can be extracted using a filter to enable all-optical signal processing schemes, such as all-optical signal intensity stabilization, all-optical signal magnification and all-optical enhancement of pulses' extinction ratios. We finally analyze the power regimes of the different optical transfer functions provided by the generated sideband, which lead to the aforementioned all-optical signal processing schemes.

3.1 Kerr effect and self-phase modulation

The Kerr effect describes the dependence of a medium's refractive index on the intensity of a signal propagating through that medium. When the intensity of a light beam increases, the polarization response $\mathbf{P}(t)$ from the electric dipoles in the medium becomes a nonlinear function of the input electric field $E(t)$. In an optical fiber, the relationship between $\mathbf{P}(t)$

and $E(t)$ for a monochromatic linearly-polarized wave $E(t) = E_0 \cos(\omega t)$, with E_0 being the amplitude of the field and ω being the frequency, is given by [60]

$$\mathbf{P}(t) = \mathbf{P}_{\mathrm{L}}(t) + \mathbf{P}_{\mathrm{NL}}(t) = \epsilon_0 \left(\chi^{(1)} + \frac{3}{4}\chi^{(3)}|E_0|^2 \right) E_0 \cos(\omega t) + \frac{\epsilon_0}{4}\chi^{(3)} E_0^3 \cos(3\omega t), \tag{3.1}$$

with ϵ_0 being the permittivity of the vacuum, $\chi^{(1)}$ and $\chi^{(3)}$ respectively being the first- and third-order susceptibilities, $P_{\mathrm{L}}(t) = \epsilon_0 \chi^{(1)} E_0 \cos(\omega t)$ being the linear response of the polarization and $P_{\mathrm{NL}}(t)$ being the nonlinear response part of the polarization. The last term in Eq. 3.1 is responsible for the third-harmonic generation, while the components at frequency ω are responsible for the Kerr effect and self-phase modulation. For the purpose of this thesis, only the terms at the input frequency ω will be considered and the last term of Eq. 3.1 is ignored. The link between the signal intensity and the effective refractive index of a medium can be expressed as [8]

$$n_{\mathrm{eff}} = \sqrt{1+\chi} = \sqrt{1 + \left(\chi^{(1)} + \frac{3}{4}\chi^{(3)}|E_0|^2 \right)} \simeq n_0 + \frac{3\chi^{(3)}}{8n_0}|E_0|^2 = n_0 + n_2 I \tag{3.2}$$

where $I \propto |E_0|^2$ is the optical intensity of the electromagnetic field $E(t)$, n_0 is the linear part of the refractive index of the material, and n_2 is the material's nonlinear refractive index and is around $3 \times 10^{-20}\,\mathrm{m^2\,W^{-1}}$ in silica [8]. Due to the dependence of the refractive index on the signal intensity, when an intense optical signal propagates down an optical fiber, the phase of the signal also possesses an intensity-dependent term: $\phi = (n_0 + n_2 I)\, k_0 L$, where ϕ is the signal's phase, $k_0 = 2\pi/\lambda$ with λ is the signal wavelength, and L is the medium length. The accumulated nonlinear phase shift is expressed as $\phi_{\mathrm{NL}}(t) = n_2 k_0 L I(t)$ and varies over time if the signal's temporal profile (and thus intensity) also changes over time, as is the case for optical pulses. In this case, the time-dependent variation of the induced additional phase shift leads to the generation of new frequencies and ultimately broadens the signal's spectrum.

While conventional single-mode fibers can be utilized to generate nonlinear phase shifts, it is common to instead use optical fibers with a refractive index profile that leads to a tighter guided mode profile [60]. Indeed, the intensity of a guided signal corresponds to the power of the signal divided by the area over which the signal's modes spread, known as the effective area A_{eff}. Therefore, reducing A_{eff} increases the signal's intensity and thus increases the amount of nonlinear phase shift generated. A more commonly-used parameter to describe nonlinear media is the waveguide nonlinearity $\gamma = k_0 n_2 / A_{\text{eff}}$ [8], whose value is approximately equal to $1.3\,\text{W}^{-1}\,\text{km}^{-1}$ for a standard single mode fiber, and approximately equal to $2.3\,\text{W}^{-1}\,\text{km}^{-1}$ for a dispersion-shifted fiber (DSF) [60]. The Kerr medium used in the experiments conducted in this work is a 2-km-long DSF. The dispersion curve of such fiber is shown in Fig. 3.1, where $D = -(2\pi c/\lambda)\,\beta_2$, c is the speed of light and $\beta_2 = d^2\beta(\omega)/d\omega^2$ is the group velocity dispersion parameter and $\beta(\omega) = n(\omega)\frac{\omega}{c}$. The shift of the dispersion curve of a DSF compared to a standard single-mode fiber is obtained by reducing the core diameter or modifying the refractive index profile.

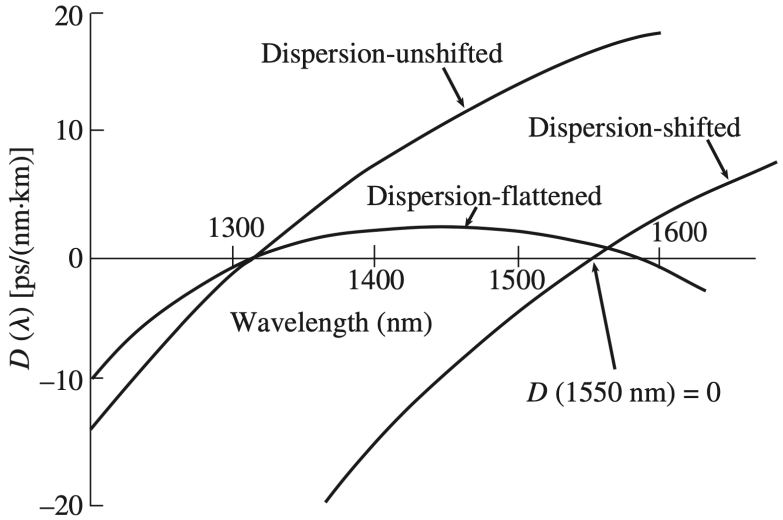

Figure 3.1: Dispersion curves for standard single-mode fiber, dispersion-shifted fiber and dispersion-flattened fiber [60], where $D = -(2\pi c/\lambda)\,\beta_2$, c is the speed of light, λ is the wavelength of operation, $\beta_2 = d^2\beta(\omega)/d\omega^2$ is the group velocity dispersion parameter, $\beta(\omega) = n(\omega)\frac{\omega}{c}$ and ω is the frequency of operation.

To determine which of the dispersion or the nonlinear effects are predominant when a pulse propagates, the length of the fiber must be compared to an equivalent dispersion length $L_{\mathrm{D}} = T_0^2/|\beta_2|$ and to an equivalent nonlinear length $L_{\mathrm{NL}} = 1/\gamma P_0$, where T_0 is the pulse width and P_0 is the peak power. Because the dispersion of a DSF is null or close to zero around the wavelength of operation (1550 nm), L_{D} is much greater than the length of the DSF utilized in our experiments, and much greater than L_{NL}. Other fiber-based medium could be used as Kerr medium in our work as long as they possess an equivalent nonlinear length much shorter than their equivalent dispersion length, and thus a high nonlinear waveguide parameter. If significant dispersion is induced while propagating through the Kerr medium, the pulse width is widened and the spatial resolution of the fiber sensor is therefore negatively affected, as explained in the previous chapter. In our case, a dispersion-shifted fiber was a suited single-mode fiber to act as a Kerr medium that was present in the laboratory at the time of the experiments. Therefore, we can neglect the dispersion occurring when a pulse propagates down our Kerr medium and describe the pulse propagation down the DSF fiber using [8]

$$\frac{\partial U}{\partial z} = -i\gamma P_0 e^{\alpha z}|U|^2 U, \tag{3.3}$$

where α is the attenuation coefficient, and U is the pulse normalized amplitude, with the pulse amplitude being expressed as $A(z,t) = \sqrt{P_0}\exp(-\alpha z/2)\,U(z,t)$. As we operate in the normal dispersion regime ($D < 0$), we can neglect the impact of four-wave mixing because the phase matching condition cannot be satisfied in this dispersion regime when SPM is induced [8]. Solving Eq. 3.3 yields [8]

$$U(L,T) = U(0,T_0)e^{i\phi_{\mathrm{NL}}(L,T)},$$

with L being the propagation distance, $T = t - z/v_g$, and $v_g = c/n_g(\omega)$ being the group velocity, with $n_g = n(\omega) + \omega\frac{\partial n}{\partial \omega}$ being the group refractive index. The induced nonlinear phase shift $\phi_{\mathrm{NL}}(L,T)$ at the end of the nonlinear medium is expressed as

$$\phi_{\mathrm{NL}}(L,T) = \left|U(0,T_0)\right|^2 \gamma P_0 L_{\mathrm{eff}}, \tag{3.4}$$

where $U(0,T_0)$ the pulse shape of width T_0 in $z=0$, and $L_{\mathrm{eff}} = \left(1-e^{-\alpha L}\right)/\alpha$ is the effective length of the nonlinear medium. The effective length L_{eff} accounts for the impact of the attenuation on the nonlinear process.

There are two main nonlinear phenomena used in all-optical signal processing that rely on the dependence of the refractive index to the light intensity expressed in Eq. 3.2. These two phenomena are self-phase modulation (SPM), which occurs when only a single signal is sent through a nonlinear medium, and cross-phase modulation (XPM) which takes place when multiple signals are sent through the nonlinear medium [8]. For the remainder of this thesis, only SPM will be considered as only a single signal source was utilized in the experiments described in the following chapters. For a pulsed light, the phase shift experienced varies across the pulse due to the inherent intensity variation in the pulse profile. The resulting frequency changes in the pulse spectrum are given as [119]

$$\delta\omega(t) = -\frac{\partial\Delta\phi}{\partial t} = -\frac{2\pi}{\lambda} n_2 L \frac{\partial I}{\partial t}. \tag{3.5}$$

Therefore, the phase shifts experienced by the leading and trailing edges of the pulse will be in opposite directions and can lead to a symmetrical broadening of the light spectrum if the pulse shape is symmetrical. The pulses utilized in our experiments are symmetrical and the sidebands produced at the output of the nonlinear medium are created symmetrically with respect to the laser frequency, as will be shown in section 3.2.

The Kerr effect was previously utilized in all-optical signal processing in telecommunications to isolate error bits [120] and to quantify the amplitude jitter of the laser source [121]. Both applications rely on a fixed SPM-based power transfer function operated in different regimes but require a stable input signal to yield reliable results. The SPM-based signal

processing schemes proposed in our work (described in the next section) also rely on different power regimes of optical transfer functions. However, our work provides more flexibility with the introduction of a sinusoidal modulation which allows for the generation of multiple transfer function at the output of the Kerr medium. The Kerr effect was also previously utilized in fiber sensing, in a configuration referred to as Kerr phase-interrogator [122]. The Kerr phase-interrogator relies on an interferometer-like polarization-based sensor placed before a nonlinear medium. Self-phase modulation is induced on continuous-wave signals exhibiting perpendicular polarization to convert the phase shift occurring between the polarization axis of the sensor into a power variation occurring at the first-order SPM-generated sideband. This Kerr-based system allowed for displacement sensing by sinusoidally modulating a laser signal and sending it into a polarization-maintaining interferometer with one arm connected to the displacement source. The reference and sensing signal were then sent to a Kerr medium and the power of the generated first-order sideband was proportional to the induced displacement [122]. A similar approach was utilized to measure chromatic dispersion of a fiber, as well as measuring temperature changes using a linearly-chirped fiber Bragg grating [123, 124].

In this work, a laser signal and/or a sensor's response is successively sinusoidally modulated and then pulse shaped before being launched into a Kerr medium. This allows for the creation of optical sidebands due to SPM. The behaviour of these SPM-generated sidebands is derived and described in the next section.

3.2 Derivation of self-phase modulation of sinusoidally modulated optical signals

To determine the amplitude of the electric field in each SPM-generated optical sideband at the output of the Kerr medium, we start by expressing the electric field amplitude of a sinusoidally-modulated optical signal

$$A = \sqrt{P_p}\cos\left(\frac{\omega_s t}{2}\right),$$

where P_p is the signal peak power, ω_s is the sinusoidal modulation frequency, and the general expression for the electric field is $E = A\exp\{i(\omega_0 t - kz)\}$, with ω_0 being the central frequency of the laser light. The signal power at the input of the Kerr medium is thus given by

$$P(t) = |A(t)|^2 = P_p\cos^2\left(\frac{\omega_s t}{2}\right) = \frac{P_p}{2}\left[1+\cos(\omega_s t)\right], \tag{3.6}$$

The field is then sent through a single-mode fiber acting as a Kerr medium with negligible attenuation. At the output of the Kerr medium, the field has experienced an additional phase shift due to self-phase modulation and the amplitude becomes

$$A = \sqrt{P_p}\cos\left(\frac{\omega_s t}{2}\right)\exp\left[j\gamma P(t)L\right], \tag{3.7}$$

with L being the length of the Kerr medium and γ being the nonlinear parameter of the waveguide. By introducing Eq. 3.6 into Eq. 3.7, we obtain

$$A = \sqrt{P_p}\cos\left(\frac{\omega_s t}{2}\right)\exp\left\{j\frac{\gamma P_p L}{2}\left[1+\cos(\omega_s t)\right]\right\},$$

and using the definition of the SPM-induced nonlinear phase shift $\phi_{\mathrm{SPM}} = \gamma P_p L$, the field amplitude can be written as

$$A = \sqrt{P_p}\cos\left(\frac{\omega_s t}{2}\right)\exp\left\{j\frac{\phi_{\mathrm{SPM}}}{2}\right\}\exp\left\{j\frac{\phi_{\mathrm{SPM}}}{2}\cos\left(\omega_s t\right)\right\}. \tag{3.8}$$

Using the Jacobi-Anger expansion [125, 126]

$$e^{(jz\cos\theta)} = \sum_{m=-\infty}^{\infty} j^m J_m\left(z\right)e^{(jm\theta)},$$

as well as the exponential expression of a cosine, we can express the amplitude of the electric field at each SPM-generated sideband, and obtain

$$A = \frac{\sqrt{P_p}}{2}\exp\left\{j\frac{\phi_{\mathrm{SPM}}}{2}\right\}\left[\sum_{m=-\infty}^{\infty} j^m J_m\left(\frac{\phi_{\mathrm{SPM}}}{2}\right)e^{j\omega_s(m+0.5)t} + \sum_{m=-\infty}^{\infty} j^m J_m\left(\frac{\phi_{\mathrm{SPM}}}{2}\right)e^{j\omega_s(m-0.5)t}\right], \tag{3.9}$$

where the $m \pm 0.5$ coefficient arises from the exponential form of the first cosine term in Eq. 3.8. After replacing m by $m+1$ in the second term of Eq. 3.9, separating the summations with respect to negative and positive integers m ,and replacing m by $-m$ in the second summation, we obtain

$$A = \frac{\sqrt{P_p}}{2}\exp\left\{j\frac{\phi_{\mathrm{SPM}}}{2}\right\}\left\{\sum_{m=0}^{\infty} j^m\left[J_m\left(\frac{\phi_{\mathrm{SPM}}}{2}\right) + jJ_{m+1}\left(\frac{\phi_{\mathrm{SPM}}}{2}\right)\right]e^{j\omega_s(m+0.5)t} + \sum_{m=1}^{\infty} j^{(-m)}\left[J_{-m}\left(\frac{\phi_{\mathrm{SPM}}}{2}\right) + jJ_{-m+1}\left(\frac{\phi_{\mathrm{SPM}}}{2}\right)\right]e^{j\omega_s(-m+0.5)t}\right\}.$$

By substituting m by $m+1$ in the second summation, using the Bessel's functions identity $J_{-v}\left(z\right) = (-1)^v J_v\left(z\right)$, as well as $(-1)^v = (j)^{2v}$ and reorganizing, we obtain the final expression of the field amplitude at the output of the Kerr medium

$$A = \sum_{m=0}^{\infty} j^m\frac{\sqrt{P_p}}{2}\exp\left\{j\frac{\phi_{\mathrm{SPM}}}{2}\right\}\left[J_m\left(\frac{\phi_{\mathrm{SPM}}}{2}\right) + jJ_{m+1}\left(\frac{\phi_{\mathrm{SPM}}}{2}\right)\right]e^{j\omega_s(m+0.5)t} + \sum_{m=0}^{\infty} j^m\frac{\sqrt{P_p}}{2}\exp\left\{j\frac{\phi_{\mathrm{SPM}}}{2}\right\}\left[J_m\left(\frac{\phi_{\mathrm{SPM}}}{2}\right) + jJ_{(m+1)}\left(\frac{\phi_{\mathrm{SPM}}}{2}\right)\right]e^{-j\omega_s(m+0.5)t}.$$

The power of the field at each generated sideband of frequency $\omega_0 \pm (m + 0.5)\,\omega_s$ is expressed as:

$$|A|^2_{w_0 \pm (m+0.5)\omega_s} = \left| j^m \frac{\sqrt{P_p}}{2} \exp\left\{ j\frac{\phi_{\text{SPM}}}{2} \right\} \left[J_m\left(\frac{\phi_{\text{SPM}}}{2}\right) + jJ_{m+1}\left(\frac{\phi_{\text{SPM}}}{2}\right) \right] \right|^2$$
$$= \frac{P_p}{4} \left[J_n^2\left(\frac{\phi_{\text{SPM}}}{2}\right) + J_{n+1}^2\left(\frac{\phi_{\text{SPM}}}{2}\right) \right]. \tag{3.10}$$

Figure 3.2 shows the calculated values of the relative sideband powers as a function of the nonlinear phase shift, corresponding to Eq. 3.10. The measurements shown in Fig. 3.2 were performed using an optical spectrum analyzer to monitor the power at each sideband for a given input peak power and are in good agreement with the theoretical predictions.

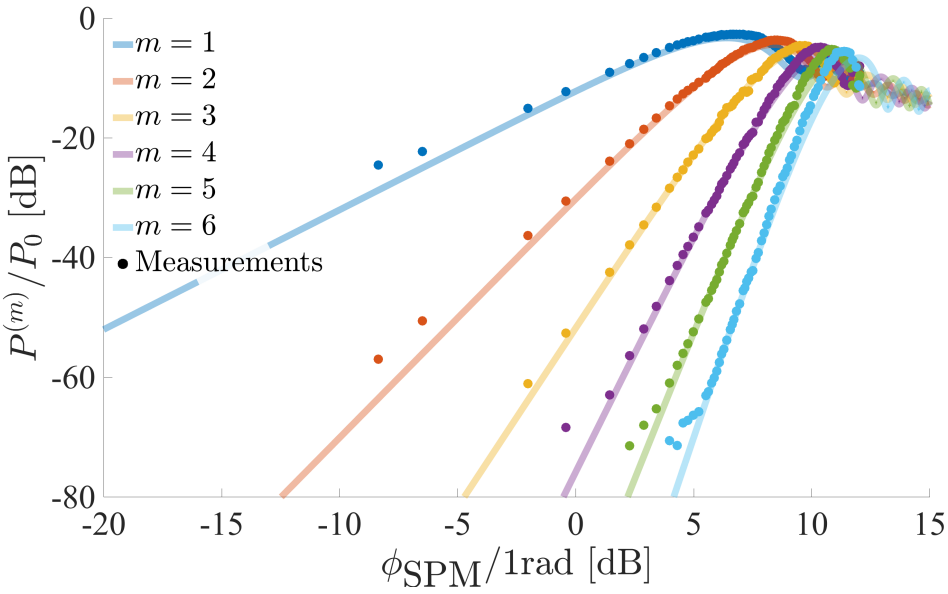

Figure 3.2: Theoretical and measured values of the SPM-generated sideband power as a function of the nonlinear phase shift. The theoretical predictions arise from Eq. 3.10 and are in good agreement with the measurements. The latter are obtained by measuring each sideband peak power as the input pulse peak power is modified.

A conceptual experimental setup to generate sidebands at the output of a Kerr medium is presented in Fig. 3.3(a). A continuous-wave (CW) laser signal, whose frequency spectrum and temporal power profile are shown in Fig. 3.3(b), is first sinusoidally modulated with a

frequency f_m by an electro-optic modulator, as illustrated in Fig. 3.3(c). A pulse is then impressed onto the sinusoidally modulated optical signal using a second EOM, as illustrated in Fig. 3.3(c). After the two cascaded EOMs, the optical pulse experiences SPM in a nonlinear Kerr medium, leading to a broadening of the spectrum as predicted by Eq. 3.5. The broadened frequency spectrum features the optical sidebands described in Eq. 3.10, and is illustrated in Fig. 3.3(e). Finally, an SPM-generated sideband is extracted using a band-pass filter (BPF), as shown in Fig. 3.3(f).

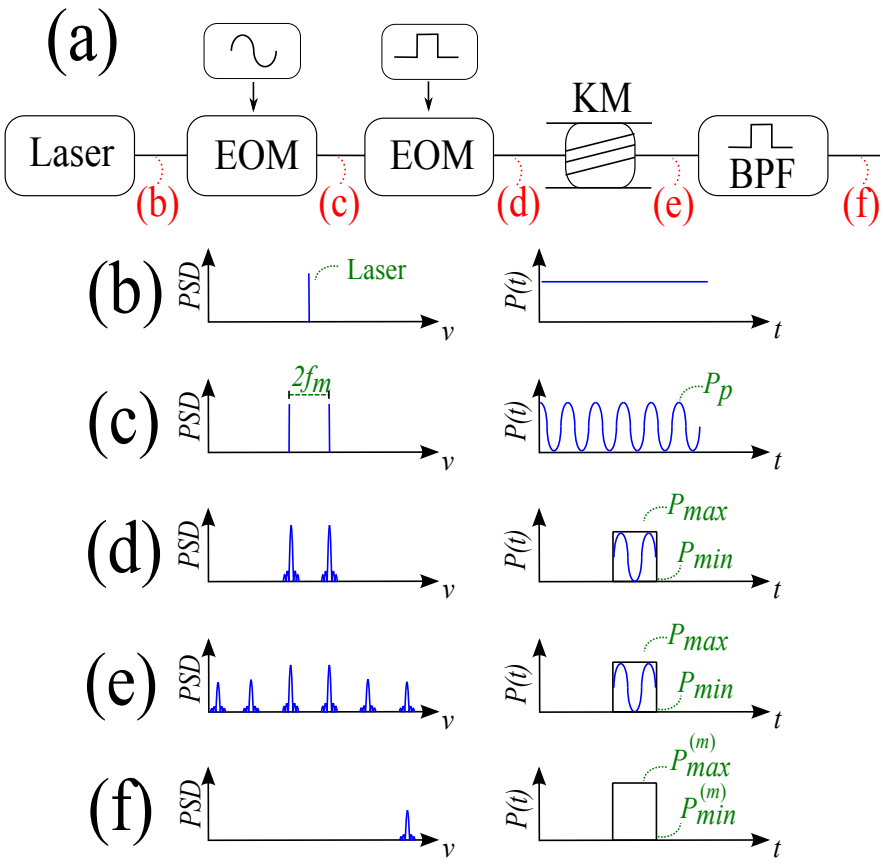

Figure 3.3: a) Schematic of a conceptual setup to allow for sideband generation at the output of a Kerr medium, b) the CW laser signal, c) the SMOS, d) the square-pulse impressed SMOS, e) the square-pulse impressed SMOS after experiencing SPM in the Kerr medium, f) the square pulse obtained after extracting the m^{th}-order sideband. The plots on the left part of b) to f) represent the power spectral density (PSD), with ν being the frequency and f_m being the EOM modulation frequency; and the plots on the right represent the power temporal profile, with P_p being the peak power and m being the order of the extracted sideband. BPF: Band-pass filter, EOM: Electro-optic modulator, KM: Kerr medium [118]

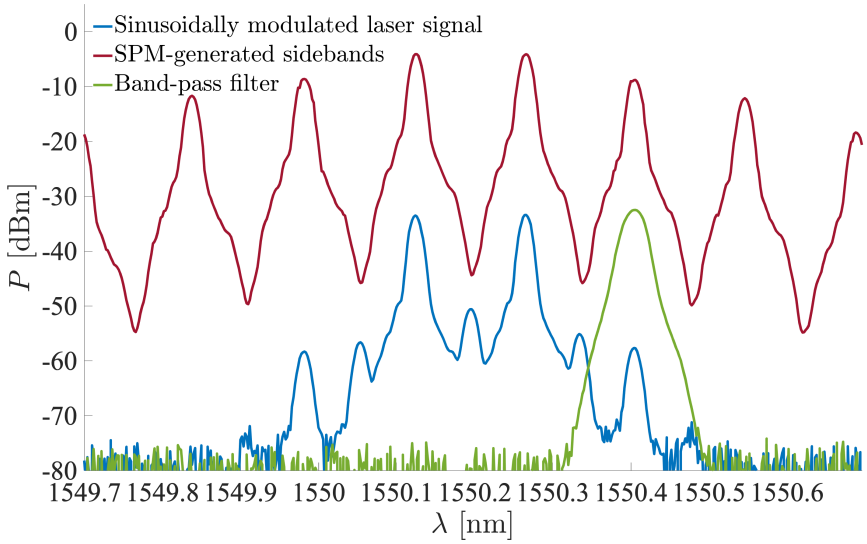

Figure 3.4: Measured spectra of the sinusoidally modulated laser signal in blue, SPM-generated sidebands in red, and band-pass filter in green, corresponding to Fig. 3.3. The sinusoidal modulation frequency is $f_m = 8.9\,\text{GHz}$, the input peak power is on the order of 16 dBm, and the BPF's bandwidths is 3 GHz.

Figure 3.4 shows the measured spectra corresponding to Fig 3.3(d) and (e), as well as the BPF spectrum aligned, in this particular case, with the first-order sideband. The setup presented in Fig. 3.3 uses optical pulses to generate sidebands at the output of the Kerr medium. This pulse-based approach will be used in the next sections to demonstrate the regimes of operation arising from the SPM-generated sidebands. However, the generation of sidebands through SMOS experiencing SPM is not limited to pulsed light and is valid for CW laser signals. In our case, a sinusoidally-modulated CW light could not directly be sent through the Kerr medium without first being pulse-modulated as a high-power CW signal propagating in a conventional single-mode optical fiber leads to the generation of Brillouin scattering. The presence of Brillouin scattering would induce a backward propagating signal, which could be blocked by introducing an isolator in principle, but it would also further decrease the light's peak power as it propagates down the Kerr medium. This reduction of power would reduce the amount of achievable nonlinear phase shift and therefore hinder sideband generation.

3.3 Regimes of operation

Multiple sidebands can be generated at the output of the Kerr medium for a given initial signal peak power, as depicted in Fig. 3.3(e) and shown in Fig. 3.4. Therefore, by adjusting the input peak power and extracting a specific sideband using the band-pass filter, several regimes of operation can be achieved. Each regime of operation will be discussed in the following subsections and demonstrated in the following chapters.

3.3.1 Generation of high extinction ratio optical pulses

The first regime obtainable when an SMOS undergoes SPM is the generation of high extinction ratio optical pulses. As mentioned in the previous chapter, the pedestal power of the pulse launched into the fiber under test in a Φ-OTDR contributes to the background noise measured at the detector. The extinction ratio of a conventional EOM ranges between 20 and 40 dB, limiting the maximum distance at which a perturbation is guaranteed to be detected in a Φ-OTDR system, as was shown in Fig. 2.15. A conceptual overview of this regime of operation is shown in Fig. 3.5.

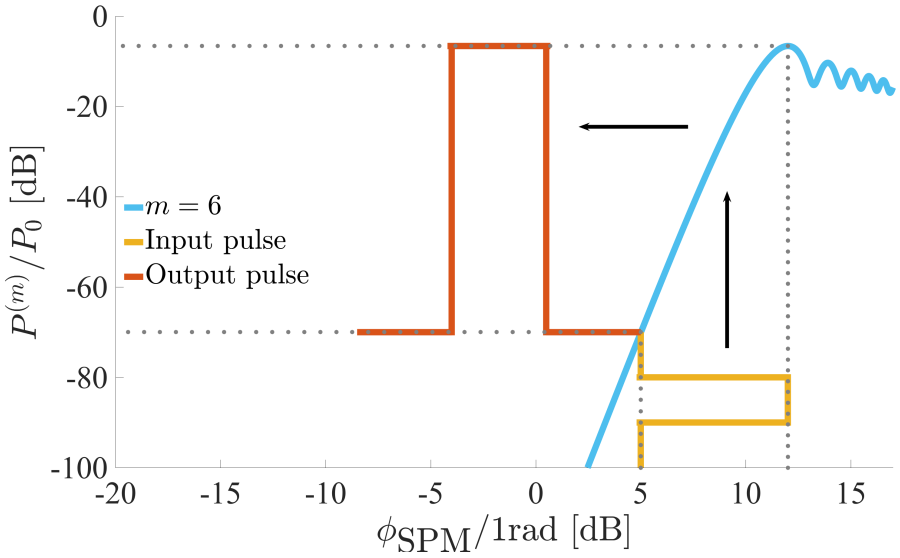

Figure 3.5: Generation of high-ε pulses (in red) by adjusting the the peak power of the input pulse (in yellow) to match the maximum point of the transfer function (in blue).

As illustrated in Fig. 3.5, the pulse peak power must be located at the maximum point of the transfer function obtained using Eq. 3.10. However, each sideband order possesses its own maximum transfer function point, corresponding to a specific induced ϕ_{SPM}, as observed in Fig. 3.2. Thus, by locating the peak of each transfer function and fitting a dual exponential function linking the sideband order m (for $m = 1$ to $m = 20$) and the required ϕ_{SPM} to maximize the relative output power, we obtain that to generate high-ε pulses, the input pulse peak power must be adjusted to generate a nonlinear phase shift satisfying the following condition:

$$\phi_{\mathrm{SPM}}/1\,\mathrm{rad}\ [\mathrm{dB}] = 12.34 \times \exp\left(\frac{3m}{200}\right) - 7.96 \times \exp\left(-\frac{29m}{100}\right). \tag{3.11}$$

This condition ensures the alignment of the peak power of the pulse entering the Kerr medium with the maximum point of the transfer function, as shown in Fig. 3.5. In the case of the 6^{th}-order sideband shown in Fig. 3.5, the condition becomes $\phi_{\mathrm{SPM}}/1\,\mathrm{rad} = 12\,\mathrm{dB}$. When the condition in Eq. 3.11 is met, the extinction ratio of the pulse at the output of the Kerr medium $\varepsilon_{\mathrm{out}}$ can be expressed as

$$\varepsilon_{\mathrm{out}}^{(m)}\ [\mathrm{dB}] = (2m+1)\varepsilon_{\mathrm{in}}\ [\mathrm{dB}] - 3.2m - 2.7, \tag{3.12}$$

for $5\,\mathrm{dB} < \varepsilon_{\mathrm{in}} < 40\,\mathrm{dB}$, where $\varepsilon_{\mathrm{in}}$ is the extinction ratio of the pulse entering the Kerr medium. If we use $\varepsilon_{\mathrm{in}} = 20\,\mathrm{dB}$ and extract the 6^{th}-order, the output extinction ratio is theoretically higher than 200 dB, as shown in Fig. 3.6. In the next chapter, we will propose a method to quantify the extinction ratio obtained at the 6^{th}-order sideband, because conventional photodetectors would not allow for the measurement of the power at the pulse's pedestal. Indeed, the minimum detectable power of photodetectors is on the order of $-40\,\mathrm{dBm}$, while the peak power of a pulse at the output of the Kerr medium is on the order of 10 dBm in our experiments (a typical value for fiber sensing applications). Therefore, the true extinction ratio of the high-ε pulses generated by our SMOS-based approach cannot be characterized

using conventional photodetectors as a proper measurement of the pedestal power is not possible.

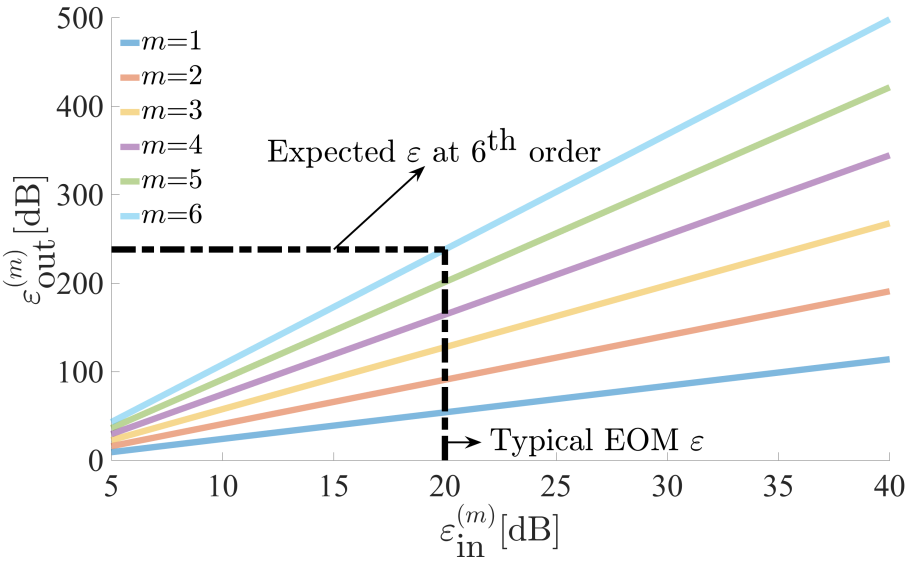

Figure 3.6: Plot of Eq. 3.12, and visual demonstration of the expected extinction ratio at the 6^{th}-order sideband when a conventional EOM is utilized to generated the input pulse.

The benefit of utilizing high-ε pulses is demonstrated using a Φ-OTDR system and allows to achieve a range of measurement more than four times larger when using high-ε pulses, compared to conventional EOM-generated pulses [118]. Figure 3.7 shows a comparison between the Φ-OTDR traces obtained with high-ε pulses and regular-ε pulses when using a direct-detection scheme. Each subfigure in Fig. 3.7 represents consecutive backscattering traces, equivalent to the one presented in Fig. 2.12. When comparing Fig. 3.7(a) and (b), which correspond to the Φ-OTDR traces of a 1.5-km fiber under test when using a high-ε and a regular-ε ($\sim 20\,\text{dB}$) pulse respectively, it is evident that the contribution of the pedestal power to the background noise of the trace cannot be neglected. Indeed, the backscattered signal arising from the pulse pedestal power interferes with the backscattered signal of the pulse peak power all along the fiber and acts as a background noise added on top of the trace. When the length of the FUT is increased, such as in Fig. 3.7(c) and (d), it becomes even clearer that a low-ε pulse does not allow for performing any sort of long distance Φ-OTDR measurements when using a direct detection scheme.

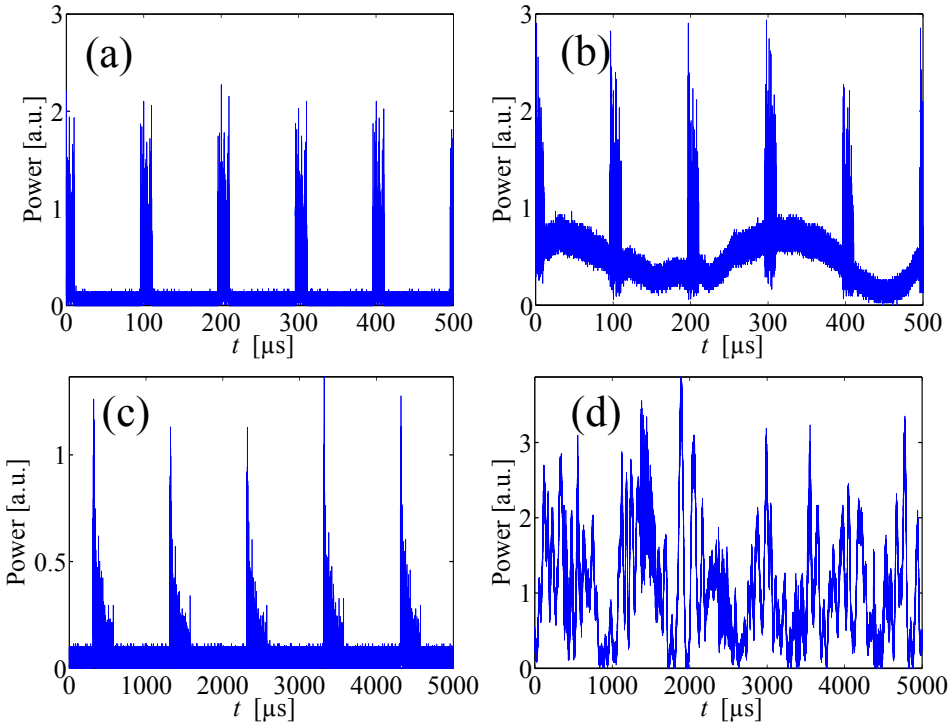

Figure 3.7: Measured backscattering traces of a) high-ε pulses for a 1.5 km fiber under test (FUT), b) direct-modulation pulses with a 20 dB ε generated using a conventional electro-optic modulator for a 1.5 km FUT, c) high-ε pulses for a 26.5 km FUT, and d) direct-modulation pulses for a 26.5 km FUT [118].

The backscattered light arising from the pulse pedestal (also referred to as CW) is coherently added all along the fiber length when the coherence length of the laser is higher than the length of the FUT, which is the case in Fig. 3.7 where the laser linewidth equals 3 kHz. To reduce the CW-induced backscattered power and allow to detect the trace of a longer FUT with a low-ε pulse, one can use a laser with a larger linewidth and thus a lower coherent length. However, when the laser linewidth is increased, the phase noise of the laser is also increased [127, 128] which decreases Φ-OTDR performances [129, 130]. Thus, when using a Φ-OTDR system, there is a tradeoff between the laser linewidth, the pulse's extinction ratio and the maximum detectable FUT length. Because the pulse extinction ratio requirement is tightly linked to the length of the fiber under test in a Φ-OTDR system, as shown in Fig. 2.15, research groups have started to use higher quality EOMs or cascade multiple regular EOMs to increase the pulses ε[113, 131–133]. However, this led to claims of ε beyond 70 dB [52] without actual measurements, since conventional detectors do not have the capability of

measuring the pedestal power of such high-ε pulses. Therefore, and to verify our claim of high-ε provided by SMOS undergoing SPM, we utilize a single-photon counter to allow for the measurement of the pulse pedestal power, and the results are presented in Chap. 4.

The general condition expressed in Eq. 3.11 not only allows the generation of high-ε pulses when a higher-order sideband is extracted, but also allows stabilization of the peak power of an input signal when the first sideband is extracted. This will be discussed in the next section and demonstrates the versatility of all-optical signal processing provided by SMOS experiencing the nonlinear Kerr effect.

3.3.2 Stabilization of input signal power fluctuations

When the first-order sideband is extracted at the output of the Kerr medium using a bandpass filter, the power fluctuations present at the peak power of the pulse can be reduced. To achieve this, the nonlinear phase shift induced by the average peak power of the pulse must be equal to 6.4 dB/1rad, as given by Eq. 3.11 when $m = 1$. This condition enables the placement of the input peak power around the flatter part of first-order sideband power profile, which reduces the power fluctuations at the output of the bandpass filter, as conceptually demonstrated in Fig. 3.8. Figure 3.9 shows that extracting the first-order sideband allows the stabilization of the largest range of input peak power fluctuations.

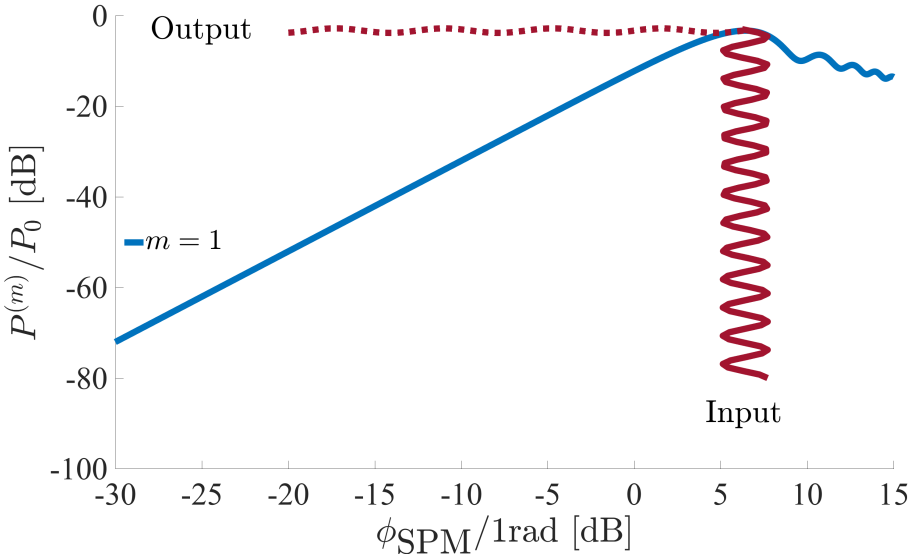

Figure 3.8: Visualization of signal stabilization when the first-order SPM-generated sideband is extracted at the output of the Kerr medium. The average induced nonlinear phase shift must be equal to 6.4 dB/1rad to place the input signal at the maximum point of the sideband's transfer function.

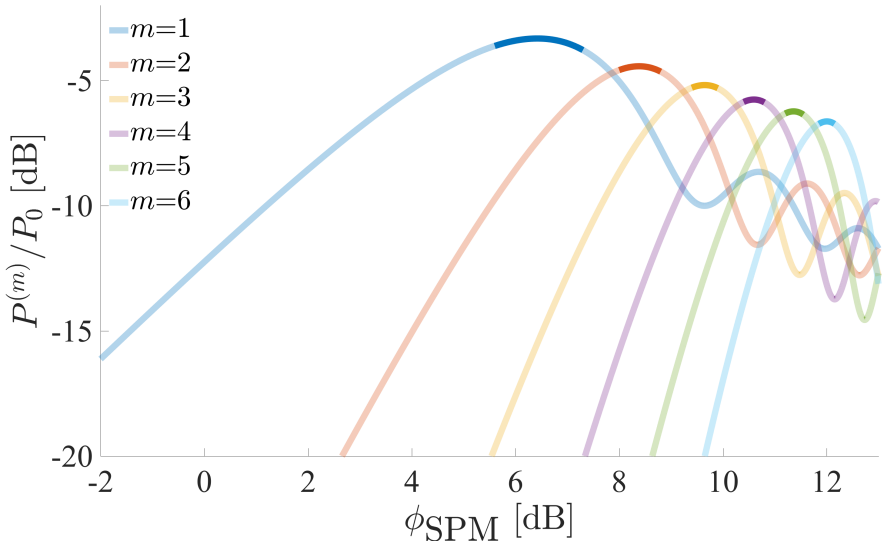

Figure 3.9: Visualization of stabilization power regime for different sideband orders. The first-order sideband allows for the largest input power fluctuations when imposing a given tolerance on the output power fluctuations.

A conceptual fiber sensing setup using all-optical signal stabilization is presented in Fig. 3.10. The laser output power can be expressed as $P_{\mathrm{L}} = P + \delta P$, with $\delta P \ll P$ and where P is the initial average output power ,and δP is the power variation around the average power.

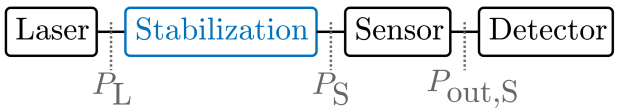

Figure 3.10: Schematic of a fiber sensing setup including a power stabilization stage. P_{L} is the laser power, P_{S} is the stabilized laser power and $P_{\mathrm{out,S}}$ is the output power of the sensor with stabilized input power.

Defining the relative power fluctuation as:

$$F \simeq \frac{\delta P}{P},$$

we can express the laser output power as $P_{\mathrm{L}} = P(1+F)$. Without accounting for the losses occurring during the light propagation through the setup, the stabilized laser power can be expressed as

$$P_{\mathrm{S}} = P(1+\eta F),$$

where η is the fluctuation reduction factor provided by our stabilization technique. This factor can be determined using a polynomial fit of the first-order sideband peak region and is expressed as

$$\eta = 10^{-2}\left(22F + 0.17 + \frac{0.003}{F}\right).$$

The stabilized signal then passes through a fiber-based sensor. For this demonstration, as well as for the following magnification regime, only an interferometric intensity-based sensor is considered because this type of sensor will be utilized to demonstrate the combined interest of stabilization and magnification in fiber point sensing in Chap. 7. Such a sensor converts the relative phase difference between its two arms into power following a cosine square law, as shown in Fig. 2.4 and demonstrated in the previous chapter. The output power of the sensor with a stabilized input power can be re-written as

$$P_{\mathrm{out,S}} = \alpha_s P_{\mathrm{in}} \cos^2\left(\frac{\phi_d}{2}\right) \simeq \Omega(1+\eta F)(1+\Delta\phi_d), \tag{3.13}$$

where $\Omega = 0.5\alpha_s P$, and when the sensor is operated at the quadrature point. Equation 3.13

refers to the steady state output of the sensor, however the advantage of a stabilized input power becomes apparent when an external perturbation is applied on the sensor, such as strain for instance. The output power of the sensor under strain with stabilized input light $P_{\text{out,S}}\big|_{\Delta\epsilon}$ can be expressed by introducing Eq. 2.5 into Eq. 3.13 and is given by

$$P_{\text{out,S}}\big|_{\Delta\epsilon} = \Omega(1+\eta F)(1+\phi_{d,0}+\phi_{d,0}\theta_\epsilon\Delta\epsilon), \tag{3.14}$$

while the generated output power difference generated by strain $\Delta\epsilon$ is expressed as

$$\Delta P_{\text{out,S}}\big|_{\Delta\epsilon} = P_{\text{out,S}}\big|_{\Delta\epsilon} - P_{\text{out,S}} = \Omega(1+\eta F)\phi_{d,0}\theta_\epsilon\Delta\epsilon.$$

We can thus observe that the amount of noise in the measured power difference, which is given by $\Omega\eta F\phi_{d,0}\theta_\epsilon\Delta\epsilon$, is reduced by a factor η compared to the same setup using non-stabilized laser light. Assuming that the main source of background noise at the detection system arises from the intensity noise of the laser source, this stabilization technique allows for enhancing sensing performances as the minimum detectable environmental perturbation is reduced. However, if the detection system noise, which arises from the photodetector and the oscilloscope, dominates the other noises contributions, a magnification of the signal is required to allow for the detection of an external perturbation applied to the sensor.

3.3.3 Magnification of input signal fluctuations

The stabilization regime requires a specific sideband to be extracted and specific amount of induced nonlinear phase shift. However, a magnification regime can also be obtained from SMOS undergoing SPM in a nonlinear Kerr medium over a wider range of induced phase shift and without sideband order restrictions, as shown in Fig. 3.11.

The obtained all-optical magnification allows for the detection of external perturbations that would otherwise be too small to be detected. Because the magnification takes place

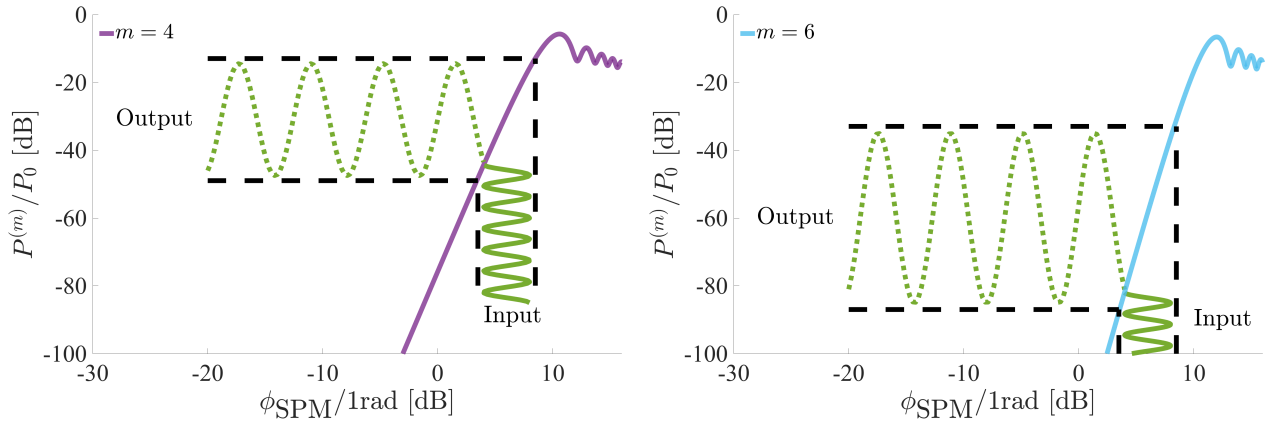

(a) 4^{th}-order sideband (b) 6^{th}-order sideband

Figure 3.11: Visualization of all-optical signal magnification using the same input power fluctuation when extracting the 4^{th}- and 6^{th}-order sidebands at the output of the Kerr medium, respectively in (a) and (b).

in the so-called linear regime of the SMOS undergoing SPM, we can utilize the asymptotic regime of the Bessel functions which is expressed as

$$J_m\left(\frac{\phi_{\text{SPM}}}{2}\right) \sim \frac{1}{m!}\left(\frac{\phi_{\text{SPM}}}{4}\right)^m \quad \text{for} \quad 0 < \left(\frac{\phi_{\text{SPM}}}{2}\right) \ll \sqrt{m+1}. \tag{3.15}$$

Thus, Eq. 3.10 becomes

$$\begin{aligned} P^{(m)}\left(\phi_{\text{SPM}}\right) &= \frac{1}{4}P_p\left[\left(\frac{1}{m!}\right)^2\left(\frac{\phi_{\text{SPM}}}{4}\right)^{2m} + \left(\frac{1}{m+1!}\right)^2\left(\frac{\phi_{\text{SPM}}}{4}\right)^{2m+2}\right] \\ &= \left(\frac{P_p}{4}\right)^{(2m+1)}\left(\frac{1}{m!}\right)^2(\gamma L)^{2m}\left[1+\left(\frac{1}{m+1}\right)^2\left(\frac{\phi_{\text{SPM}}}{4}\right)^2\right] \end{aligned} \tag{3.16}$$

Based on the domain of validity of Eq. 3.15, we can write:

$$1+\left(\frac{1}{m+1}\right)^2\left(\frac{\phi_{\text{SPM}}}{4}\right)^2 \simeq 1$$

The validity of this asymptotical approximation is visually demonstrated in Fig. 3.12.

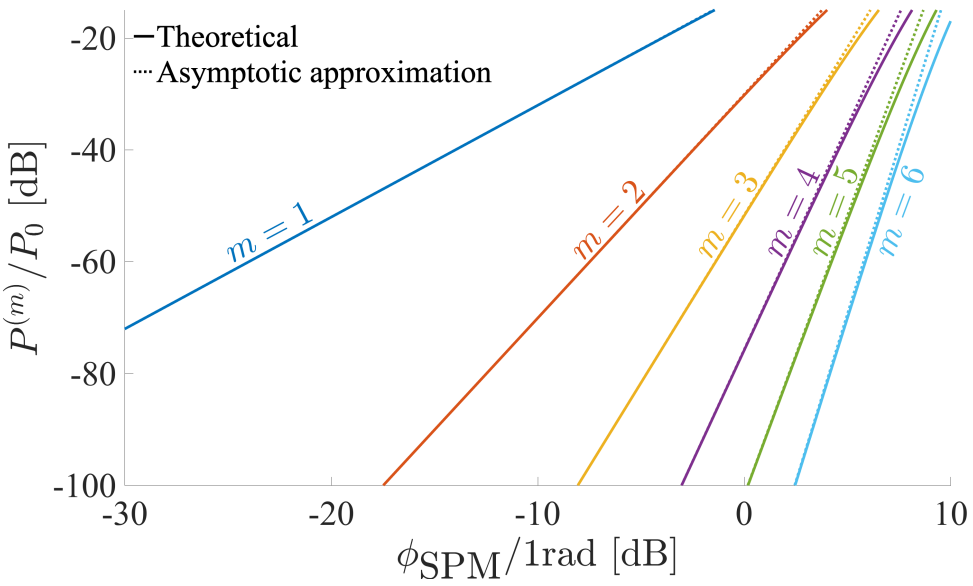

Figure 3.12: Theoretical and asymptotical approximations of the power behaviour of SMOS experiencing the nonlinear Kerr effect, respectively expressed in Eq. 3.10 and Eq. 3.16.

Using this simplification, the power output of the m^{th}-order sideband in the magnification regime can be approximated by

$$P^{(m)}\left(\phi_{\mathrm{SPM}}\right) = \left(\frac{P_p}{4}\right)^{(2m+1)} \left(\frac{1}{m!}\right)^2 (\gamma L)^{2m}\,. \tag{3.17}$$

A conceptual setup using all-optical magnification is presented in Fig. 3.13, where an interferometric intensity-sensor is operated at the quadrature point, as shown in Fig. 2.4.

Figure 3.13: Conceptual setup for all-optical signal magnification. P_{L} is the laser power, P_{out} is the power at the output of the sensor, and $P_{\mathrm{out,M}}$ is the magnified sensors' output power.

Similarly to Eq. 3.13, the output power of the intensity-based sensor operated at the quadrature point can be written as

$$P_{\mathrm{out}} = \Omega(1+F)(1+\Delta\phi_d). \tag{3.18}$$

The sensor's output power is then magnified and the resulting signal power can be determined by introducing Eq. 3.18 into Eq. 3.17, with $P_{\text{out}} = P_p$. We thus have that the magnified sensor response when extracting the m^{th}-order sideband is expressed as

$$P_{\text{out,M}}^{(m)} = \xi_m \Omega^{2m+1} (1+F)^{2m+1} (1+\Delta\phi_d)^{2m+1}, \tag{3.19}$$

with $\xi_m = (0.25)^{2m+1} (1/m!)^2 (\gamma L)^{2m}$. When strain is applied to the sensor, the magnified output power is found by introducing Eq. 2.5 into Eq. 3.19 and is expressed as

$$\begin{aligned} P_{\text{out,M}}^{(m)}\big|_{\Delta\epsilon} &= \xi_m \Omega^{2m+1} (1+F)^{2m+1} \left(1+\phi_{d,0}+\phi_{d,0}\theta_\epsilon \Delta\epsilon\right)^{2m+1} \\ &= \xi_m \Omega^{2m+1} (1+F)^{2m+1} (1+\phi_{d,0})^{2m} \Big(1+\phi_{d,0}+(2m+1)\phi_{d,0}\theta_\epsilon \Delta\epsilon\Big), \end{aligned} \tag{3.20}$$

and the generated output power difference induced by $\Delta\epsilon$ is given by

$$\Delta P_{\text{out,M}}^{(m)}\big|_{\Delta\epsilon} = P_{\text{out,M}}^{(m)}\big|_{\Delta\epsilon} - P_{\text{out,M}}^{(m)} = \xi_m \Omega^{2m+1} (1+F)^{2m+1} (1+\phi_{d,0})^{2m} (2m+1)\phi_{d,0}\theta_\epsilon \Delta\epsilon. \tag{3.21}$$

If we normalize Eq. 3.21 using Eq. 3.19, we obtain that our all-optical magnification scheme allows magnification of the induced amplitude change on the light by a factor of $2m+1$ when extracting the m^{th}-order sideband. Therefore, because this magnification scheme is all-optical, one could imagine cascading multiple magnification steps to significantly enhance the detection capabilities of existing intensity-based fiber sensors. The proposed magnification scheme will be experimentally demonstrated in Chap. 6 and combined with our all-optical stabilization scheme in Chap. 7.

In summary, inducing self-phase modulation on sinusoidally-modulated optical signals allows for various all-optical signal processing schemes that can benefit fiber distributed and point sensing. However, each scheme comes with its own caveats. First, the generation of high-ε pulses requires the peak power of the input pulse to be stable. Any peak power fluctuation will be magnified given how sharp the transfer function is around the maximum

transmission point, as shown in Fig. 3.9. This magnification will induce a signal pulse shape modification and the conventional analysis and expectations of an OTDR-based systems will not be valid because their working principle assumes square pulses, as was shown in the previous chapter. The temporal profile of a vibration applied in a Φ-OTDR may therefore not be recovered if the pulse shape is too distorted, even though the optical pulse possesses a high extinction ratio. Second, and as will be shown in Chap. 5, the stabilization regime offers a nonlinear amount of stabilization depending on the input power fluctuation which could be detrimental if the output power fluctuations need to be maintained below a given specification. Moreover, the average peak power of the input signal must remain constant to ensure that the stabilization schemes is operating at the maximum transmission point and provides the maximum amount of stabilization. For highly-perturbed input power, this stabilization scheme may not be suited as strong power deviation would place the signal into the magnification regime, thus defeating the purpose of the scheme. Finally, in the magnification regime, while a sensor's response can be magnified, any other perturbation occurring on the interrogation system will also be magnified and added onto the sensor's response. These perturbations can arise from external environmental perturbation or from optical noises, for example the ASE noise from the amplifiers. Moreover, the initial laser power fluctuation will be magnified and compounded to the external perturbation, further increasing the noise in the detected signal and hindering the initial objective of all-optical signal magnification. Therefore, for this technique to be utilized in a practical scenario, it is crucial to stabilize the laser power before the light reaches the sensor, and to shorten the distance between the sensor and the magnification stage to avoid additional undesired external perturbation.

Chapter 4

Measurement of high extinction ratio pulses by single-photon counting

We have seen in the previous chapter that high extinction ratio optical pulses can be generated by taking advantage of a pulse-shaped sinusoidally-modulated optical signals undergoing self-phase modulation. As was graphically represented in Fig. 3.5, the input peak power must be adjusted to satisfy Eq. 3.11, which ensures that we operate around the maximum point of the m^{th}-order sideband's transfer function. To achieve the generation of high-ε pulses, additional filtration steps are required before the signal enters the Kerr medium to prevent the initial laser signal from reaching the nonlinear medium. Thus, dual-gratings filters are added to the experimental setup when compared to the conceptual setup presented in Fig. 3.3(a). These gratings possess an individual bandwidth of 2.5 GHz, and their central wavelengths are separated by 17.8 GHz. They also possess a 75 % reflectivity and a 30 dB central frequency rejection. When a conventional electro-optic modulator is utilized to create a pulse, a pulse exhibiting an ε between 20 and 40 dB can be obtained. If a pulse with such an ε enters the Kerr medium after being sinusoidally modulated and Eq. 3.11 is satisfied, one can generate optical pulses with an ε theoretically higher than 200 dB by extracting a high-order sideband at the output of the Kerr medium, as expressed in Eq. 3.12. However, because the peak power at the output of the Kerr medium is on the order of 15 dBm using

our 2-km DSF (with an input peak power of 18.5 dBm), this means that the pulse pedestal power is approximately equal to −190 dBm, or 10^{-10} pW. It becomes quickly apparent that a conventional photodetector, whose minimum detectable power is in the tens to hundreds of nanowatts, will not be sufficient to measure the pedestal power of the high-ε pulse and to characterize the extinction ratio of the optical pulses generated using our technique. We therefore decided to employ a single-photon counter [134] to characterize both the peak power and the pedestal power of the pulse. Given the disparity between the peak and pedestal power levels, the peak power was subjected to high attenuation in order to avoid the saturation of the photon counter. The photon counter used in the following manuscript is based on avalanche photodiodes [135, 136], as opposed to the conventional photomultiplier tube [137], and was loaned to our research group by the company ID Quantique. Photon counting was previously used in fiber sensing, in OTDR [138–140] and when using fiber Bragg gratings [141]. However, a photon counter was never utilized for pulse ε characterization since an approach to generate high ER pulses has only been recently demonstrated [118]. In this work, we present the use of a single-photon counter for measuring the extinction ratio of high-ε pulses and report the measurement of an optical pulse exhibiting an ε of 120 dB.

4.1 Characterization of high extinction ratio optical pulses

applied optics

High extinction ratio optical pulse characterization method via single-photon counting

Benoit Vanus,* Chams Baker, Liang Chen, and Xiaoyi Bao

University of Ottawa, Department of Physics, Ottawa (ON), K1N 6N5, Canada
**Corresponding author:* [redacted]

Received 9 September 2020; revised 23 November 2020; accepted 25 November 2020; posted 1 December 2020 (Doc. ID 409800); published 21 December 2020

We present the characterization of high extinction ratio (ε) square optical pulses using a photon counting technique, as other techniques only offer a limited range of measurement up to 60 dB. High-ε pulses are generated by applying a square pulse modulation on sinusoidally modulated optical signals, then inducing self-phase modulation (SPM) using the nonlinear Kerr effect and extracting an SPM-generated sideband. We measured a 10 ns Kerr-generated optical pulse exhibiting a 120.1 dB extinction ratio, originating from a conventional electro-optic modulator delivering a pulse with a 20-dB extinction ratio, by counting the number of photons at the peak and the pedestal of the generated pulse. These proven high-ε pulses allow for long-range distributed vibration sensing in optical time-domain reflectometry systems and open new horizons in high-Q microring sensors.

https://doi.org/10.1364/AO.409800

1. INTRODUCTION

In most optical time-domain reflectometry systems (OTDRs), pulses with a duration on the order of 10 ns are launched into a fiber under test (FUT), and a fraction of the pulse energy is scattered all along the FUT due to Rayleigh scattering. The location of events occurring along the FUT is performed by monitoring the intensity variations of the backpropagating scattering signal [1], whose intensity is 40 to 60 dB lower than the pulse power [2]. The minimization of the noise contributions to the backscattered signal requires the maximization of the pulse extinction ratio [3–6], defined as $\varepsilon = P_p/P_\Delta$, where P_p and P_Δ are, respectively, the peak and pedestal power levels of a square pulse, as illustrated in Fig. 1. Commercially available high-ε electro-optic modulators can provide an extinction ratio up to 40 dB. When cascaded, an extinction ratio of 60 dB can be generated [7], which allows the propagation of 10 ns pulses over an 8.4 km sensing range, providing a 1 m spatial resolution, and has been utilized for the detection of a 20 kHz acoustic signal. Extinction ratios higher than 110 dB were reported by cascading two acousto-optic modulators (AOMs) of, respectively, 50 and 65 dB, which allows for a vibration detection at 102.7 km with a 7.3 dB signal-to-noise ratio [8]. However, the actual value of ε was deduced from the addition of the AOMs' individual extinction ratios, which is not a reliable approach to measuring high extinction ratios, as discussed by Ren *et al.* [7].

The conventional method to measure an optical pulse extinction ratio uses photodiodes to measure the power at the pulse pedestal, represented by P_Δ in Fig. 1. This method is valid only if the pedestal lies above the detector noise floor, represented by the dashed red line in Fig. 1. However, the minimum detectable power of a conventional photodiode is on the order of nanowatts, preventing an accurate measurement of the P_Δ from a high-ε pulse, as shown in Fig. 1. Another technique to measure ultrashort pulses ε takes advantage of a second-harmonic generation process but is limited at 50 dB [9]. Various extinction ratio enhancement techniques have been reported reaching up to 15 dB enhancement [10,11] in which the optical pulse pedestal power still remains above the photodetector noise floor. We have recently reported a technique capable of enhancing the extinction ratio of an optical pulse, and theoretically achieve ε beyond 200 dB through self-phase modulation (SPM) induced by the nonlinear Kerr effect [12]. As we also used photodetectors, we were limited to the measurement of an ε enhancement of 60 dB. To measure high pulse extinction ratios, an infrared single-photon counter (SPC) is required because its noise floor falls in the range of tens to hundreds of photons per second and allows for the measurement of P_Δ, as depicted by the solid green line in Fig. 1. The power collected over 1 s is therefore on the order of $P = [N \times h \times c/\lambda]/1\,\mathrm{s} = N \times 1.28^{-19}$ W, assuming an optical wavelength $\lambda = 1550$ nm, with c the speed of light, h the Planck constant, and N the number of photon

1559-128X/21/010020-04 Journal © 2021 Optical Society of America

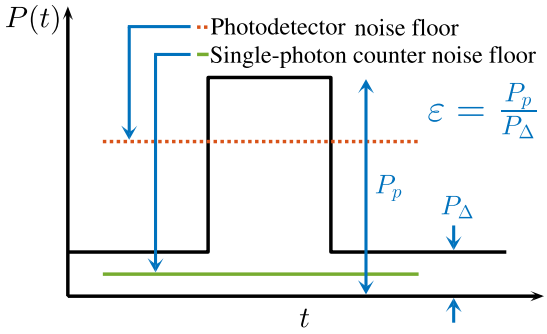

Fig. 1. Square pulse parameters definition.

counts. In comparison, low-noise photodetectors can exhibit a minimum detectable power down to 10^{-9} W. The low SPC noise floor allows for the measurement of the pulse peak power using attenuators and of the pulse pedestal power, enabling a better characterization of the extinction ratio in high-ε pulses, as depicted in Fig. 1.

In this paper, we measure the extinction ratio of high-ε optical pulses generated by the nonlinear Kerr effect for general fiber sensing applications and report an ε enhancement of 100.1 dB. First, we experimentally demonstrate the measurement of a 10 ns optical pulse exhibiting a 120.1 dB extinction ratio, using a SPC. Then, we discuss the origin of the residual noise floor. Such a technique would allow for the characterization of pulses with high extinction ratios.

2. MEASUREMENT OF HIGH EXTINCTION RATIO

We previously demonstrated that a pulse-shaped sinusoidally modulated optical signal undergoing the nonlinear Kerr effect generates sidebands, and pulses with a theoretically high ε are obtained when extracting a high-order sideband [12]. However, the measurements of ε enhancement within the generated sidebands were limited at $\epsilon = 66.4$ dB due to the noise floor of the optical signal analyzer. To reliably measure the extinction ratio of a high-ε pulse, we developed the measurement setup presented in Fig. 2 utilizing a photon counter. A 1550.196 nm coherent continuous-wave (CW) signal is generated by a low phase-noise laser (NP Photonics FLS-25-3-1550-12) and is amplified using an erbium-doped fiber amplifier (EDFA, Amonics AEDFA-C-30B). An electro-optic modulator (EOM, OC-192) modulates the laser signal with a sinusoidal modulation, $f_m = 8.89$ GHz. A second EOM (OC-192) then applies a 10 ns square pulse on the laser signal, with a 50 kHz repetition rate and a 20 dB extinction ratio. The signal is then filtered by a dual-grating filter, aligned with the sinusoidally modulated laser spectrum, with central wavelengths of $\lambda_1 = 1550.110$ nm and $\lambda_2 = 1550.268$ nm. The power of the signal is then boosted using a high-power EDFA (Amonics AEDFA-33) and refiltered by the inverted version of the same dual-grating filter to equalize the optical paths before the nonlinear medium and further reduce any residual carrier frequency. The signal is then launched into a Kerr medium composed of a 2-km long dispersion-shifted fiber, with a zero-dispersion wavelength of 1552 nm, to experience SPM by the nonlinear Kerr effect. The sixth-order SPM-generated sideband is extracted using a bandpass filter (BPF, TFC-C-Band) with a 3 dB bandwidth of 3 GHz. The high-ε pulse then passes through a cascade of attenuators (EXFO FVA-3100), and photons are collected by the low-noise synchronous SPC (id220-FR-SMF) over a photon-detection window of 100 ms, synchronized with the pulse repetition rate.

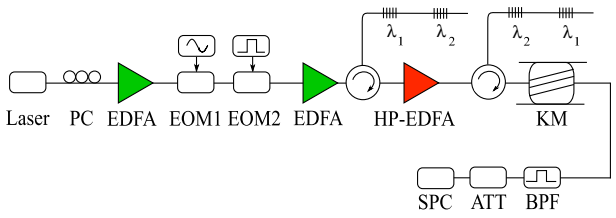

Fig. 2. Schematic of the pulse's high extinction ratio measurement setup. ATT, variable attenuator; BPF, bandpass filter; EDFA, erbium-doped fiber amplifier; EOM, electro-optical modulator; HP-EDFA, high-power EDFA; KM, Kerr medium, PC, polarization controller; SPC, single-photon counter.

To ensure the reliability of the measured power levels, we ensure that each electrical pulse originating from the single-photon detector represents a single photon. The total attenuation provided by a cascade of variable attenuators is increased using 3 dB steps, as shown in Fig. 3, and the measurement is reliable if the number of photons is half its previous value after each step. The reliable measurement baseline is reached after applying 121 dB of attenuation on the signal peak power, corresponding to a photon count of $N_{\text{base}} \simeq 245$ photons, as shown in Fig. 3. Decreasing the signal power by 3 dB beyond a count of N_{base} leads to a photon count different from half its current value, as can be observed in Fig. 3; therefore, measurements performed beyond a count of N_{base} are not reliable.

To measure the pedestal power of the optical pulse, P_Δ, in Fig. 1, the square pulse modulation of EOM2 in Fig. 2 is disabled, the attenuators are bypassed, and the number of photons is recorded. Because the generation of sidebands is much weaker, the number of collected photons after the BPF arises from the leaked power of all optical elements in the setup and acts as a reference level. The number of photons per measuring window corresponding to P_Δ is recorded over 700 times using the setup

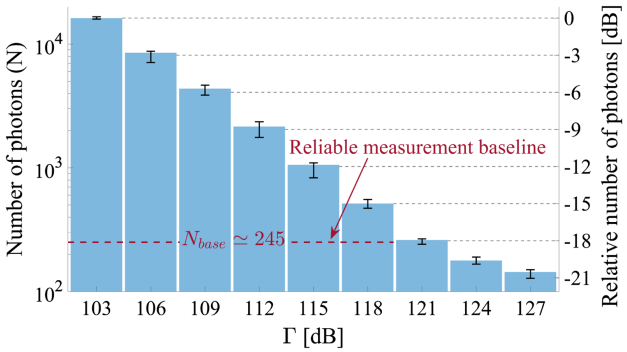

Fig. 3. Measurement of photon counts while applying 3 dB steps attenuation to the high-ε pulse peak power. The bars and the error bars, respectively, represent the average number of collected photons and the extreme values of counts for a given attenuation.

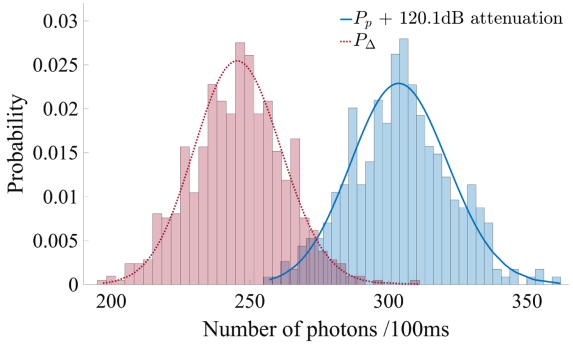

Fig. 4. Poisson distribution fit of the pulse pedestal photon count (in dotted red line) and of the photon count corresponding to the pulse peak power signal attenuated by 120.1 dB (in solid blue line).

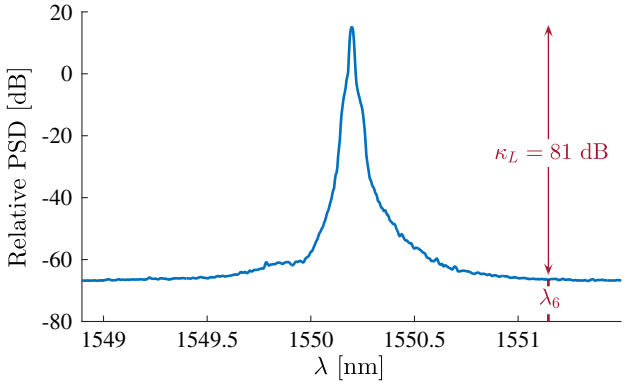

Fig. 5. Laser relative power spectral density and laser contrast κ_L at λ_6.

presented in Fig. 2. The results are fitted with a Poisson distribution and displayed with a dotted red line in Fig. 4, where the average of the distribution is located around 246 photons per 100 ms, coinciding with the result obtained in Fig. 3.

The pulse peak power is then measured when enabling the square pulse modulation on EOM2 in Fig. 2. A strong frequency component is thus generated at the central frequency of the BPF in Fig. 2, and an optical pulse exits the filter. The variable attenuators are connected, and the path attenuation Γ is increased. Measuring the maximal peak power attenuation must be performed while maintaining a photon count higher than 245 over 100 ms in this experiment. The attenuation is increased until a photon count equivalent to P_Δ is reached, in which case $P_p = P_m + \Gamma[\mathrm{dB}]$, where P_m is the measured power. When P_m is made equal to P_Δ, Γ is equivalent to the pulse extinction ratio and is measured to be 120.1 dB. The photon counts are recorded using the same photon counter parameters as for P_Δ, and a Poisson fit is presented in Fig. 4 using a solid blue line. We observe that the mean number of photon counts per 100 ms is located at 304 photons. The attenuation cannot be further increased because an extra decibel would mean a multiplication of the number of photons by a factor of 0.8, which places the measurement below N_{base}. The initial extinction ratio of the square pulse modulation provided by the EOM2 in Fig. 2 is 20 dB; thus, the optical pulse extinction ratio enhancement is 100.1 dB.

3. DISCUSSION

The use of an SPC allows for the measurement of high values of optical pulse extinction ratios. However, our measurement of ε is 120.1 dB and does not match the theoretical value of 200 dB corresponding to the sixth-order SPM-generated sideband for an input pulse with an ε of 20 dB. This discrepancy arises due to power leakage through the optical components of the setup, which constitutes the power of the pulse pedestal. Equation (1) estimates the minimum power of the pulse pedestal, accounting for the individual power contributions of each optical component of the setup at the wavelength of the sixth-order sideband, λ_6,

$$P_{\mathrm{min},6} = P_0 - \underbrace{\kappa_L}_{81\ \mathrm{dB}} + \underbrace{G_{\mathrm{EDFA},1}}_{23\ \mathrm{dB}} + \underbrace{D_{\mathrm{EOM1}}}_{-6\ \mathrm{dB}} + \underbrace{D_{\mathrm{EOM2}}}_{-26\ \mathrm{dB}} + \underbrace{G_{\mathrm{EDFA},2}}_{38\ \mathrm{dB}} + \underbrace{D_{C,1}}_{-3\ \mathrm{dB}} + \underbrace{D_{\mathrm{DG},1}}_{-43\ \mathrm{dB}} + \underbrace{G_{\mathrm{HP\text{-}EDFA}}}_{27\ \mathrm{dB}} + \underbrace{D_{C,2}}_{-3\ \mathrm{dB}} + \underbrace{D_{\mathrm{DG},2}}_{-49\ \mathrm{dB}} + \underbrace{D_{\mathrm{BPF}}}_{-3\ \mathrm{dB}}. \quad (1)$$

The laser contribution is expressed as the difference between the laser power P_0 and κ_L, where κ_L is the contrast between P_0 and the power emitted by the laser near λ_6, as shown in Fig. 5. The power gains from the respective first and second EDFAs in Fig. 2 are expressed by $G_{\mathrm{EDFA},1-2}$, $D_{\mathrm{EOM1-2}}$ are the power drops of the respective two EOMs, with EOM2 being in the OFF-state, and $D_{C,1-2}$ representing the insertion loss of the circulators. The power drops and gains near λ_6 of the dual-gratings filters, HP-EDFA, and BPF are, respectively, given by $D_{\mathrm{DG},1-2}$, $G_{\mathrm{HP\text{-}EDFA}}$, and D_{BPF}. Since $P_0 = 15$ dBm, and the measured power contributions of each optical element are expressed in Eq. (1), the minimum power present at the sixth-order sideband is $P_{E,6} = P_0 - 126\ \mathrm{dB} = -111$ dBm. Therefore, as the peak power of the high-ε pulse is 14.8 dBm, the extinction ratio of the setup presented in Fig. 2 is estimated to be $\varepsilon_{\mathrm{estimate}} = P_p - P_{\mathrm{min},6} = 125.8$ dB, which is close to the measured value of 120.1 dB. Since the power contribution of the dual-gratings filters is superior to the contribution of their preceding amplifiers, the measured extinction ratio can be made closer to the theoretical limit by cascading multiple stages of amplifiers and dual-gratings filters before the signal enters the Kerr medium.

4. CONCLUSION

We present the measurement of high-ε pulses generated by SPM using a single-photon counting method. An all-optical extinction ratio improvement of 100.1 dB for pulses with a duration in the nanosecond regime is demonstrated, and the measurement requires the use of a SPC as detector rather than a conventional photodetector. Nanosecond pulses with high extinction ratio are critical in OTDR fiber sensing because they significantly reduce the noise in backscattering traces from a FUT and allow for better sensing performances, especially for long sensing lengths where coherent Rayleigh scattering limits the spatial resolution.

Funding. Canada Research Chairs (950-231352); Natural Sciences and Engineering Research Council of Canada (7RGPIN-2020-06302).

Acknowledgment. The authors are thankful to ID Quantique for their partnership and support.

Disclosures. The authors declare no conflicts of interest.

REFERENCES

1. H. F. Taylor and C. E. Lee, "Apparatus and method for fiber optic intrusion sensing," U.S. Patent 5,194,847 (16 March 1993).
2. D. A. Krohn, T. MacDougall, and A. Mendez, *Fiber Optic Sensors: Fundamentals and Applications*, 4th ed., Vol. PM247 of SPIE Press Monograph (SPIE Press, 2014).
3. A. Morsali, S. Lecler, P. M. Pelletier, and P. Pfeiffer, "Significance of high extinction ratio laser pulse generation in coherent optical time domain reflectometry," in *Optical Sensing and Detection VI*, F. Berghmans and A. G. Mignani, eds. (SPIE, 2020), p. 30.
4. H. Iribas, J. Mariñelarena, C. Feng, J. Urricelqui, T. Schneider, and A. Loayssa, "Effects of pump pulse extinction ratio in Brillouin optical time-domain analysis sensors," Opt. Express **25**, 27896–27912 (2017).
5. V. Lecoeuche, D. J. Webb, C. N. Pannell, and D. A. Jackson, "Transient response in high-resolution Brillouin-based distributed sensing using probe pulses shorter than the acoustic relaxation time," Opt. Lett. **25**, 156–158 (2000).
6. H. F. Martins, S. Martin-Lopez, P. Corredera, M. L. Filograno, O. Frazão, and M. González-Herráez, "Coherent noise reduction in high visibility phase-sensitive optical time domain reflectometer for distributed sensing of ultrasonic waves," J. Lightwave Technol. **31**, 3631–3637 (2013).
7. M. Ren, D.-P. Zhou, L. Chen, and X. Bao, "Influence of finite extinction ratio on performance of phase-sensitive optical time-domain reflectometry," Opt. Express **24**, 13325–13333 (2016).
8. F. Uyar, T. Onat, C. Unal, T. Kartaloglu, E. Ozbay, and I. Ozdur, "A direct detection fiber optic distributed acoustic sensor with a mean SNR of 7.3 dB at 102.7 km," IEEE Photon. J. **11**, 1–8 (2019).
9. S. Camatel, A. L. Rau, and D. J. Blumenthal, "Accurate measurement of high extinction ratios of ultrafast pulsed sources," IEEE Photon. Technol. Lett. **17**, 1917–1919 (2005).
10. A. Argyris, H. Simos, A. Ikiades, E. Roditi, and D. Syvridis, "Extinction ratio improvement by four-wave mixing in dispersion-shifted fibre," Electron. Lett. **39**, 230–232 (2003).
11. J. D. Merlier, G. Morthier, T. V. Caenegem, R. Baets, I. Moerman, and P. V. Daele, "Experimental demonstration of 15 dB extinction ratio improvement in a new 2R optical regenerator based on an MMI-SOA," in *Proceedings 27th European Conference on Optical Communication*, Amsterdam, Netherlands, 30 September–4 October (2001), Vol. **4**, pp. 574–575.
12. C. Baker, B. Vanus, M. Wuilpart, L. Chen, and X. Bao, "Enhancement of optical pulse extinction-ratio using the nonlinear Kerr effect for phase-OTDR," Opt. Express **24**, 19424–19434 (2016).

Chapter 5

All-optical intensity stabilization

The previous chapter demonstrated the validity of the high-ε pulses generation, which is the first regime of operation of our Kerr-based signal processing scheme. The second regime of operation enables the stabilization of an optical signal's intensity, as introduced in Chap. 3. The following manuscript presents the application of this all-optical stabilization technique to reduce the intensity noise contributions in a direct-detection Φ-OTDR setup. To demonstrate the interest of the scheme, we compare our stabilized Φ-OTDR to an equivalent Φ-OTDR setup not utilizing a stabilization technique in a vibration detection scenario. As will be shown in the manuscript, without stabilizing the pulse peak power intensity, the applied vibration remains buried into the background noise and cannot be detected using the conventional trace-to-trace difference presented in Fig. 2.14.

5.1 Experimental demonstration of all-optical intensity stabilization

Research Article Vol. 4, No. 5 / 15 May 2021 / OSA Continuum 1430

All-optical pulse peak power stabilization and its impact in phase-OTDR vibration detection

BENOIT VANUS,* CHAMS BAKER, LIANG CHEN, AND XIAOYI BAO

University of Ottawa, Department of Physics, Ottawa (ON), K1N 6N5, Canada

Abstract: We present an all-optical technique for the stabilization of laser power using the nonlinear Kerr effect and experimentally demonstrate improvement of vibration recovery in direct-detection phase-sensitive optical time domain reflectometry (Φ-OTDR). A pulsed or continuous wave optical signal impressed with a sinusoidal modulation generates sidebands while experiencing self-phase modulation in a nonlinear medium which can be utilized to stabilize the peak power of the signal. By adjusting the peak power at the entrance of the Kerr medium, the signal created at the first order sideband exhibits reduced peak power fluctuations and can be extracted using a band-pass filter. Experimental results show that the generated pulses with stabilized peak power improve vibration detection in a Φ-OTDR with a direct-detection scheme. This technique can be combined with other performance enhancement techniques to allow for the detection of weak signals, and reduces the need of an optoelectronic-based power control loop on a fiber laser.

1. Introduction

Fiber-based lasers exhibit various noises such as intensity noise, frequency noise and phase noise. The frequency and phase noises can be minimized using various techniques such as a Pound-Drever-Hall scheme, a scattering-based scheme or with semiconductor optical amplifier [1–3]. The intensity noise is often minimized using an optoelectronic-based feedback loop which adjusts the pump current or the internal temperature of the laser, or using other techniques such as an external feedforward compensation system [4,5]. However, using a control loop to reduce one noise parameter usually comes at the expense of increasing other noise parameters, especially phase noise. When performing phase-sensitive optical time domain reflectometry (Φ-OTDR), both low laser frequency drift and low power fluctuation are required [6,7]. Φ-OTDR allows for distributed vibration sensing with high sensitivity and is widely applied in seismic sensing, perimeter monitoring and structural health monitoring [8–10]. As nanosecond pulses from a highly coherent laser source are sent into a sensing fiber, Rayleigh scattering occurs at every point along the fiber and a fraction of the scattered light propagates backward towards the interrogating system. By monitoring the evolution of the backscattered light amplitude, vibrations occurring on the sensing fiber can be located and characterized [11,12]. To improve the detection of events in Φ-OTDR, the signal-to-noise ratio (SNR) of the system must be increased. This can be achieved through various techniques such as coding-schemes or algorithm-based methods generating up to 14 dB of SNR enhancement, or using a coherent detection technique leading to a 10 dB SNR improvement [13–15]. Another technique uses chirped pulse amplification and an SNR improvement of 20 dB was reported when detecting strain [16]. Φ-OTDR performances can also be enhanced when focusing on the pulse source and it has been demonstrated that a high pulse extinction ratio (ε), defined as the pulse peak power divided by the power at the pedestal of the pulse, leads to longer detection ranges and improves sensitivity [17,18]. To ensure reliable measurements, Φ-OTDR requires a stable pulse peak power. Stabilization of pulses in the femtosecond regime has been demonstrated in free-space optics using self-phase modulation (SPM) and parametric chirped-pulse amplification [19,20].

#409809 https://doi.org/10.1364/OSAC.409809
Journal © 2021 Received 9 Sep 2020; revised 31 Mar 2021; accepted 14 Apr 2021; published 26 Apr 2021

OSA CONTINUUM

In this paper, we present an all-optical pulse peak power stabilization technique using SPM and demonstrate its interest in Φ-OTDR vibration detection. First, we illustrate how to achieve a power fluctuation reduction using the nonlinear Kerr effect. Second, we present a theoretical model for the principle of power fluctuation reduction. Third, we experimentally demonstrate pulse peak power stabilization with a pulse duration in the nanosecond regime. We apply the stabilized pulses to a Φ-OTDR direct-detection scheme and demonstrate a vibration detection improvement. This all-optical process replaces intensity stabilization feedback loops on the laser and thus allows for higher laser phase stability. Moreover, this SPM-based method can be combined with other modulation-based or all-optical SNR-enhancement techniques as well as with all-optical laser stabilization techniques to further improve the performances of Φ-OTDR systems.

2. Stabilization of pulsed optical signals

The behaviour of sinusoidally modulated optical signals undergoing the nonlinear Kerr effect allows for all-optical small signals magnification and high-ε pulse generation both by generating and extracting a specific SPM-generated optical sideband [17,21]. Figure 1 presents the evolution of the relative output power of the first SPM-generated sideband with respect to the nonlinear phase shift ϕ_{SPM}, calculated using $P^{(1)}(\phi_{\mathrm{SPM}})/P_0 = \left[J_1^2(0.5\phi_{\mathrm{SPM}}) + J_2^2(0.5\phi_{\mathrm{SPM}})\right]$ where $P^{(1)}$ is the first order sideband output power, $P_0 = P_p/4$ with P_p the input peak power and $\phi_{\mathrm{SPM}} = \gamma P_p L$ where γ and L are respectively the waveguide nonlinearity parameter and the length of the Kerr medium [17]. The relative first-order output power exhibits a flat region around $\phi_{\mathrm{SPM}}/1\mathrm{rad} = 6.4$ dB, which can be utilized to reduce the peak power fluctuations of an incoming optical signal, F_{in}, defined as $F_{in} = \sigma_P/P_p$ where σ_P is the standard deviation of the peak power varying over time. By fixing the length of the Kerr medium, γ and L are determined and the signal peak power at the entrance of the Kerr medium can be adjusted to match the ϕ_{SPM} condition that minimizes power fluctuations. When the fluctuation minimization condition is satisfied, the power fluctuations of the signal at the first SPM-generated sideband, F_{out}, is reduced as illustrated in Fig. 1. The amount of fluctuation reduction provided by this technique is presented in Fig. 2. Figure 2 shows that, for example, a peak power fluctuation of 0.7 % at the input signal is reduced to 0.012 % at the output of the first SPM-generated sideband, as illustrated by the dashed yellow lines in Fig. 2. The relationship between F_{out} and F_{in} is fitted by a second order polynomial to obtain a simple analytical formula describing the theoretical power fluctuation reduction provided by the proposed technique.

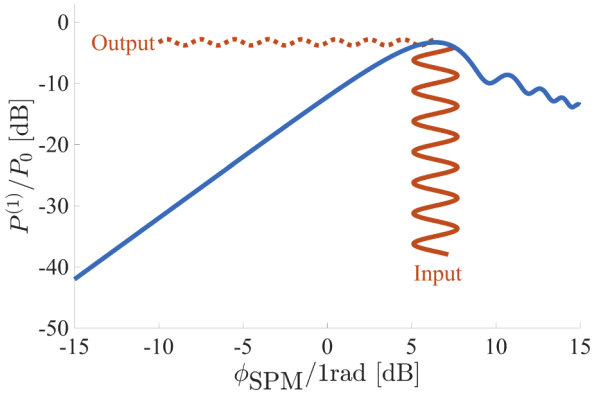

Fig. 1. Relative output intensity of the first sideband as a function of the nonlinear phase shift, ϕ_{SPM}. Also illustrated is the reduction of the input signal power variation.

OSA CONTINUUM

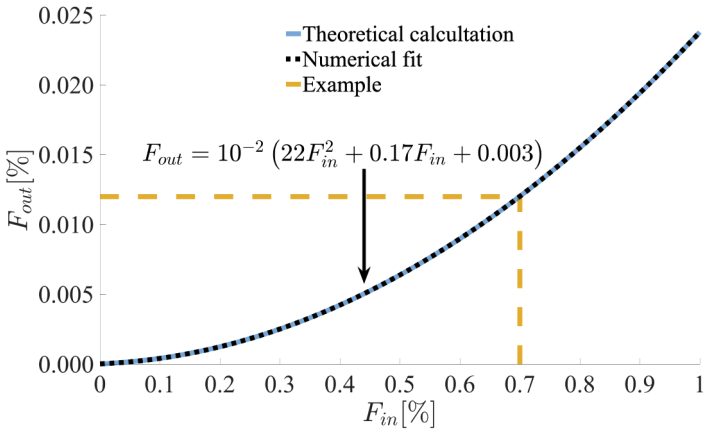

Fig. 2. Reduction of input peak power fluctuation provided by the first SPM-generated sideband around ϕ_{SPM} = 6.4 dB/1rad.

3. Experimental setup and results

The advantage of the proposed power fluctuation reduction approach is experimentally demonstrated by comparing the vibrations detected using stabilized and non-stabilized pulses in the direct-detection Φ-OTDR setup presented in Fig. 3. A coherent continuous light at 1550.196 nm is generated by a low phase-noise laser (NP Photonics FLS-25-3-1550-12) and is amplified using an erbium-doped fiber amplifier (EDFA, Amonics AEDFA-C-30B). A polarization controller (PC) then ensures the alignment of the light polarization with the main polarization axis of the following electro-optic modulators (EOMs). A non-stabilized optical pulse is generated by following the dashed line from point *a* to point *b* in Fig. 3. In this case, two cascaded EOMs (EOM3 and EOM4, Photoline S/N: 3604-14) generate a 10 ns pulse with an extinction ratio equal to 60 dB±2 dB [22] at a 20-kHz repetition rate. The non-stabilized pulse is amplified by an EDFA (Amonics AEDFA-PA-25-B-FA) and filtered using a band-pass filter (BPF, TFC-C-Band), with a 3 dB bandwidth of 3 GHz, to reduce the amplified spontaneous emission noise. The generation of pulses with stabilized peak power is presented in Fig. 3 following the solid line between points *a* and *b*. The light at point *a* passes through a first EOM (EOM1, OC-192) applying an 8.825 GHz sinusoidal modulation, then through a second EOM (EOM2, OC-192) applying a 10 ns pulse originating from the same function generator (Tektronix AFG3252) using the same pulse duration and repetition rate as the non-stabilized case. The light is then amplified using an EDFA (Amonics AEDFA-PA-25-B-FA) and filtered using a dual-grating filter (λ_1 = 1550.110 nm and λ_2 = 1550.268 nm). The pulse power is then increased by a high-power EDFA (HP-EDFA, Amonics AEDFA-33) and the light is re-filtered by an inverted version of the dual-grating filter before entering the Kerr medium (KM) composed of a 2-km dispersion-shifted fiber. The pulse experiences SPM in the KM leading to the generation of sidebands and the first order sideband is extracted using a BPF (TFC-C-Band). The amount of amplification is adjusted to match the ϕ_{SPM} condition presented in Fig. 1. The extinction ratio of the stabilized pulse is 54 dB. The difference in ε between stabilized and non-stabilized pulses has no impact on our measurements. The amount of amplification provided to the non-stabilized pulse is also adjusted so that at point *b* in Fig. 3 both stabilized and non-stabilized pulses exhibits a 14 dBm peak power. After point *b*, pulses are amplified by an EDFA (Amonics AEDFA-PA-25-B-FA) operated away from the saturation regime and sent to a 4-km FUT through a circulator. A piezoelectric transducer (PZT) located at the end of the FUT produces a 2-kHz vibration on 2 m of fiber wrapped around it. A fraction of the pulse power propagates backwards due to Rayleigh scattering and is amplified by

OSA CONTINUUM

a high-gain EDFA (HG-EDFA, Amonics APEDFA-C-10-B-FA). The backscattered light is then filtered by a band-pass filter (TFC-C-Band) before being detected by a low-noise photodetector (New Focus 1811- IR DC 125MHz) and captured by an oscilloscope (LeCroy 64Xi-A).

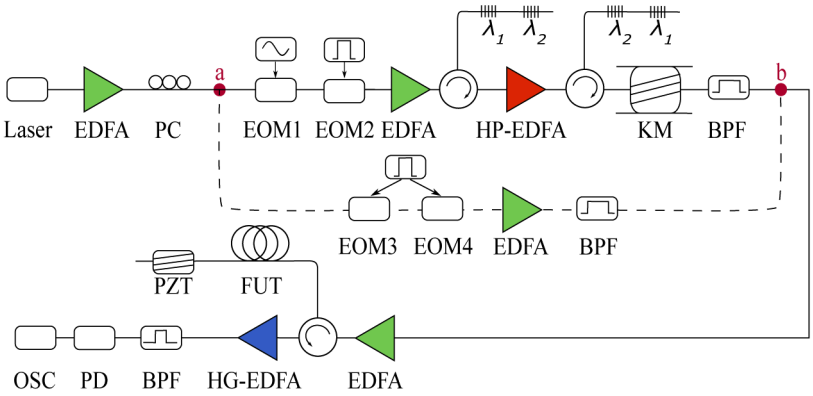

Fig. 3. Schematic of the setup to measure optical pulse's peak power fluctuation reduction. ATT: Variable, Attenuator, BPF: Band-Pass Filter, EDFA: Erbium-Doped Fiber Amplifier, EOM: Electro-Optical Modulator, HG-EDFA: High-gain EDFA, HP-EDFA: High-power EDFA, KM: Kerr Medium, OSC: Oscilloscope, PD: Photodiode.

To demonstrate the peak power fluctuation reduction provided by the proposed approach, stabilized and non-stabilized pulses with a duration of 100 ns are generated and measured at point *b* in Fig. 3. A set of 400 traces is recorded in both cases and the measured fluctuations of the pulses peak power are presented in Fig. 4 where the original non-stabilized pulse is presented in dashed blue line and the stabilized first-order pulse is in solid blue line. The percentage of fluctuation is measured on the flatter part of the pulse to avoid transient power variations imposed by the function generator at the pulse edges. Figure 4 shows a clear reduction of the peak power fluctuation when stabilizing using the proposed approach. The amount of fluctuation reduction presented in Fig. 4 is consistent with the amount predicted by the example in Fig. 2 after taking the 8 mV measurement resolution of the oscilloscope into consideration, corresponding to 0.26 % of the peak voltage. A laser exhibiting large intensity noise is utilized to better demonstrate the peak power fluctuation reduction provided by the proposed approach.

Figure 5 presents experimental vibration detection results from direct-detection Φ-OTDR systems with and without stabilization, respectively shown in red and blue. Figures 5(a) and (e) respectively show overlapped backscattering traces from 10-ns pulses for the non-stabilized and stabilized intensity cases. A sliding window average is applied on each backscattering trace to improve locating the vibration [11]. Figures 5(b) and (f) present the conventional trace-to-trace difference [11] for the non-stabilized and stabilized backscattering traces, respectively. The intensity fluctuations of the non-stabilized pulse prevent locating the vibration as observed in Fig. 5(b). When stabilizing the pulse, the amplitude fluctuations in the backscattering traces are reduced by a factor of 1.95, in close agreement with the results from Fig. 4, which allows for detecting the vibration location, as shown in Fig. 5(f). To reliably locate the vibration, the difference between each trace and the average of all traces is calculated and the results for the non-stabilized and stabilized cases are presented in Fig. 5(c) and (g), respectively, showing that the vibration is located at 4.09 km. The detected vibration and scaled version of the signal driving the PZT are presented in Fig. 5(d) and (h) for the non-stabilized and stabilized cases respectively, and show 11 cycles over 5.5 ms, corresponding to the 2-kHz vibration applied by the PZT. The vibration location cannot be identified in Fig. 5(c) corresponding to the case of non-stabilized

OSA CONTINUUM

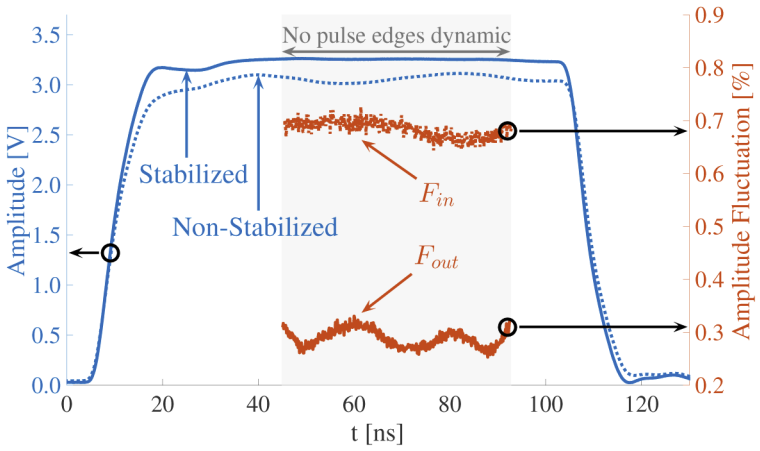

Fig. 4. Measured original non-stabilized and stabilized 100 ns pulses. The black circles and their associated arrows indicate the axis of reference for the corresponding traces.

pulses but can be identified in Fig. 5(g) corresponding to the case of stabilized pulses, which demonstrates the practicality of this stabilization technique.

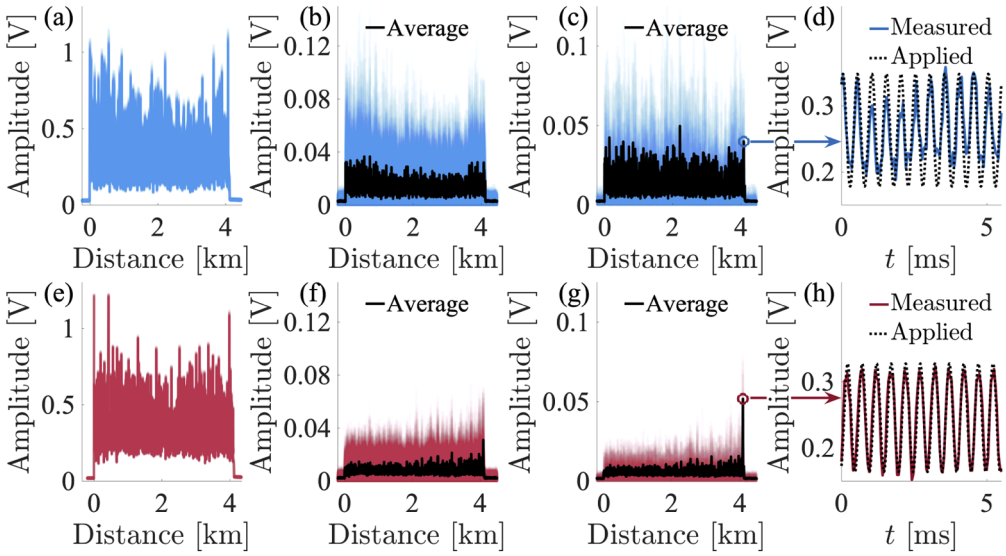

Fig. 5. Comparison of Φ-OTDR vibration detection in the non-stabilized and stabilized scenarios, respectively in blue and red: a) Non-stabilized overlapped backscattering traces, b) Overlap of trace-to-trace difference in the non-stabilized scenario, c) Overlap of the difference to the average trace in the non-stabilized scenario, d) Detected vibration from the non-stabilized scenario and scaled PZT driving signal, e) Stabilized overlapped backscattering traces, f) Overlap of trace-to-trace difference in the stabilized scenario, g) Overlap of the difference to the average trace in the stabilized scenario, h) Detected vibration from the stabilized scenario and scaled PZT driving signal.

OSA CONTINUUM

4. Discussion

The proposed all-optical power fluctuation reduction approach is not limited to pulse peak powers and can also be applied to sinusoidally modulated continuous wave lasers. We utilize optical pulses to mitigate the generation of Brillouin scattering in the Kerr medium which would drain the signal power and limit the achievable nonlinear phase shift. Optical pulses also allow for achieving higher peak power and ease achieving the optimal ϕ_{SPM} value to satisfy the power fluctuation reduction condition. For initial power fluctuations below 1 % of their reference power, this technique allows for a reduction of power fluctuations by a factor of at least 40 as can be observed in Fig. 2. The proposed all-optical technique replaces optoelectronic feedback loops on the laser and thereby eliminates their impact on phase noise and improves Φ-OTDR performance.

A photodetector with low detection threshold is required to reduce the intensity noise observed in the backscattering traces from Fig. 5(a) and (e). Such photodetector allows for the reduction of signal amplification provided by the HG-EDFA in Fig. 3 and therefore minimizes the intensity noise added by this amplification stage [23]. The amplifier present before the FUT in Fig. 3 can be bypassed if the length or the γ parameter of the Kerr medium are tuned to match a required output peak power. For example, a shorter Kerr medium requires a higher input peak power to achieve the optimal ϕ_{SPM} value and therefore induces a higher peak power at the first order sideband, as shown in Fig. 1.

5. Conclusion

We present a new all-optical technique for stabilizing the peak power of an optical signal by tuning the amount of SPM experienced by a sinusoidally modulated optical signal entering a Kerr medium and extracting the first order sideband that is generated by SPM. The advantage of this technique is demonstrated using a Φ-OTDR direct-detection scheme to detect vibrations applied on a fiber at a 4-km distance. We experimentally demonstrated a trace-to-trace amplitude fluctuation reduction using our stabilization technique, which allows for locating vibrations that could not be located in the case of non-stabilized laser power. This all-optical technique can also be combined with other Φ-OTDR performance enhancing techniques for broader sensing capabilities.

Funding. Canada Research Chairs (950-231352); Natural Sciences and Engineering Research Council of Canada (7RGPIN-2020-06302).

Disclosures. The authors declare no conflicts of interest.

References

1. R. W. P. Drever, J. L. Hall, F. V. Kowalski, J. Hough, G. M. Ford, A. J. Munley, and H. Ward, "Laser phase and frequency stabilization using an optical resonator," Appl. Phys. B **31**(2), 97–105 (1983).
2. B. Saxena, X. Bao, and L. Chen, "Suppression of thermal frequency noise in erbium-doped fiber random lasers," Opt. Lett. **39**(4), 1038 (2014).
3. C. Li, S. Xu, X. Huang, Y. Xiao, Z. Feng, C. Yang, K. Zhou, W. Lin, J. Gan, and Z. Yang, "All-optical frequency and intensity noise suppression of single-frequency fiber laser," Opt. Lett. **40**(9), 1964 (2015).
4. M. Heurs, V. M. Quetschke, B. Willke, K. Danzmann, and I. Freitag, "Simultaneously suppressing frequency and intensity noise in a Nd:YAG nonplanar ring oscillator by means of the current-lock technique," Opt. Lett. **29**(18), 2148 (2004).
5. L.-S. Fock, A. Kwan, and R. Tucker, "Reduction of semiconductor laser intensity noise by feedforward compensation: experiment and theory," J. Lightwave Technol. **10**(12), 1919–1925 (1992).
6. J. C. Juarez and H. F. Taylor, "Field test of a distributed fiber-optic intrusion sensor system for long perimeters," Appl. Opt. **46**(11), 1968 (2007).
7. X. Zhong, C. Zhang, L. Li, S. Liang, Q. Li, Q. Lü, X. Ding, and Q. Cao, "Influences of laser source on phase-sensitivity optical time-domain reflectometer-based distributed intrusion sensor," Appl. Opt. **53**(21), 4645 (2014).
8. H. F. Taylor and C. E. Lee, "Apparatus and method for fiber optic intrusion sensing," (1993). Library Catalog: Google Patents.
9. K. N. Choi, J. C. Juarez, and H. F. Taylor, "Distributed fiber optic pressure/seismic sensor for low-cost monitoring of long perimeters," in *AeroSense 2003*, E. M. Carapezza, ed. (Orlando, FL, 2003), p. 134.

OSA CONTINUUM

10. M. Filograno, C. Riziotis, and M. Kandyla, "A Low-Cost Phase-OTDR System for Structural Health Monitoring: Design and Instrumentation," Instruments **3**(3), 46 (2019).
11. Y. Lu, T. Zhu, L. Chen, and X. Bao, "Distributed Vibration Sensor Based on Coherent Detection of Phase-OTDR," J. Lightwave Technol. **28**, 3243–3249 (2010).
12. G. Tu, X. Zhang, Y. Zhang, F. Zhu, L. Xia, and B. Nakarmi, "The Development of an Phase-OTDR System for Quantitative Vibration Measurement," IEEE Photonics Technol. Lett. **27**(12), 1349–1352 (2015).
13. C. Bentz, L. Baudzus, and P. Krummrich, "Signal to Noise Ratio (SNR) Enhancement Comparison of Impulse-, Coding- and Novel Linear-Frequency-Chirp-Based Optical Time Domain Reflectometry (OTDR) for Passive Optical Network (PON) Monitoring Based on Unique Combinations of Wavelength Selective Mirrors," Photonics **1**(1), 33–46 (2014).
14. H. He, L. Shao, H. Li, W. Pan, B. Luo, X. Zou, and L. Yan, "SNR Enhancement in Phase-Sensitive OTDR with Adaptive 2-D Bilateral Filtering Algorithm," IEEE Photonics J. **9**(3), 1–10 (2017).
15. Z. Pan, K. Liang, Q. Ye, H. Cai, R. Qu, and Z. Fang, "Phase-sensitive OTDR system based on digital coherent detection," (Shanghai, China, 2011), p. 83110S.
16. J. Pastor-Graells, L. R. Cortés, M. R. Fernández-Ruiz, H. F. Martins, J. Azaña, S. Martin-Lopez, and M. Gonzalez-Herraez, "SNR enhancement in high-resolution phase-sensitive OTDR systems using chirped pulse amplification concepts," Opt. Lett. **42**(9), 1728 (2017).
17. C. Baker, B. Vanus, M. Wuilpart, L. Chen, and X. Bao, "Enhancement of optical pulse extinction-ratio using the nonlinear Kerr effect for phase-OTDR," Opt. Express **24**(17), 19424 (2016).
18. F. Uyar, T. Onat, C. Unal, T. Kartaloglu, E. Ozbay, and I. Ozdur, "A Direct Detection Fiber Optic Distributed Acoustic Sensor With a Mean SNR of 7.3 dB at 102.7 km," IEEE Photonics J. **11**(6), 1–8 (2019).
19. A. Špaček, J. T. Green, F. Batysta, J. Novák, R. Antipenkov, P. Bakule, and B. Rus, "General method of passive optical pulse peak intensity stabilization through controlled self-phase modulation and over-compression," J. Opt. Soc. Am. B **35**(10), 2494 (2018).
20. R. Riedel, M. Schulz, M. J. Prandolini, A. Hage, H. Höppner, T. Gottschall, J. Limpert, M. Drescher, and F. Tavella, "Long-term stabilization of high power optical parametric chirped-pulse amplifiers," Opt. Express **21**(23), 28987 (2013).
21. B. Vanus, C. Baker, L. Chen, and X. Bao, "All-optical intensity fluctuation magnification using Kerr effect," Opt. Express **28**(3), 3789 (2020).
22. M. Ren, D.-P. Zhou, L. Chen, and X. Bao, "Influence of finite extinction ratio on performance of phase-sensitive optical time-domain reflectometry," Opt. Express **24**(12), 13325 (2016).
23. A. W. S. Putra, M. Yamada, H. Tsuda, and S. Ambran, "Theoretical Analysis of Noise in Erbium Doped Fiber Amplifier," IEEE J. Quantum Electron. **53**(4), 1–8 (2017).

5.2 Additional comments

As observed in Fig. 3 of the previous manuscript, an EDFA is present after the laser and could arguably increase the intensity noise of the laser source. However, this EDFA was necessary to counter the loss induced by the cascaded EOMs, and was present in both stabilized and non-stabilized cases. Therefore, this amplifier does not have an impact on the final conclusions. It would be possible to remove this EDFA if the laser in use was capable of generating a sufficiently high output power to pass through the EOMs and still be within the input power range of the following amplifier, or by using EOMs with a lower insertion loss. It must also be mentioned that the laser used in the experiment (NP Photonics FLS-25-3-1550-12) was intentionally running without an intensity stabilization control-loop, thus producing higher laser intensity fluctuations. The exaggerated intensity noise allowed us make our stabilization technique visible and detectable given the photodetector and oscilloscope in use.

Chapter 6

All-optical signal magnification

The two previous chapters each demonstrated achievable all-optical signal processing schemes based on sinusoidally-modulated optical signals undergoing the nonlinear Kerr effect. This chapter presents another all-optical signal processing technique that can be reached using the same physical process and corresponding to the third regime of operation presented in Chap. 3. All-optical magnification occurs when the nonlinear phase-shift induced in the Kerr medium satisfies the the so-called linear regime of the transfer function of the extracted sideband, as shown in Fig. 3.12. If a fiber sensor's response to an external perturbation is too weak to be detected, one may simply amplify the input light or amplify the sensors' response. However, the first option may induce undesired nonlinear effects while the second amplifies any background signal and is limited by the saturation level of the photodetector. Therefore, and as will become clear with the first figure of the following manuscript, a signal magnification technique is required for enhancing the contrast in the sensor's response and bringing it into a detectable range without reaching the photodetector saturation. We thus propose an all-optical magnification scheme based on self-phase modulation to increase the contrast in the response of a fiber sensor to an external perturbation. The following manuscript serves as a proof of concept for all-optical magnification as the signal to be magnified is known.

6.1 Experimental demonstration all-optical signal magnification

Research Article | Vol. 28, No. 3 / 3 February 2020 / Optics Express 3789

Optics EXPRESS

All-optical intensity fluctuation magnification using Kerr effect

BENOIT VANUS,* CHAMS BAKER, LIANG CHEN, AND XIAOYI BAO

Universit_o Ottawa, Department of Physics, Ottawa (ON), K1N 6N5, Canada

Abstract: We present a new all-optical method for the magnification of small-intensity fluctuations using the nonlinear Kerr effect. A fluctuation of interest is impressed onto a sinusoidally modulated optical signals (SMOS) and spectral sidebands are generated as the SMOS experiences self-phase modulation in a nonlinear medium. Magnification of these temporal variation is obtained by filtering one of the sidebands. For small fluctuations, the amount of magnification obtained is proportional to $(2m+1)$, with m being the sideband order. This technique enhances fiber-based point sensor capabilities by bringing signals originally too small to be detected into the detection range of photodetectors.

1. Introduction

Most optical intensity based sensors, such as a Mach-Zehnder interferometer [1–4] exhibit a sinusoidal power dependance to a parameter of interest, such as strain or temperature, as illustrated in Fig. 1(a). If the intensity fluctuation that results from the measured parameter variation is too weak to be detected, illustrated as a sinusoidal signal in Fig. 1(b), an amplifier, such as an erbium-doped fiber amplifier, is utilized to amplify the intensity of the fluctuation to a detectable level. However, this leads to the amplification of both the useful signal and its offset, the latter is defined as the optical power level at the base of the signal of interest, as illustrated in Fig. 2. This can lead to a saturation of the photodetector because the intensity becomes higher

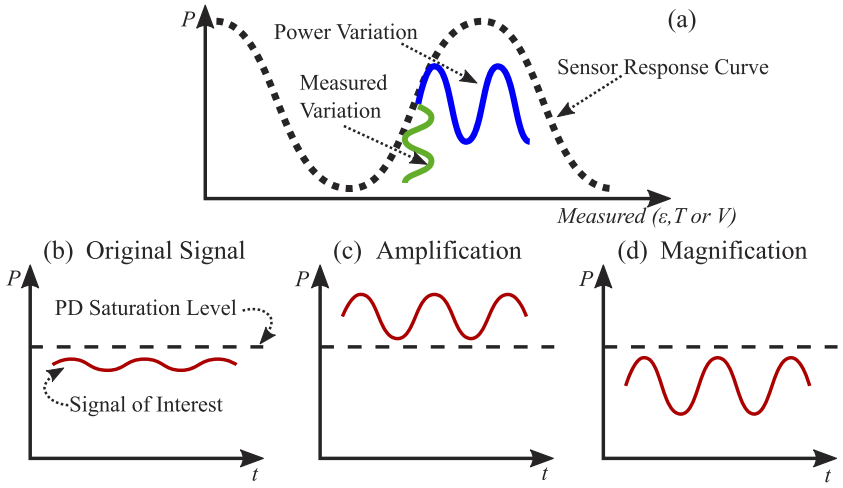

Fig. 1. Illustration of the amplification and magnification of small intensity fluctuations. ϵ: Strain, P: Power, PD: Photodetector, T: Temperature, V: Voltage. a) Optical sensor operating at the quadrature point, b) The original signal power with respect to the PD saturation level, c) The amplified signal is above the saturation level and can not be detected, d) The magnified signal is below the saturation level and can be detected.

#384004 https://doi.org/10.1364/OE.384004
Journal © 2020 Received 25 Nov 2019; revised 11 Jan 2020; accepted 14 Jan 2020; published 27 Jan 2020

Optics EXPRESS

than the saturation level of the photodetector, as illustrated in Fig. 1(c) where the dashed line represents the saturation level. Hence there exist a maximum amplification beyond which the signal can not be detected. To extract a small fluctuation and remain below the photodetector saturation limit, a magnification of the signal of interest must be combined with a reduction of its offset, as presented in Fig. 1(d). A solution to this issue can be found using nonlinear optical processes as some allow for optical signal reshaping and reamplification based on self-phase modulation (SPM) [5–8] and for general all-optical signal processing when including cross-phase modulation, three and four wave mixing processes [9].

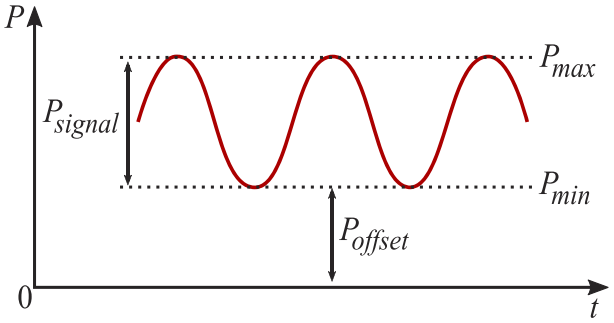

Fig. 2. Illustration of the signal parameters, defining the maximum and minimum powers as well as the signal offset power.

In this paper, we propose and demonstrate the use of SPM to magnify a signal intensity fluctuation and reduce its offset power to prevent photodetector saturation. First, we present the theory behind optical signal magnification and define the signal contrast. Then, we predict the magnification factor of the signal contrast for small amplitude signals. Finally, we present an experimental setup generating all-optical small signals magnification and show a close agreement between theoretical predictions and experimental results.

2. Magnification of optical signals

It has been demonstrated that spectral sidebands are generated through SPM if a sinusoidally modulated optical signal (SMOS) featuring a high peak power undergoes the nonlinear Kerr effect [10,11]. All-optical signal magnification using the nonlinear Kerr effect is achieved by operating at power levels exhibiting an exponential relationship between powers of the input signals propagating through the Kerr medium and the generated sidebands. By adjusting the peak power of the signal sent into the Kerr medium, any deviations from the original power profile will get magnified. The maximum power of the signal P_{max} is defined as the peak power of the signal, the minimum power P_{min} as the power at the troughs which also corresponds to the offset power of the signal P_{offset} , and the signal's magnitude P_{signal} is defined as the difference $P_{max} - P_{min}$, as illustrated in Fig. 2. The signal contrast at the input of the Kerr medium, ρ_{in}, is expressed as :

$$\rho_{in} = \frac{P_{max} - P_{min}}{P_{min}} \tag{1}$$

Based on Fig. 2, the total power is described as the sum of the offset power and the signal power: $P_{tot} = P_{offset} + P_{signal}$. Therefore, ρ_{in} can be expressed as:

$$\rho_{in} = \frac{P_{offset} + \max\{P_{signal}\}}{P_{offset}} - 1. \tag{2}$$

Figure 3 shows a linear dependance at small nonlinear phase shift $\phi_{SPM} = \gamma P_p L$, in the logarithmic scale, of each SPM-generated sideband relative output power variation ($P^{(m)}/P^{(0)}$), where m is

Optics EXPRESS

the sideband order, γ is the waveguide nonlinearity parameter, P_p is the signal peak power and L is the length of the nonlinear medium. In this regime, any fluctuation in the initial peak power leads to a variation in ϕ_{SPM} and thus leads to a magnification of this fluctuation impressed on the power of the sidebands. A linear regression with a slope of $2m$ is fitted to each sideband order and shows good agreement for small signals, as presented in Fig. 3. Therefore we can approximate that, for small power variations, the relative output power variation is proportional to the $2m$ power of the nonlinear phase shift: $P^{(m)}/P^{(0)} \propto \phi_{SPM}^{(2m)}$. Moreover, by operating at a low power regime, it can also be approximated that the input signal power is equivalent to the power of the 0^{th} order sideband: $P_{in} \approx P^{(0)}$; therefore, as the input power is proportional to the peak power, $\phi_{SPM} \propto P_{in}$, we have that $P^{(m)}/P_{in} \propto P_{in}^{(2m)}$. Thus the power of the m^{th} order sideband is proportional to the input power raised to the power of $(2m+1)$:

$$P^{(m)} \propto P_{in}^{(2m+1)}. \tag{3}$$

The contrast of the m^{th} order sideband is expressed as:

$$\begin{aligned} \rho_{out} &= \frac{\left(P_{offset} + \max\{P_{signal}\}\right)^{2m+1}}{P_{offset}^{2m+1}} - 1 \\ \rho_{out} &= \left(1 + \frac{\max\{P_{signal}\}}{P_{offset}}\right)^{2m+1} - 1 \end{aligned} \tag{4}$$

For small signal fluctuations, $(2m+1) \cdot \left(\max\{P_{signal}\}/P_{offset}\right) \ll 1$, Eq. (4) can be expanded as a Taylor series limited to the first order, leading to:

$$\begin{aligned} \rho_{out} &\approx (2m+1)\frac{\max\{P_{sig}\}}{P_{off}} + \ldots \\ \rho_{out} &\approx (2m+1)\rho_{in} \end{aligned} \tag{5}$$

Equation (5) shows that in a small signals regime, the m^{th} order sideband contrast will be magnified by a $(2m+1)$ factor with respect to the input signal contrast.

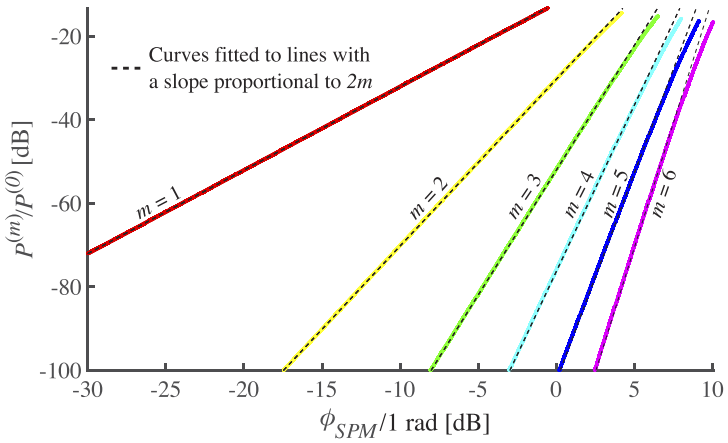

Fig. 3. Relative output intensity for each sideband as a function of the nonlinear phase shift (ϕ_{SPM}) using the equation $P^{(m)}(\phi_{SPM}) = P_0\left[J_m^2(0.5\phi_{SPM}) + J_{m+1}^2(0.5\phi_{SPM})\right]$ [11], fitted with a slope proportional to $2m$, with m being the sideband order, $P_0 = P_p/4$ and P_p the input signal's peak power.

Optics EXPRESS

3. Experimental setup and results

Figure 4 presents a schematic of the signal magnification system. A 1550.12 nm light is generated by a distributed continuous wave (CW) feedback laser (AOI DFB-934-BF-10-EC-Fx-Hx-N126) and gets amplified using an erbium-doped fiber amplifier (EDFA, Amonics AEDFA-C-30B). An electro-optic modulator (EOM, OC-192) applies a 100 ns square pulse modulating the CW light with a repetition rate of 100 kHz. This pulse modulation prevents the formation of accumulated Brillouin effect in the Kerr medium which would lead to a decrease of the laser signal power at the original wavelength, hence preventing the SPM process to occur. A second EOM (OC-192) then applies a 4 MHz sinusoidal modulation on the pulse peak power to emulate the power fluctuation to be magnified. Finally a third EOM (OC-192) applies a 9.2 GHz sinusoidal modulation on the overall signal, creating an SMOS. The modulated overall signal is then amplified and filtered by two cascaded fiber Bragg gratings (FBGs) centered at λ_1=1550.058 nm and λ_2= 1550.202 nm. Power is then boosted using a high-power EDFA (Amonics EDFA033) before undergoing a second filtration step. This step allows to further remove any residual carrier contributions and equalize optical paths by using a mirrored version of the initial FBG filter. The light then experiences SPM in a 2-km long dispersion-shifted fiber, with a zero dispersion wavelength of 1550.2 nm. The SPM generates sidebands at the output of the Kerr medium [11] and the first and second order sidebands are respectively extracted using a band-pass filter with a 3 dB bandwidth of 3 GHz (BPF - TFC-C-Band). The input power of the nonlinear medium is adjusted to maximize the contrast of the signal at the output of the Kerr medium. A low-noise photodetector (New Focus 1811- IR DC 125MHz) interfaces an oscilloscope (LeCroy 64Xi-A) and enables the measurement of the magnified signal.

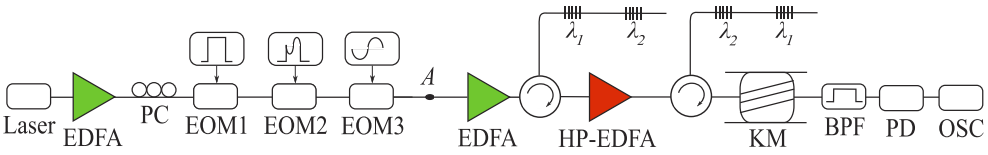

Fig. 4. Schematic of the optical signal magnification experimental setup. BPF: Band-Pass Filter, EDFA: Erbium-Doped Fiber Amplifier, EOM: Electro-Optical Modulator, HP-EDFA: High-Power EDFA, KM: Kerr Medium, OSC: Oscilloscope, PC: Polarization Controller, PD: Photodetector

Using the setup presented in Fig. 4, we first apply a 1V modulation on EOM2 and compare the reference signal, measured at point A in Fig. 4, to the filtered first and second sidebands. Figure 5 presents the normalized original signal power and the normalized power of the first and second order sidebands. We can observe a magnification of the sinusoidal modulation overlaid on top of the pulse, this magnification increases as the order of the sideband increases. The normalized reference is raised to the power of $(2m + 1)$ to represent the theoretical prediction of magnification according to Eq. (3). The theoretical calculations of the normalized powers of the first and second order sidebands are presented in dashed lines in Fig. 5 and show good agreement with the experimental results. The discrepancy between the measurement and the prediction appearing in the first sinusoidal peak is explained by the fact that the reference pulse signal does not exhibit a constant peak power, hence when normalized and raised to the $(2m + 1)$ power, it leads to amplitude values below unity.

To prove the $(2m + 1)$ magnification ratio of small signals and faithful linear correspondance between input and output signals, the modulation voltage on the EOM2 is varied, which modulates the magnitude of the sinusoidal signal. To measure the ratio between the output signal contrast and the input signal contrast, $\kappa = \rho_{out}/\rho_{in}$, the modulation voltage is reduced from 2V to 50mV by

Optics EXPRESS

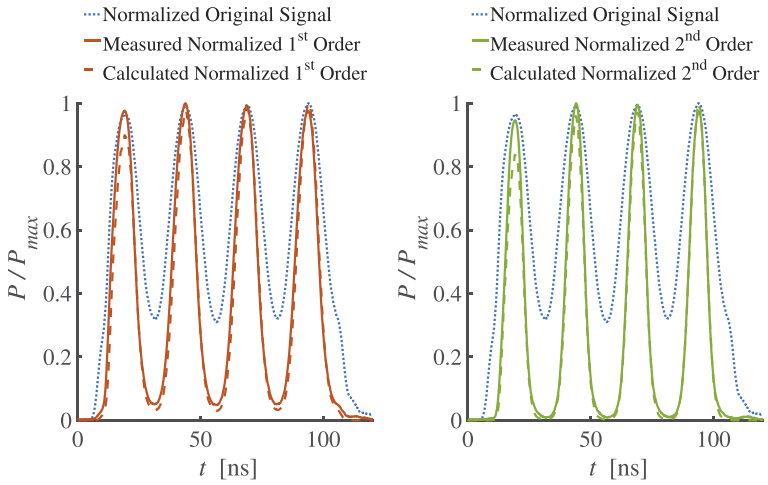

Fig. 5. Experimental measurement and theoretical approximation of a normalized reference signal and its magnification of first and second order.

halving the value at each step. Figures 6(a) and 6(b) respectively present the original normalized signal power for a 50 mV modulation voltage and the normalized second order sideband signal power showing a magnification by a factor of 5. Figure 6(c) presents the variation of κ as a function of the signal modulation voltage for the first and second order sideband. The contrast between the second trough and the third peak (see Fig. 5) is chosen to calculate the contrast ratio

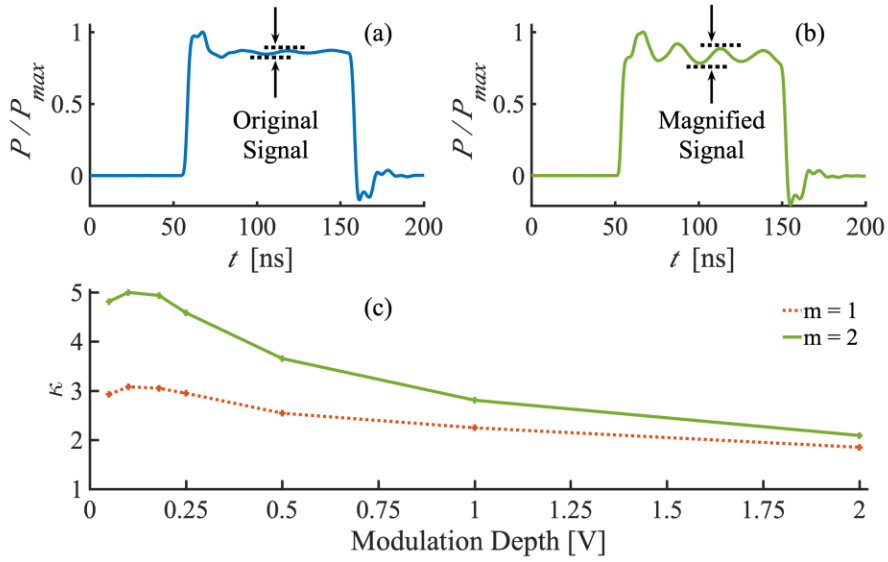

Fig. 6. Measurement of the magnification of small intensity fluctuations. a) Measured normalized original signal with a modulation depth of 50 mV, b) measured normalized 2^{nd} order sideband signal, c) ratios between of the output and input signal's contrast as a function of the modulation depth of the sinusoidal signal on EOM2.

Optics EXPRESS

to avoid the leading and falling edge pulse dynamics imposed by the function generator. We observe that the measurements in the small-signal regime are in agreement with the predicted $(2m + 1)$ value of amplification given by Eq. (5) as they respectively saturate at values of 3 and 5 for the first and second order sidebands. For ϕ_{SPM} values within the linear regression regime in Fig. 3, the magnification value increases with m, and the setup can be cascaded to achieve any magnification value. This opens the way to enhance the sensitivity of intensity based sensors as will be demonstrated in future works.

4. Conclusion

We present a new approach for the magnification of small optical signals by impressing them onto an SMOS undergoing self-phase modulation. The all-optical magnification process allows for magnification by a factor $(2m + 1)$ for the m^{th} order SPM-generated sideband of small optical signals. Magnification of signals with a modulation depth between 50 and 180 mV have been measured to undergo a contrast magnification of respectively 3 and 5 for the first and second order sidebands, in accordance with theoretical predictions. This all-optical signal magnification technique will allow for enhanced point sensing capabilities by bringing small signals of interest within the range of detection of conventional photodetectors.

Funding

Natural Sciences and Engineering Research Council of Canada (7RGPIN-2015-06071); Canada Research Chairs (950-231352).

References

1. B. J. Luff, J. S. Wilkinson, J. Piehler, U. Hollenbach, J. Ingenhoff, and N. Fabricius, "Integrated optical Mach-Zehnder biosensor," J. Lightwave Technol. **16**(4), 583–592 (1998).
2. L. V. Nguyen, D. Hwang, S. Moon, D. S. Moon, and Y. Chung, "High temperature fiber sensor with high sensitivity based on core diameter mismatch," Opt. Express **16**(15), 11369 (2008).
3. P. Lu, L. Men, K. Sooley, and Q. Chen, "Tapered fiber Mach–Zehnder interferometer for simultaneous measurement of refractive index and temperature," Appl. Phys. Lett. **94**(13), 131110 (2009).
4. L. Li, L. Xia, Z. Xie, and D. Liu, "All-fiber Mach-Zehnder interferometers for sensing applications," Opt. Express **20**(10), 11109 (2012).
5. P. V. Mamyshev, "All-optical data regeneration based on self-phase modulation effect," in *24th European Conference on Optical Communication*, vol. 1, (1998), pp. 475–476.
6. M. Matsumoto, "Performance analysis and comparison of optical 3r regenerators utilizing self-phase modulation in fibers," J. Lightwave Technol. **22**(6), 1472–1482 (2004).
7. M. Rochette, L. Fu, V. Ta'eed, D. J. Moss, and B. J. Eggleton, "2r optical regeneration: an all-optical solution for BER improvement," IEEE J. Sel. Top. Quantum Electron. **12**(4), 736–744 (2006).
8. W. Yu, C. Lou, L. Huo, and J. Chen, "A modified SPM-based 2r-regenerator based on an imbalanced nonlinear optical loop mirror," in *Asia Communications and Photonics Conference and Exhibition*, (2010), pp. 130–131.
9. A. E. Willner, S. Khaleghi, M. R. Chitgarha, and O. F. Yilmaz, "All-Optical Signal Processing," J. Lightwave Technol. **32**(4), 660–680 (2014).
10. A. Boskovic, S. V. Chernikov, J. R. Taylor, L. Gruner-Nielsen, and O. A. Levring, "Direct continuous-wave measurement of n_2 in various types of telecommunication fiber at 1.55 μm," Opt. Lett. **21**(24), 1966–1968 (1996).
11. C. Baker, B. Vanus, M. Wuilpart, L. Chen, and X. Bao, "Enhancement of optical pulse extinction-ratio using the nonlinear Kerr effect for phase-OTDR," Opt. Express **24**(17), 19424 (2016).

6.2 Additional comments

Because the Kerr medium used in experiment of the previous manuscript does not allow for the use of CW light without generating Brillouin scattering, a sinusoidal signal is imposed on the peak power of a square pulse before being launched into the Kerr medium. Only sinusoidal signals of up to a few MHz can be generated using our function generator. These signals cannot be placed on top of nanosecond pulses (conventionally used in distributed sensing) if multiple cycles need to be observed, as was the case for our demonstration. Thus, to allow for observing multiple cycles of the sinusoidal signal, the pulse width is extended into the microseconds regime. The pulse widening reduces the amount of amplification provided by the EDFAs present before the Kerr medium to the peak power. This ultimately limits the induced nonlinear phase-shift and explains why only the second order sideband can be generated in the previous manuscript, as opposed to the higher-order sideband generated in Chap. 4.

We also provide an erratum for the last figure of the previous manuscript. Figure 6 in the manuscript does not show the ratio between the contrast of the input and output signals, but rather the ratio between the two signals amplitudes (P_{signal}). The updated figure is shown in Fig. 6.1. The conclusions drawn in the manuscript remain identical because a magnification factor of $2m + 1$ is still obtained in the small-signals regime, as shown in Fig. 6.1. While the original figure also depicts the magnification of small signals, this updated figure is more in line with the mathematical derivations performed in the manuscript.

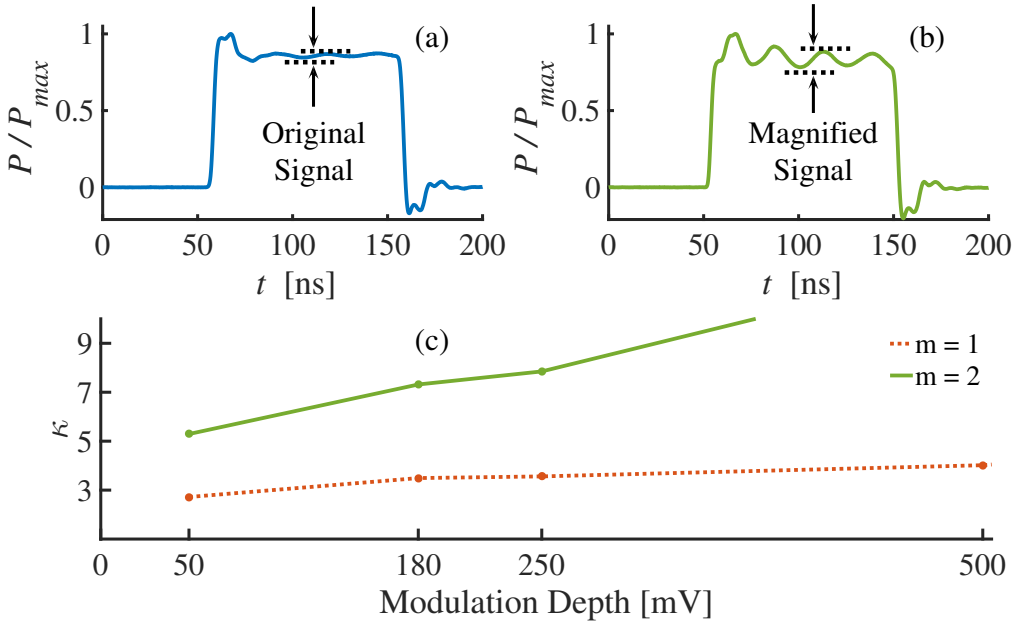

Figure 6.1: Measurement of the magnification of small intensity fluctuations. a) Measured normalized original signal with a modulation depth of 50 mV, b) measured normalized 2^{nd}-order sideband signal, c) ratios between of the output and input signal's contrast as a function of the modulation depth of the sinusoidal signal on EOM2.

Chapter 7

Enhancement of minimum detectable perturbation in intensity-based fiber sensors

The previous chapters have demonstrated that both stabilization and magnification are achievable all-optically by inducing a sinusoidal modulation on a laser signal and extracting a sideband generated after the light experiences self-phase modulation. In this chapter, we demonstrate that both stabilization and magnification can be combined to improve the minimum detectable perturbation of an intensity-based fiber sensor. To visualize the interest of this combination, we recall Eq. 3.14 and Eq. 3.20 which respectively describe the output powers of an MZI-based sensor under strain $\Delta\epsilon$ with stabilized input ($P_{\text{out,S}}\big|_{\Delta\epsilon}$) and magnified output ($P^{(m)}_{\text{out,M}}\big|_{\Delta\epsilon}$):

$$P_{\text{out,S}}\big|_{\Delta\epsilon} = \Omega(1+\eta F)(1+\phi_{d,0}+\phi_{d,0}\theta_\epsilon\Delta\epsilon), \tag{7.1}$$

$$P^{(m)}_{\text{out,M}}\big|_{\Delta\epsilon} = \xi_m\Omega^{2m+1}(1+F)^{2m+1}(1+\phi_{d,0})^{2m}\Big(1+\phi_{d,0}+(2m+1)\phi_{d,0}\theta_\epsilon\Delta\epsilon\Big). \tag{7.2}$$

By analyzing these equations, it quickly become apparent that the intensity noise reduction provided by the factor η in Eq. 7.1 can be combined with the $2m+1$ magnification factor

applied to the external perturbation of Eq. 7.2 to detect weaker environmental perturbations. The following manuscript describes our proposed sensing scheme combining stabilization and magnification applied to a polarimetric sensor under strain.

7.1 Experimental demonstration of fiber-based sensor detection enhancement

Research Article | Vol. 29, No. 20 / 27 Sep 2021 / Optics Express 32114
Optics EXPRESS

All-optical enhancement of minimum detectable perturbation in intensity-based fiber sensors

BENOIT VANUS,* CHAMS BAKER, LIANG CHEN, AND XIAOYI BAO

Department of Physics, University of Ottawa, 25 Templeton Street, Ottawa, Ontario, K1N 1N6, Canada

Abstract: We present a novel optical signal processing scheme for enhancing the minimum detectable environmental perturbation of intensity-based fiber sensors. The light intensity is first stabilized by inducing a sinusoidal intensity modulation and extracting the first-order sideband generated by self-phase modulation (SPM) in a nonlinear medium. The light with stabilized intensity is then sent through a sensor and the sensor induced power variation is magnified by first inducing a sinusoidal intensity modulation, then undergoing SPM, and finally extracting a higher-order sideband. The advantage of the proposed stabilization-magnification (SM) sensing scheme is experimentally demonstrated by applying a damped vibration on an intensity-based fiber sensor and comparing the minimum detectable strain value of the proposed scheme with that of a conventional sensing scheme. Experimental results demonstrate minimum detectable strain improvement by a factor of 3.93. This new SM sensing scheme allows for the detection of perturbations originally too weak to be detected by a given intensity-based fiber sensor, which will be beneficial for a variety of applications such as high frequency ultra-sound detection.

1. Introduction

Over the last few decades, intensity-based optical fiber sensors have been extensively used in the oil and gas industry, for medical diagnostics, and for buildings structural health monitoring [1–8]. One main objective when developing fiber sensors is to detect weak perturbations of environmental variables such as temperature or strain. This is particularly important when detecting ultrasound signals, commonly used for locating and characterizing damages in structures and for medical imaging, since the detected signal amplitude decreases when the frequency increases due to larger attenuation at high ultrasound frequencies [9,10]. Gravitational wave detection using intensity-based sensors also requires measuring extremely small environmental perturbations [11,12].

The detection limit of an intensity-based fiber sensor can first be improved by appropriately choosing and designing the sensor for a targeted application. Interferometric sensors, such as a Mach-Zehnder interferometer (MZI), are commonly utilized intensity-based sensors due to their good low-frequency response and performance across a wide frequency band [13]. The sensitivity of an intensity-based interferometric sensor can be increased by adjusting the length of the interferometer arms [14], coating or etching the sensing fiber [15,16], and operating the sensor at a quadrature point [17]. Second, using an appropriate detection algorithm also allows for improving the fiber-based sensor performance [18], particularly when the sensor is intensity-noise limited [19]. Finally, stabilization of the light source also plays a key role in enhancing the detection limit of a fiber-based sensor. Because most intensity-based sensors are also sensitive to the input signal polarization, a polarization control scheme was proposed to stabilize a laser signal and therefore improve the detection limit [20]. However, the use of control loops on the laser frequency or polarization comes at the expense of the laser intensity and phase noises which limit the minimum detectable environmental perturbation (MDEP).

We have previously demonstrated a proof of concept for all-optical magnification of small environmental perturbations [21]. In an intensity-based sensor, magnification increases the

#441217
Journal © 2021
https://doi.org/10.1364/OE.441217
Received 22 Aug 2021; accepted 13 Sep 2021; published 21 Sep 2021

Optics EXPRESS

environmental perturbation induced power variation ΔP with respect to the initial power P_0 that is measured in the absence of environmental perturbations, leading to an increase in $\Delta P/P_0$. Magnification must be distinguished from amplification which increases both ΔP and P_0 such that $\Delta P/P_0$ remains the same. Magnification is especially practical when $\Delta P \ll P_0$ because it increases ΔP while keeping P_0 below the saturation level of a photodetector, which enables the measurement of the increased ΔP. All-optical magnification can be used for enhancing the MDEP of an intensity-based sensor when the signal noise is mainly contributed by the photodetector. However, to achieve an MDEP enhancement in a general case, the laser intensity at the input of the sensor must be stabilized. Without the stabilization step, the intensity noise of the laser will be magnified and will thus limit the MDEP. Therefore, both the stabilization and magnification steps must be combined to enhance the MDEP in a practical sensing application.

In this paper, we propose and demonstrate the use of self-phase modulation (SPM) to all-optically improve the minimum detectable perturbation of an intensity-based fiber sensor using a novel stabilization-magnification (SM) sensing scheme. First, we derive a theoretical prediction of the minimum detectable strain provided by our proposed scheme and compare it with the minimum detectable strain of a conventional sensing scheme. Then, we present an experimental setup for measuring a damped vibration of a cantilever using our SM scheme and a conventional sensing scheme, and compare the results from both sensing schemes to demonstrate an enhancement of 3.93 in minimum strain detection by our SM scheme. Finally, we discuss the prospect and limitations of our novel sensing scheme.

2. Minimum detectable strain improvement by SM sensing

Figure 1 shows a conceptual schematic of an SM sensing scheme where the output power of the laser is expressed as $P_{\mathrm{L}} = P + \delta P$, with P being the mean output power, and δP being the variation of power around P. The light intensity is first stabilized and the power after stabilization is expressed as $P_{\mathrm{S}} = P + \eta\delta P$, with η being the power fluctuation reduction factor. The intensity-stabilized light is then sent to an intensity-based interferometric sensor whose transfer function is sinusoidal, as shown in Fig. 2. The transfer function of an interferometric intensity-based sensor is given by

$$P_{\mathrm{out}} = P_{\mathrm{in}}\alpha \cos^2\left(\frac{\phi_d}{2}\right) \tag{1}$$

where P_{out} is the sensor output power, P_{in} is the power entering the sensor, α is the attenuation factor, and ϕ_d is the phase difference between the optical paths of the interferometer. Using the linear approximation for small phase-shift variations when operating at a quadrature point, illustrated by the dashed green line in Fig. 2, the output power becomes

$$P_{\mathrm{out}} = \frac{1}{2}P_{\mathrm{in}}\alpha\left[1 + \sin\left(\Delta\phi_d\right)\right] \approx \frac{1}{2}P_{\mathrm{in}}\alpha\left(1 + \Delta\phi_d\right) \tag{2}$$

for $|\Delta\phi_d|<0.1$, where $\phi_d = \Delta\phi_d \pm (\pi/2) + 2l\pi$, with l being an integer. An expression of the output power of the sensor with a stabilized input power is obtained from Eq. (2) by replacing P_{in} with P_{S} leading to

$$P_{\mathrm{out,S}} = \Omega(1 + \eta F)(1 + \Delta\phi_d), \tag{3}$$

where $F = \delta P/P$ and $\Omega = 0.5\alpha P$.

The sensor output power is magnified by imposing a sinusoidal intensity modulation and extracting a sideband generated after the light experiences SPM in a nonlinear Kerr medium [21]. The general expression for the power evolution of an SPM-generated sideband of order m is given

Optics EXPRESS

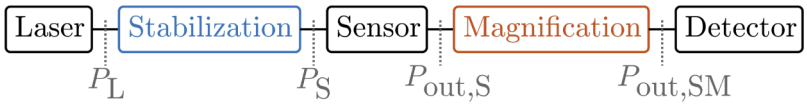

Fig. 1. Conceptual schematic of a stabilization-magnification sensing scheme

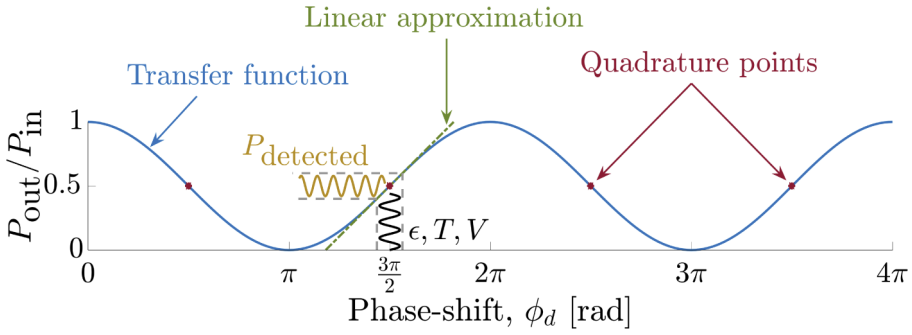

Fig. 2. Transfer function of an interferometric intensity-based sensor, with P_{out} the output power of the sensor, P_{in} the input power, and ϕ_d the phase-shift induced by strain ϵ, temperature T or voltage V changes applied on the sensor.

by

$$P^{(m)}\left(\phi_{\mathrm{SPM}}\right) = \frac{1}{4}P_p\left[J_m^2\left(\frac{\phi_{\mathrm{SPM}}}{2}\right) + J_{m+1}^2\left(\frac{\phi_{\mathrm{SPM}}}{2}\right)\right], \tag{4}$$

where the accumulated nonlinear phase-shift is $\phi_{\mathrm{SPM}} = P_p\gamma L$, with P_p being the signal peak power, γ being the waveguide nonlinear parameter, and L being the length of the nonlinear Kerr medium [22]. In the magnification regime, the amount of nonlinear phase-shift experienced by the light remains small and allows for approximating the Bessel functions in Eq. (4) with $J_m\left(\phi_{\mathrm{SPM}}/2\right) \sim \left(\phi_{\mathrm{SPM}}/4\right)^m/(m!)$. This asymptotic approximation is valid for $0<\phi_{\mathrm{SPM}} \ll 2\sqrt{m+1}$, which comprises the magnification regime.

The output power of the SM sensing scheme using the m^{th}-order sideband applied to an interferometric intensity-based sensor is

$$P_{\mathrm{out,SM}}^{(m)} = \xi_m\Omega^{2m+1}\left(1+\eta F\right)^{2m+1}\left(1+\Delta\phi_d\right)^{2m+1}, \tag{5}$$

with $\xi_m = (0.25)^{2m+1}\,(m!)^{-2}\,(\gamma L)^{2m}$. When the sensor is subjected to an external strain $\Delta\epsilon$, the phase difference between the optical paths becomes $\phi_d\big|_{\Delta\epsilon} = \phi_{d,0} + \Delta\phi_{d,\Delta\epsilon} + 2l\pi$, where $\phi_{d,0}$ is the initial phase difference between the interferometer optical paths and is equal to $\pm(\pi/2)$ at the quadrature points, and $\Delta\phi_{d,\Delta\epsilon}$ is the phase difference variation induced by the applied strain. The induced phase variation is directly related to the applied strain by $\Delta\phi_{d,\Delta\epsilon} = \phi_{d,0}\theta_\epsilon\Delta\epsilon$, where $\theta_\epsilon = \left(\partial n_d/\partial\epsilon\right)n_d^{-1} + \left(\partial L_s/\partial\epsilon\right)L_s^{-1}$, with L_s being the length of the sensor, and n_d being the refractive index difference between the sensor optical paths. Similar relationships between the induced phase difference and the applied external strain can be found for the majority of interferometric intensity-based fiber sensors [23–25], and this proportionality is well established in the field. The output power at the m^{th}-order sideband of the SM scheme is

$$P_{\mathrm{out,SM}}^{(m)}\big|_{\Delta\epsilon} = \xi_m\Omega^{2m+1}\left(1+\eta F\right)^{2m+1}\Big(1+(2m+1)\,0.5\pi\theta_\epsilon\Delta\epsilon\Big), \tag{6}$$

and the generated output power variation induced by $\Delta\epsilon$ is

$$\Delta P_{\mathrm{out,SM}}^{(m)}\big|_{\Delta\epsilon} = \xi_m\Omega^{2m+1}\left(1+\eta F\right)^{2m+1}(2m+1)\,0.5\pi\theta_\epsilon\Delta\epsilon. \tag{7}$$

Optics EXPRESS

After the magnification stage, the optical signal is converted into an electrical signal by a photodetector, and then acquired using an oscilloscope. The voltage measured at the oscilloscope is $V_{\text{out}} = G_D P + N_D + N_O$, where G_D is the detector conversion factor, P is the optical power, N_D and N_O are the noises of the detector and the oscilloscope, respectively. Using the approximation $(1+\eta F)^{2m+1} \approx 1 + (2m+1)\eta F$ when $\eta F \ll 1$ in Eq. (6), and defining $A_0 = 0.5\pi\theta_\epsilon$, the measured voltage at the oscilloscope in the SM sensing system when strain is applied on the sensor is

$$V_{\text{out,SM}}\big|_{\Delta P} = G_D \xi_m \Omega^{2m+1} \Big(1 + (2m+1)\,\eta F + (2m+1)\,A_0 \Delta\epsilon + (2m+1)^2\,\eta F A_0 \Delta\epsilon \Big) + N_D + N_O. \tag{8}$$

Similarly, the measured voltage in a conventional sensing scheme using a similar sensor under identical strain conditions is

$$V_{\text{out,C}}\big|_{\Delta P} = G_D \Omega \,(1 + F + A_0 \Delta\epsilon + F A_0 \Delta\epsilon) + N_D + N_O. \tag{9}$$

The minimum detectable strain of the SM sensing scheme, $\Delta\epsilon_{\text{min,SM}}$, is obtained by equating the signal and the noise contributions in Eq. (8) leading to

$$\Delta\epsilon_{\text{min,SM}} = \frac{1}{0.5\pi\theta_\epsilon \Big(1 - (2m+1)\,\eta F\Big)} \left(\eta F + \frac{N_{\text{SM,r}}}{2m+1} \right), \tag{10}$$

where $V_{0,\text{SM}} = G_D \xi_m \Omega^{2m+1}$ is the initial voltage in the absence of strain, and $N_{\text{SM,r}} = (N_D + N_O)/V_{0,\text{SM}}$ is the relative detection noise. Similarly, the minimum detectable strain of a conventional sensing system is

$$\Delta\epsilon_{\text{min,C}} = \frac{1}{0.5\pi\theta_\epsilon\,(1-F)} \left(F + N_{\text{C,r}} \right). \tag{11}$$

where $V_{0,\text{C}} = G_D \Omega$, and $N_{\text{C,r}} = (N_D + N_O)/V_{0,\text{C}}$. A comparison between minimum detectable strain values of conventional and SM sensing schemes can be performed when their respective initial voltage values are equal, $V_{0,\text{C}} = V_{0,\text{SM}}$. The minimum detectable strain improvement provided by the SM sensing scheme in comparison to the conventional scheme is

$$\Gamma_\epsilon = \frac{\Delta\epsilon_{\text{min,C}}}{\Delta\epsilon_{\text{min,SM}}} = \frac{1 - (2m+1)\eta F}{1 - F} \left(\frac{F + N_{\text{C,r}}}{\eta F + \frac{N_{\text{SM,r}}}{2m+1}} \right). \tag{12}$$

Based on the first factor of Eq. (12), m and η must satisfy the condition $(2m+1)\eta \leq 1$ to avoid magnifying the initial laser amplitude noise. Based on the second factor of Eq. (12), reducing η improves the minimum detectable strain by reducing the impact of the laser intensity noise, and increasing the extracted sideband order m improves the minimum detectable strain by reducing the impact of the detection noise.

3. Experimental setup

Figure 3 presents a schematic of the experimental setup used for demonstrating the enhancement in minimum strain detection provided by the SM sensing scheme compared to a conventional sensing scheme when using an interferometric intensity-based fiber sensor. The setup contains a reference branch representing the conventional sensing scheme and an SM sensing branch, shown with a dashed purple line and a solid black line, respectively. For reliable comparison, identical polarimetric sensors (PSs) are utilized in both schemes, and each PS contains a 20-cm

Optics EXPRESS

long polarization-maintaining (PM) fiber acting as a fiber under test (FUT). The PS behaves similar to an intensity-based interferometric sensor with each principal polarization axis of the PM FUT acting as an arm of the interferometer. Both PM FUTs are glued on a thin metallic cantilever, depicted by the grey rectangle in Fig. 3. One end of the cantilever is fixed to the optical table, while the other end is free, and thus applying a force on the free-end deforms the cantilever and induces identical strain on both sensors, which allows for reliable comparison.

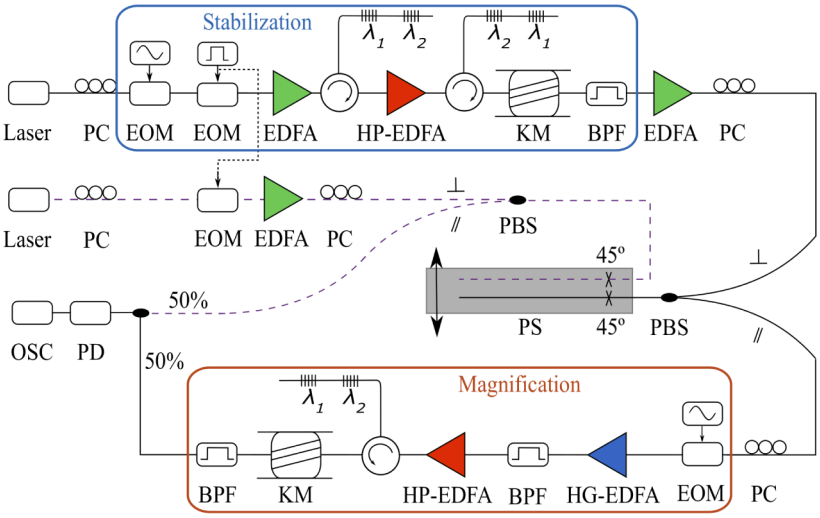

Fig. 3. Schematic of the experimental setup. BPF: Band-Pass Filter, EDFA: Erbium-Doped Fiber Amplifier, EOM: Electro-Optical Modulator, HG-EDFA: High-gain EDFA, HP-EDFA: High-power EDFA, KM: Kerr Medium, OSC: Oscilloscope, PBS: Polarization Beam Splitter, PC: Polarization Controller, PD: Photodiode, PS: Polarimetric Sensor.

The configuration of a conventional polarimetric sensor is shown in Fig. 4(a). A laser light is launched into a polarization controller (PC) which aligns the light polarization with the perpendicular axis of a fiber-coupled polarization beam splitter (PBS, from Thorlabs). The PBS, which is connected with polarization-maintaining (PM) fibers, decomposes the light into two orthogonally polarized components, respectively referred to as perpendicular $\perp$ and parallel $/\!/$ polarizations. Polarized light exiting the PBS by the common port passes to a second PC that aligns the laser light at 45° from the the principal axes of the PM sensing fiber that acts as an FUT. The 45° incident angle allows the power of the polarized light at the input of the FUT to split evenly between the FUT principal polarization axes. The light at the output of the FUT propagates to a second fiber-coupled PBS through a PC that ensures the light from each principal polarization axis of the FUT reaches the PBS at a 45° angle. As a result, half the power propagating from each principal polarization axis of the FUT is projected onto the parallel axis of the PBS, which causes light interference. The power of the interference signal is then converted to an electrical signal using a photodetector (PD) and the electrical signal is measured by an oscilloscope (OSC).

Figure 4(b) presents a schematic of the polarimetric sensor configuration used in this experiment. The configuration in Fig. 4(b) differs from the classical polarimetric sensor in Fig. 4(a) by the Fresnel reflection and by the 45°-splice utilized instead of a PC, but both configurations are effectively equivalent. The Fresnel reflection from the end of the FUT makes it possible to use a single PBS instead of the two required in the conventional configuration. Moreover, the laser light passes twice through the FUT making the effective sensing length twice as long as that in a conventional configuration. Finally, the 45-degree splices are created by a commercial

Optics EXPRESS

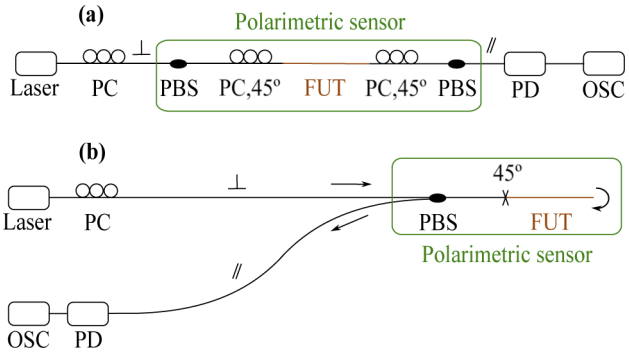

Fig. 4. Schematic of (a) a conventional polarimetric sensor, (b) the polarimetric sensor used in our experimental setup presented in Fig. 3. The ⊥ and // signs refer to the perpendicular and parallel axes of the polarization beam splitter, respectively. FUT: Fiber Under Test, OSC: Oscilloscope, PBS: Polarization Beam Splitter, PC,45°: Polarization Controller aligned at 45°, PD: Photodetector.

fiber-splicer and do not change over time, which makes them preferable to the PCs in the conventional configuration. The transmission spectrum of this polarimetric sensor, presented by the blue line in Fig. 5, is obtained by sending amplified spontaneous emission (ASE) noise from an erbium-doped fiber amplifier (EDFA) to the input and calculating the ratio between the output and the input spectra. The central wavelength of the laser is tuned to match the quadrature point of the polarimetric sensor, as shown by the red line in Fig. 5.

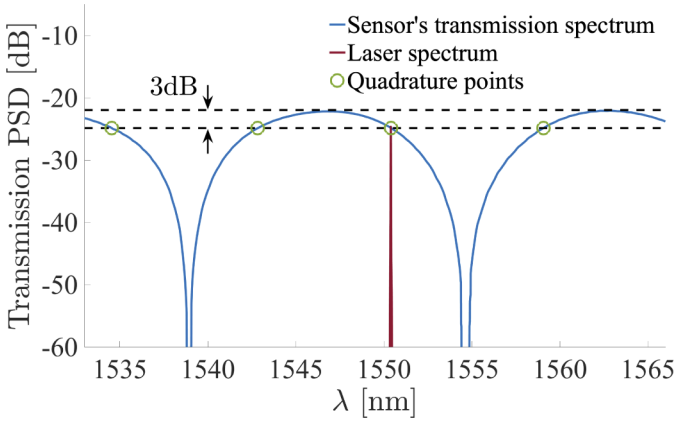

Fig. 5. Measured transmission spectrum of the polarimetric sensor that is utilized in this experiment. Also presented is the measured laser spectrum, shown in red, which is aligned with the quadrature point of the polarimetric sensor. PSD: Power Spectral Density

In the SM sensing branch of the setup presented in Fig. 3, a tuneable laser (HP 81980A) generates a coherent continuous light at 1550.196 nm, which is tuned such that the wavelength of the first-order SPM-generated sideband is aligned with the quadrature point of the polarimetric sensor. The light first passes through an electro-optic modulator (EOM, OC-192) driven by a radio frequency source (HP 83752A) applying an 8.825 GHz sinusoidal intensity modulation. The light is then pulse-modulated by a second EOM (OC-192) driven by a function generator (Tektronix AFG 3252) to create a 10 ns wide pulse with a 1 kHz repetition rate. The pulsed light is then amplified by an EDFA (Amonics AEDFA-PA-25-B-FA) before being filtered by a

Optics EXPRESS

dual-grating filter with central wavelengths tuned to the sinusoidally-modulated laser wavelengths (λ_1 = 1550.110 nm and λ_2 = 1550.268 nm). The power of the pulse is then boosted by a high-power EDFA (Amonics AEDFA-33) and filtered again by an inverted version of the same dual-grating filter before entering a 2-km long dispersion-shifted fiber acting as a Kerr medium. Sidebands are generated at the output of the Kerr medium as the sinusoidally-modulated pulse experiences SPM [22], and the first-order sideband is extracted using a band-pass filter (BPF, Teraxion TFC-C-Band). To stabilize the pulse peak power intensity, the amount of amplification is adjusted to achieve $\phi_{\mathrm{SPM}}/1$ rad = 6.4 dB [26]. The intensity-stabilized pulse is then amplified by an EDFA (Amonics AEDFA-PA-25-B-FA) and the light polarization is aligned with the input of the polarimetric sensor using a PC. The output of the polarimetric sensor enters an EOM that is sinusoidally-driven with an 8.825 GHz modulation frequency (OC-192 with HP 8673D driver). The sensor output is then amplified by a high-gain EDFA (Amonics APEDFA-C-10-B-FA) and filtered by a BPF (Newport OSP-9100). A second step of amplification and filtration is applied using a high-power EDFA (Amonics AEDFA-C-30B-B-FA) and a dual-grating filter (λ_1 = 1550.332 nm and λ_2 = 1550.470 nm) before the signal reaches a second Kerr medium, composed of 6-km long dispersion-shifted fiber. Optical sidebands are generated by SPM and the second-order sideband is extracted using a BPF (Teraxion TFC-C-Band). The peak power of the pulse at the input of the second Kerr medium is adjusted to align with the signal magnification regime [21].

The reference branch of the setup is composed of a tuneable laser (Agilent 81940A) emitting light at 1555.689 nm. The light is pulse-shaped using an EOM (JDSU 10020461) driven by the second output of the same function generator that is utilized to create the pulse in the SM branch to ensure both SM and reference pulses are synchronized and aligned for comparison. The generated pulse is amplified by an EDFA (Amonics AEDFA-PA-25-B-FA) and sent through a polarimetric sensor that is effectively identical to the one in the SM branch.

The reference and SM signals are combined when reaching the 50-50 fiber coupler but do not interfere due to a time delay imposed on the reference signal by the function generator. The signals are finally detected using a low-noise photodetector (New Focus 1811- IR DC 125MHz) and the generated electrical signal is captured using an oscilloscope (LeCroy 64Xi-A). Detection of the signals from both branches using the same photodiode and oscilloscope makes the detection noises identical and allows for reliable comparison of both schemes.

4. Results and discussion

To compare the minimum detectable strain of the SM and conventional sensing schemes, a damped vibration is induced on the sensors by applying and suddenly releasing a force on the free-end of the cantilever. The vibrational deformation of the cantilever induces an equal strain on the FUTs of both sensors and the resulting signal amplitude changes are measured at the oscilloscope. The solid blue and red traces in Fig. 6 respectively show the measured initial output signals from the SM and reference schemes in the absence of vibrations. The peaks of these initial signals, representing $V_{0,\mathrm{SM}}$ and $V_{0,\mathrm{C}}$, are made equal so that the detected vibration amplitudes can be reliably compared. The dashed blue and red traces in Fig. 6 respectively show the vibration-induced amplitude changes of the SM and reference signals when subjected to the same vibration. The vibration profile is obtained by tracking the evolution of the peak amplitude of the SM and reference signals over time.

Figure 7 presents the measured damped vibration from the SM and the conventional schemes relative to $V_{0,\mathrm{SM}}$ and $V_{0,\mathrm{C}}$, respectively. As the vibration dampens, the conventional signal becomes buried in the noise while the SM signal can still be detected, therefore showing an increased minimum detectable strain. The signal-to-noise ratios are $\mathrm{SNR_C} = \Delta V_{\mathrm{out,C}}/N_{\mathrm{C}} = \alpha_{\mathrm{C}}\Delta\epsilon/N_{\mathrm{C}}$ for the conventional scheme and $\mathrm{SNR_{SM}} = \Delta V_{\mathrm{out,SM}}/N_{\mathrm{SM}} = \alpha_{\mathrm{SM}}\Delta\epsilon/N_{\mathrm{SM}}$ for the SM scheme, where α_{C} and α_{SM} are the strain-to-voltage conversion factors for the conventional and the SM schemes,

Optics EXPRESS

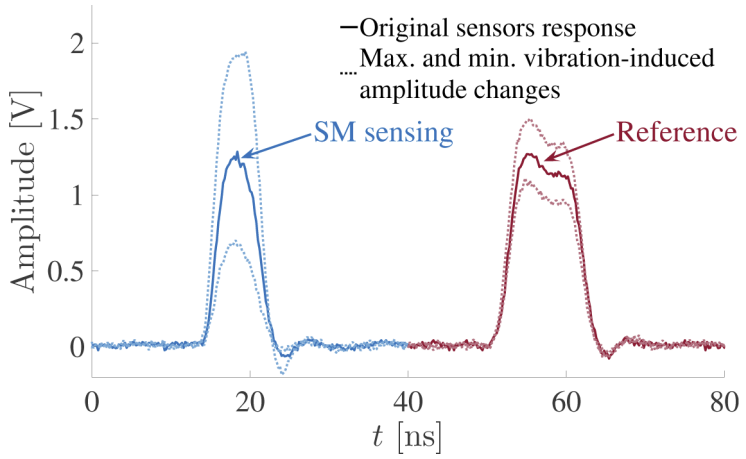

Fig. 6. Continuous oscilloscope trace recording the SM and reference sensors outputs, respectively in blue and red, and their respective amplitude changes under a given applied vibration.

and N_C and N_{SM} are the noise levels of the conventional and SM schemes, respectively. The value of $\Delta\epsilon_{min,C} = N_C/\alpha_C$ is obtained by setting $SNR_C = 1$, and the value of $\Delta\epsilon_{min,SM} = N_{SM}/\alpha_{SM}$ is obtained by setting $SNR_{SM} = 1$, which leads to an enhancement in the minimum detectable strain $\Gamma_\epsilon = \Delta\epsilon_{min,C}/\Delta\epsilon_{min,SM} = (\alpha_{SM}/\alpha_C)(N_C/N_{SM})$. Using $\Delta V_{out,C} = \alpha_C\Delta\epsilon$ and $\Delta V_{out,SM} = \alpha_{SM}\Delta\epsilon$, leads to $\alpha_{SM}/\alpha_C = \Delta V_{out,SM}/\Delta V_{out,C}$ at a non-zero value of $\Delta\epsilon$, and by reference to Fig. 7, the measured ratio is $\alpha_{SM}/\alpha_C = 4.65$. The measured peak-to-peak noise amplitudes in the SM and reference branches are 0.13 V, 0.11 V, respectively, leading to $N_C/N_{SM} = 0.85$. Therefore, the measured enhancement in the minimum detectable strain is $\Gamma_\epsilon = (\alpha_{SM}/\alpha_C)(N_C/N_{SM}) = 4.65 \times .85 = 3.93$, which is comparable to the value of 4.40 predicted by Eq. (12) using $F = 0.3\,\%$, $N_{C,r} = 7.9\,\%$, and $N_{SM,r} = 9.3\,\%$. The discrepancy can be attributed to the difference between the FUT lengths, the time jitter of the electronic equipment, and the imperfect alignment of the lasers and dual-grating filters with the quadrature points of the sensors.

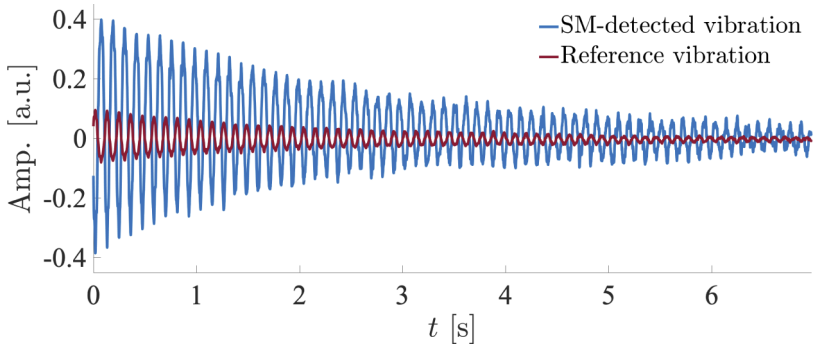

Fig. 7. Relative amplitude variation of the peak power from each sensor output under identical damped vibration.

The FUT length of the polarimetric sensors is selected to be relatively short, 20 cm, for reduced sensitivity and increased difficulty of detecting weaker signals, to better highlight the effectiveness of the proposed SM scheme. The FUTs in the SM and the conventional schemes are made from the same fiber and their lengths are equal within 2 millimeters, and hence, the

Optics EXPRESS

intrinsic sensitivity of these sensors is effectively identical. We do not measure the absolute value of the strain because our focus is on measuring the enhancement of the minimum detectable strain by our SM scheme in comparison to a conventional scheme, which is possible because the two sensors are effectively identical, subjected to the same external vibration, and an identical average peak power reaches the photodetector connected to the oscilloscope.

The bandwidth limit of our SM scheme depends on the nonlinear Kerr effect which has a response time on the order of femtoseconds. The frequency of the sinusoidal intensity modulation may limit the maximum detectable vibration frequency, but this parameter can be tuned according the desired application by using appropriate modulators and dual-grating filters. The detection of ultra-high vibration frequencies also requires using CW light instead of pulsed light. Currently, our proposed sensing scheme utilizes pulses because available Kerr media can not generate enough SPM when CW light is utilized due to the rise of stimulated Brillouin scattering (SBS). Indeed, SBS decreases the amount of induced nonlinear phase shift as most of the signal power passing through the nonlinear Kerr medium is transferred to the SBS Stoke's frequency. We are currently working to develop an approach that allows for the suppression of SBS to enable the implementation of the proposed SM scheme using a CW laser instead of laser pulses.

The minimum detectable strain can be further enhanced by cascading multiple stabilization steps prior to the sensor and multiple magnifications steps at the detection end. The minimum detectable strain enhancement of an SM sensing scheme composed of N stabilization steps and M magnification steps is given by

$$\Gamma_{\epsilon}^{N,M} = \frac{1-\mu HF}{1-F}\left(\frac{F+N_{\mathrm{C,r}}}{HF+\frac{N_{\mathrm{SM,r}}}{\mu}}\right), \tag{13}$$

where $\mu = \prod_{i=1}^{M}(2m_i+1)$ with m_i being the extracted sideband order at the i^{th} magnification step, and $H = \prod_{j=1}^{N}\eta_j$ with η_j being the power fluctuation reduction at the j^{th} stabilization step. The denominator of the second factor in Eq. (13) rapidly tends to 0 as N and M increase, and the minimum detectable strain enhancement tends to infinity providing a theoretically unlimited performance enhancement. In practice however, environmental noises and amplification noises between the magnification stages must also be considered because these noises will get magnified and increase the detection noise floor limiting the minimum detectable strain enhancement. Systems equipped with multiple stabilization and magnification stages, and the impact of environmental noises between the stages will be investigated in future works.

5. Conclusion

We present a novel all-optical approach based on self-phase modulation for enhancing the minimum detectable strain of an intensity-based fiber sensor. A detection limit enhancement is achieved by first stabilizing the intensity of the light before reaching the sensor, and then magnifying the sensor induced power fluctuations to overcome detection noises. Experimental results show an enhancement of the minimum detectable vibration amplitude when using a stabilization-magnification sensing scheme over a conventional sensing scheme. This stabilization-magnification sensing approach will allow for detection of environmental parameters previously too weak to be detected using intensity-based sensors, and thus allow for the potential discovery of new physical behaviours.

Funding. Natural Sciences and Engineering Research Council of Canada (7RGPIN-2020-06302); Canada Research Chairs (950-231352).

Disclosures. The authors declare no conflicts of interest.

Data availability. Data underlying the results presented in this paper are not publicly available at this time but may be obtained from the authors upon reasonable request.

Optics EXPRESS

References

1. C. T. M. Doyle, A. R. Martin, M. Q. Wu, T. Liu, S. A. Hayes, D. Brooks, R. A. Badcock, and G. F. Fernando, "Intensity-based optical fiber sensors for condition monitoring of engineering materials," in *Fiber Optic Sensors V*, vol. 2895 (International Society for Optics and Photonics, 1996), pp. 288–299.
2. B. H. Lee, Y. H. Kim, K. S. Park, J. B. Eom, M. J. Kim, B. S. Rho, and H. Y. Choi, "Interferometric Fiber Optic Sensors," Sensors **12**(3), 2467–2486 (2012).
3. F. Liu, X. He, L. Yu, Y. Pan, B. Xie, D. Yi, L. Gu, and M. Zhang, "The Applications of Interferometric Fiber-Optic Sensors in Oilfield," in *2018 Progress in Electromagnetics Research Symposium (PIERS-Toyama)*, (IEEE, Toyama, 2018), pp. 1664–1671.
4. W. H. Png, H. S. Lin, C. H. Pua, and F. A. Rahman, "Pipeline Monitoring and Vibrational Sensing Using Loop Integrated Mach Zehnder Interferometer Optical Fiber Sensor," in *2018 IEEE 7th International Conference on Photonics (ICP)*, (2018), pp. 1–3. ISSN: 2330–5665.
5. J. W. Arkwright, N. G. Blenman, I. D. Underhill, S. A. Maunder, M. M. Szczesniak, P. G. Dinning, and I. J. Cook, "In-vivo demonstration of a high resolution optical fiber manometry catheter for diagnosis of gastrointestinal motility disorders," Opt. Express **17**(6), 4500–4508 (2009).
6. S. Poeggel, D. Tosi, D. Duraibabu, G. Leen, D. McGrath, and E. Lewis, "Optical Fibre Pressure Sensors in Medical Applications," Sensors **15**(7), 17115–17148 (2015).
7. K. Bremer, M. Wollweber, F. Weigand, M. Rahlves, M. Kuhne, R. Helbig, and B. Roth, "Fibre Optic Sensors for the Structural Health Monitoring of Building Structures," Procedia Technol. **26**, 524–529 (2016).
8. D.-H. Kim, B.-Y. Koo, C.-G. Kim, and C.-S. Hong, "Damage detection of composite structures using a stabilized extrinsic Fabry–Perot interferometric sensor system," Smart Mater. Struct. **13**(3), 593–598 (2004).
9. B. Culshaw, G. Thursby, D. Betz, and B. Sorazu, "The Detection of Ultrasound Using Fiber-Optic Sensors," IEEE Sensors J. **8**(7), 1360–1367 (2008).
10. Y. Xu, L. Zhang, S. Gao, P. Lu, S. Mihailov, and X. Bao, "Highly sensitive fiber random-grating-based random laser sensor for ultrasound detection," Opt. Lett. **42**(7), 1353 (2017).
11. D. Reitze, "Chasing gravitational waves," Nat. Photonics **2**(10), 582–585 (2008).
12. G. Gagliardi, M. Salza, S. Avino, P. Ferraro, and P. De Natale, "Probing the Ultimate Limit of Fiber-Optic Strain Sensing," Science **330**(6007), 1081–1084 (2010).
13. W. Png, H. S. Lin, C. H. Pua, J. Lim, S. K. Lim, Y. Lee, and F. Abd-Rahman, "Feasibility use of in-line Mach–Zehnder interferometer optical fibre sensor in lightweight foamed concrete structural beam on curvature sensing and crack monitoring," Struct. Heal. Monit. **17**(5), 1277–1288 (2018).
14. Y. Xie, M. Zhang, and D. Dai, "Design Rule of Mach-Zehnder Interferometer Sensors for Ultra-High Sensitivity," Sensors **20**(9), 2640 (2020).
15. M. Batumalay, S. W. Harun, N. Irawati, H. Ahmad, and H. Arof, "A Study of Relative Humidity Fiber-Optic Sensors," IEEE Sens. J. **15**(3), 1945–1950 (2015).
16. X. Chong, K. Kim, P. R. Ohodnicki, E. Li, C. Chang, and A. X. Wang, "Ultrashort Near-Infrared Fiber-Optic Sensors for Carbon Dioxide Detection," IEEE Sens. J. **15**(9), 5327–5332 (2015).
17. C. Flueraru, H. Kumazaki, S. Sherif, S. Chang, and Y. Mao, "Quadrature Mach–Zehnder interferometer with application in optical coherence tomography," J. Opt. A: Pure Appl. Opt. p. 5 (2007).
18. H. Moradi, F. Hosseinibalam, and S. Hassanzadeh, "Improving the signal-to-noise ratio in a fiber-optic Fabry–Pérot acoustic sensor," Laser Phys. Lett. **16**(6), 065106 (2019).
19. R. C. Rabelo, R. T. d. Carvalho, and J. Blake, "SNR enhancement of intensity noise-limited FOGs," J. Lightwave Technol. **18**(12), 2146–2150 (2000).
20. A. Kersey, M. Marrone, A. Dandridge, and A. Tveten, "Optimization and stabilization of visibility in interferometric fiber-optic sensors using input-polarization control," J. Lightwave Technol. **6**(10), 1599–1609 (1988).
21. B. Vanus, C. Baker, L. Chen, and X. Bao, "All-optical intensity fluctuation magnification using Kerr effect," Opt. Express **28**(3), 3789 (2020).
22. C. Baker, B. Vanus, M. Wuilpart, L. Chen, and X. Bao, "Enhancement of optical pulse extinction-ratio using the nonlinear Kerr effect for phase-OTDR," Opt. Express **24**(17), 19424 (2016).
23. Y. Wang, H. Yuan, X. Liu, Q. Bai, H. Zhang, Y. Gao, and B. Jin, "A Comprehensive Study of Optical Fiber Acoustic Sensing," IEEE Access **7**, 17 (2019).
24. T. R. Woliński, "Polarimetric optical fibers and sensors," in *Progress in Optics*, vol. 40 E. Wolf, ed. (Elsevier, 2000), pp. 1–75.
25. S. Gao, C. Baker, L. Chen, and X. Bao, "High-Sensitivity Temperature and Strain Measurement in Dual-Core Hybrid Tapers," IEEE Photonics Technol. Lett. **30**(12), 1155–1158 (2018).
26. B. Vanus, C. Baker, L. Chen, and X. Bao, "All-optical pulse peak power stabilization and its impact in phase-OTDR vibration detection," OSA Continuum **4**(5), 1430–1436 (2021).

7.2 Additional comments

First, the Fresnel reflection present on one end of the polarimetric sensor used in the manuscript leads to a reduced peak power reaching the input of the Kerr medium placed at the detection end. Therefore, only the second-order sideband was achievable at the magnification stage using our setup. However, in an experiment using a sensor without a high attenuation, higher-order sidebands can be achieved and thus a higher amount of magnification obtained, further improving the interest of our proposed SM sensing scheme.

Second, and as described in the experimental setup, the interrogating tuneable lasers do not operate at the same wavelength. This arises from the fact that the two polarimetric sensors did not exhibit the exact same transfer function. The difference in transfer function also explains why the two polarimetric sensors' amplitude responses are in opposite directions, as can be observed in Fig. 5 of the previous manuscript. The transfer function of the sensor can be obtained by sending ASE noise from an EDFA and calculating the difference between the input light spectrum and the output light spectrum, as shown by the yellow line in Fig. 7.1.

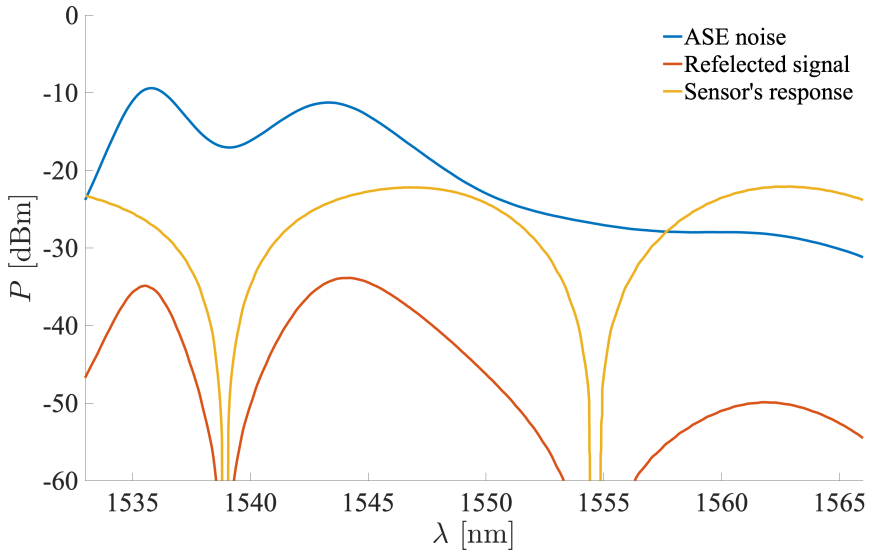

Figure 7.1: Polarimetric sensor's response to ASE noise and cosine-squared transfer function. The ASE noise is presented in blue, the reflected spectrum from the polarimetric sensor is in red, and the sensor's transfer function is shown in yellow.

The two polarimetric sensors' transfer functions are presented in Fig. 7.2, respectively with a solid blue and dashed yellow line. As shown in Fig. 7.2, both sensors' transfer functions have the same wavelength spacing (or oscillation period), which indicates that both sensors are of equal length (within a few millimeters). The comparison performed in the manuscript is thus valid given that their transfer functions have the same period and that the two lasers are aligned with the quadrature points, as shown by the solid red and dashed purple lines in Fig. 7.2. Given the location of the lasers, it becomes clear that if an applied strain induced a shift of the transfer functions to the right, one sensor's amplitude response increases while the other decreases, which is in agreement with Fig. 5 of the previous manuscript. It should also be mentioned that we cannot guarantee the perfect alignment of the laser with the quadrature point of the sensor given that undesired environmental perturbations also modify the transmission spectrum of sensor.

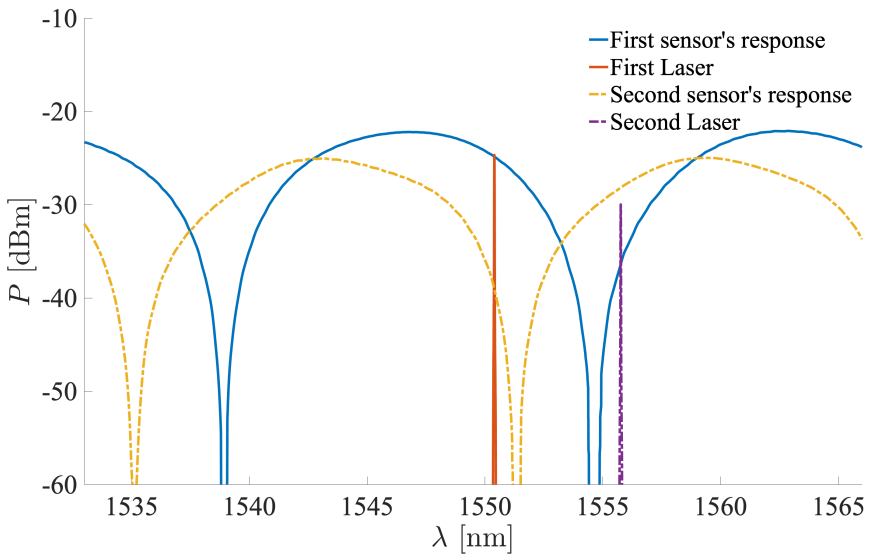

Figure 7.2: Polarimetric sensor's cosine-squared transfer functions and lasers spectra aligned to the quadrature point of their respective sensor. The first sensor's transfer function is shown in solid blue line, and the corresponding laser spectrum is shown in solid red line. The second sensor's transfer function is displayed in dashed yellow line, and the corresponding laser spectrum is shown in dashed purple line.

Chapter 8

Conclusion and Future work

Conclusion

This thesis presents the use of all-optical signal processing based on the nonlinear Kerr effect for fiber sensing applications. We demonstrate that this nonlinear effect allows for significant sensing performance enhancement, and allows for the creation of sensing schemes compatible with existing ones. A general overview of all-optical signal processing is given, as well as a review of fiber point and distributed sensing and their respective limitations. We then derive the impact of self-phase modulation on sinusoidally modulated optical signals and show that multiple regimes of operation can improve fiber sensor limitations.

First, we demonstrate the generation of optical pulses exhibiting a 120-dB extinction ratio, which are measured using a single-photon counter. The use of a single-photon counter is necessary to characterize the pulses' extinction ratio as the noise floor of a photodetector is above the pedestal power of the high-ε pulses, thus making such characterization impossible. The all-optical extinction ratio enhancement provided when a high-order sideband is extracted allows for Φ-OTDR sensing range extension by reducing the background noise present at the photodetector.

Second, we demonstrate the use of the first-order SPM-generated sideband to reduce power fluctuations on a pulse peak power. If the initial power fluctuations are within 1 % of

the average peak power value, our proposed technique reduces power fluctuations by a factor of at least 40. Moreover, we demonstrate the practicality of intensity stabilization in Φ-OTDR by successfully detecting a vibration applied at a 4-km distance when using stabilization, while an identical Φ-OTDR system without stabilization is not capable of detecting said vibration.

Third, all-optical magnification of signal power fluctuations is achieved when a sideband is extracted at the output of the Kerr medium, after an SMOS undergoes experiences SPM, and kept within the so-called linear regime of the optical transfer function. We demonstrated that a $2m+1$ magnification factor can be obtained for small signals located on top of the peak power of an optical square pulse, when extracting the m^{th}-order SPM-generated sideband.

Finally, after demonstrating all-optical intensity stabilization in distributed fiber sensing and a proof-of-concept for all-optical signal magnification, we prove that, when combined, they allow for the enhancement of the minimum detectable environmental perturbations. We compare our proposed stabilization-magnification sensing scheme to a regular sensing scheme when detecting an amplitude-dampening vibration using a polarimetric sensor. We experimentally demonstrate that the minimum detectable perturbation is enhanced when using our proposed scheme. We also discuss the possibilities and capabilities of minimum perturbation detection improvement provided by cascading several stabilization steps before the sensor and several magnification steps at the detection end. This sensing scheme could be used in environments where the detection of extremely small environmental perturbation is crucial, for example in gravitational wave detection or in high frequency ultra-sound detection.

Future work

The first future investigation based on the presented work could be a deeper dive into high extinction ratio pulses generation. When generating optical pulses with a high extinction ratio using our setup, a pulse narrowing effect also occurs, as can be observed in Fig. 8.1 where an initial 5-ns pulse is narrowed to ∼2 ns when extracting the 6$^{\text{th}}$-order sideband.

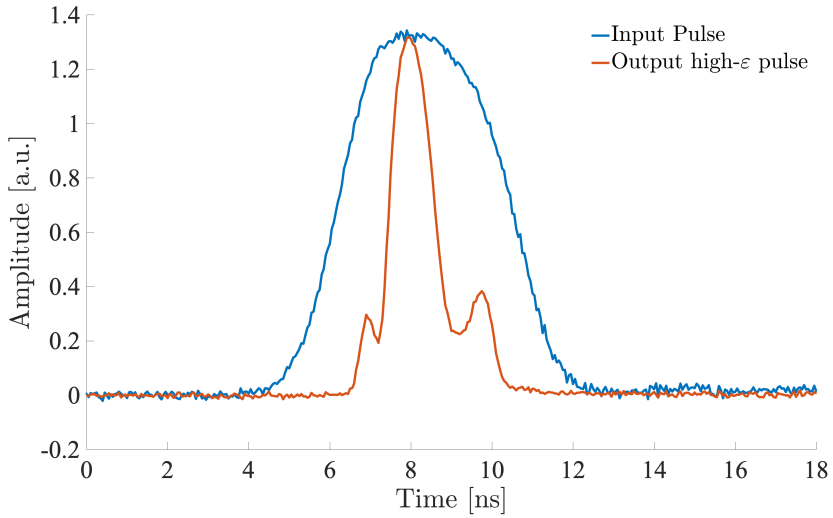

Figure 8.1: Pulse shrinking induced by an SMOS undergoing the nonlinear Kerr effect. The 6$^{\text{th}}$-order SPM-generated sideband is extracted with a 5 ns input pulse width. The input pulse is shown in blue and the output pulse is shown red.

In a conventional OTDR or Φ-OTDR setup, pulses narrower than 10 ns are rarely used, especially if they do not exhibit a high extinction ratio. Indeed, the amount of backscattering signal generated by the pulse peak power is not sufficient to detect small amplitude perturbations, as those perturbations remain buried in the background noise generated by the pulse's pedestal power, as shown in Fig. 3.7(d). However, the generation of high-ε pulses allows us, so far, to detect events at a 10-km distance with an effective 2-ns pulse width using a conventional direct-detection scheme. This could be further improved and a frequency analysis of the backscattering signal could also be performed in order to determine the impact of the high-frequencies, generated during pulse narrowing, on fiber point and distributed sensing. Another future potential application for high-ε pulses would be to use them on high-Q resonators in sensing application, such as with micro-spheres. Indeed, the very low pedestal

power would eliminate the background noise and allow for the detection of extremely small perturbations.

The second future application of the work performed in this thesis could be to create an intensity-stabilized pulsed laser. A conceptual setup of the latest version of our work on such a laser is presented in Fig. 8.2, where π-shifted grating (ΠSG) acts as a narrow band-pass filter; its presence in the final setup is yet to be determined hence the brackets surrounding it.

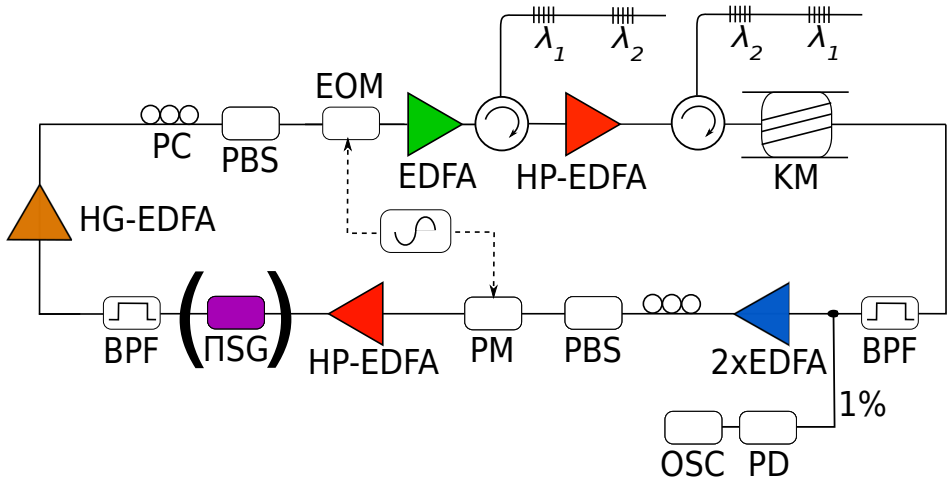

Figure 8.2: Conceptual setup for an intensity-stabilized pulsed laser based on SMOS undergoing the nonlinear Kerr effect. BPF: Band-Pass Filter, EDFA: Erbium-Doped Fiber Amplifier, EOM: Electro-Optical Modulator, HG-EDFA: High-Gain EDFA, HP-EDFA: High-Power EDFA, KM: Kerr Medium, OSC: Oscilloscope, PBS: Polarization Beam Splitter, PC: Polarization Controller, PD: Photodetector, PM: phase-modulator, 2xEDFA: Dual-Stage EDFA, ΠSG: π-shifted fiber-Bragg grating.

We can describe the generation of nanoseconds optical pulses by analyzing the setup starting at the high-gain EDFA (HG-EDFA). The CW signal generated by the HG-EDFA is sinusoidally modulated by the EOM to create an SMOS. The two dual-grating filters placed before the Kerr medium possess the same wavelength spacing and have an identical central frequency, λ_0. The two filters are cascaded to further enhance the sinusoidal modulation depth. The band-pass filter located after the Kerr medium is aligned with the first-order SPM-generated sideband at λ_1. The light passing through the band-pass filter is then am-

plified by a dual-stage EDFA. The central wavelength of the signal is then shifted back to λ_0 using a phase-modulator driven by the same sinusoidal signal as the EOM. After various amplification and filtration steps, the single-frequency signal is again sinusoidally-modulated by the EOM to create an SMOS. By adjusting the gains of the different amplifiers, the stabilization regime provided by the first-order sideband is theoretically achievable. However, our most recent results suggest that while a pulse in the nanosecond regime can be obtained, the intensity stabilization is yet to be reached. Figure 8.3 shows consecutive pulses acquired by the oscilloscope, and as can be observed, amplitude fluctuations and time-jitter are present. Many phenomena can be responsible for these fluctuations, such as polarization dispersion, chromatic dispersion, spectral alignment issues. Our research group is currently investigating a potential key element which could allow for reaching the stabilization regime of the proposed pulsed-laser.

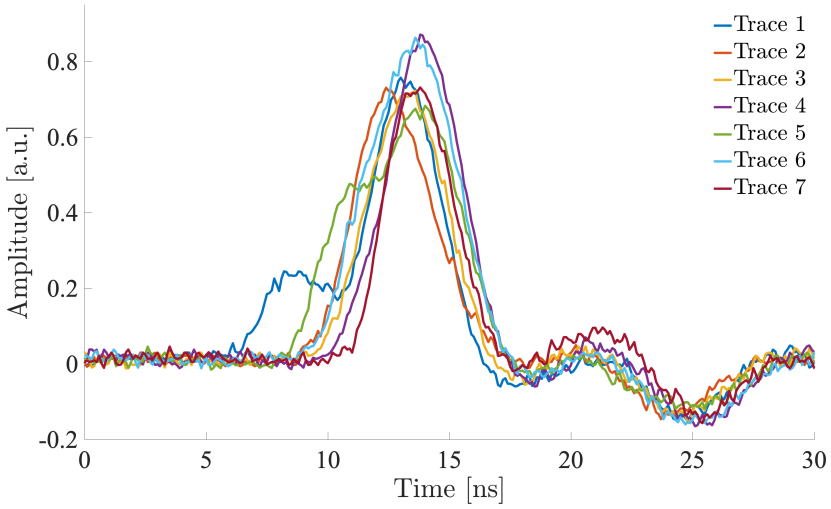

Figure 8.3: Consecutive optical pulses measured at the output of the stabilized pulsed laser presented in Fig. 8.2.

Publications

1. B. Vanus, C. Baker, L. Chen, and X. Bao, "All-optical enhancement of minimum detectable perturbation in intensity-based fiber sensors", *Opt. Express*, Vol. 29, No. 20, 2021.

2. B. Vanus, C. Baker, L. Chen, and X. Bao, "All-optical pulse peak power stabilization and its impact in phase-OTDR vibration detection", *OSA Continuum*, Vol. 4, No. 5, 2021.

3. B. Vanus, C. Baker, L. Chen, and X. Bao, "High extinction ratio optical pulse characterization method via single-photon counting", *App. Optics*, Vol. 60, No. 1, 2020.

4. B. Vanus, C. Baker, L. Chen, and X. Bao, "All-optical intensity fluctuation magnification using Kerr effect", *Opt. Express*, Vol. 28, No. 3, January 2020.

5. C. Baker, B. Vanus, M. Wuilpart, L. Chen, and X. Bao, "Enhancement of optical pulse extinction-ratio using the nonlinear Kerr effect for phase-OTDR", *Opt. Express*, Vol. 24, No. 17, 2016.

6. M. Wuilpart, B.Vanus, A. Andrasan, G. Andrei, P. Moreau, and P. Mégret, "Study of a fibre optics current sensor for the measurement of plasma current in ITER," *Proc. Of SPIE*, Vol. 9916, 2016.

Bibliography

1. Young, T. Experimental demonstration of the general law of the interference of light. *Philosophical Transactions of the Royal Society of London* **94** (1804).
2. Einstein, A. Uber einen die Erzeugung und Verwandlung des Lichtes betreffenden heurischen Gesichtpunkt. *Ann. Phys.* **17** (1905).
3. Franken, P. A., Hill, A. E., Peters, C. W. & Weinreich, G. Generation of Optical Harmonics. *Phys. Rev. Lett.* **7** (1961).
4. Willner, A. E., Khaleghi, S., Chitgarha, M. R. & Yilmaz, O. F. All-Optical Signal Processing. *Journal of Lightwave Technology* **32** (2014).
5. Dat, P. T. *et al.* Transparent Fiber–Radio–Fiber Bridge at 101 GHz using Optical Modulator and Direct Photonic Down-Conversion. *Optical Fiber Conference* (2021).
6. Taylor, J. A. *et al.* Phase noise in the photodetection of ultrashort optical pulses. *IEEE International Frequency Control Symposium* (2010).
7. Pan, Z., Yu, C. & Willner, A. E. Optical performance monitoring for the next generation optical communication networks. *Optical Fiber Technology* **16** (2010).
8. Agrawal, G. P. Nonlinear fiber optics 5th ed. (2013).
9. Wabnitz, S. & Eggleton, B. J. All-Optical Signal Processing (2015).
10. Contestabile, G., Presi, M., Proietti, R., Calabretta, N. & Ciaramella, E. A simple and low-power optical limiter for multi-GHz pulse trains. *Opt. Express* **15** (2007).
11. Chow, K., Shu, C., Lin, C. & Bjarklev, A. All-optical wavelength multicasting with extinction ratio enhancement using pump-modulated four-wave mixing in a dispersion-flattened nonlinear photonic crystal fiber. *IEEE Journal of Selected Topics in Quantum Electronics* **12** (2006).
12. Saruwatari, M. All-optical signal processing for terabit/second optical transmission. *IEEE Journal of Selected Topics in Quantum Electronics* **6** (2000).
13. Kuo, B. P., Chui, P. C. & Wong, K. K. All-Optical Tunable Delay With NRZ-to-RZ Format Conversion Capability Based on Optical Kerr Switch and Pulse Pre-Chirping. *Journal of Lightwave Technology* **26** (2008).
14. Santagiustina, M., Chin, S., Primerov, N., Ursini, L. & Thévenaz, L. All-optical signal processing using dynamic Brillouin gratings. *Sci Rep* **3** (2013).
15. Zhu, Z., Gauthier, D. J. & Boyd, R. W. Stored Light in an Optical Fiber via Stimulated Brillouin Scattering. *Science* **318** (2007).

16. Matsumoto, M. Performance analysis and comparison of optical 3R regenerators utilizing self-phase modulation in fibers. *Journal of Lightwave Technology* **22** (2004).

17. Mamyshev, P. V. All-optical data regeneration based on self-phase modulation effect. *24th European Conference on Optical Communication* **1** (1998).

18. Boscolo, S., Audo, F., Fatome, J. & Finot, C. Nonlinear spectral compression in optical fiber: A new tool for processing degraded signals. *19th International Conference on Transparent Optical Networks* (2017).

19. Taira, K. & Kikuchi, K. Picosecond pulse generation with high extinction ratio employing electroabsorption modulator, fibre compressor, and self-phase-modulation-based pulse reshaper. *Electronics Letters* **40** (2004).

20. Merlier, J. D. *et al.* Experimental demonstration of 15 dB extinction ratio improvement in a new 2R optical regenerator based on an MMI-SOA. *Proceedings 27th European Conference on Optical Communication* **4** (2001).

21. Yu, W., Lou, C., Huo, L. & Chen, J. A modified SPM-based 2R-regenerator based on an imbalanced nonlinear optical loop mirror. *Asia Communications and Photonics Conference and Exhibition* (2010).

22. Wang, A. *et al.* Optical fiber sensors for harsh environments. *International Conference on Sensors and Control Techniques* **4077** (2000).

23. Mihailov, S. J. Fiber Bragg Grating Sensors for Harsh Environments. *Sensors* **12** (2012).

24. Zinsou, R. *et al.* Recent Progress in the Performance Enhancement of Phase-Sensitive OTDR Vibration Sensing Systems. *Sensors* **19** (2019).

25. Yan, Q. *et al.* Distributed Vibration Sensing System for Oil and Gas Pipelines Based on COTDR and BP Neural Network. *26th International Conference on Optical Fiber Sensors* (2018).

26. Choi, K. N., Juarez, J. C. & Taylor, H. F. Distributed fiber optic pressure/seismic sensor for low-cost monitoring of long perimeters. *AeroSense* (2003).

27. Arkwright, J. W. *et al.* In-vivo demonstration of a high resolution optical fiber manometry catheter for diagnosis of gastrointestinal motility disorders. *Opt. Express, OE* **17** (2009).

28. Dong, S., Liao, Y. & Tian, Q. Intensity-based optical fiber sensor for monitoring corrosion of aluminum alloys. *Appl. Opt.* **44** (2005).

29. Bao, X., Leeson, J., Snoddy, J. & Chen, L. *Optical Fiber New Developments* (2009).

30. Bao, X. & Chen, L. Recent Progress in Distributed Fiber Optic Sensors. *Sensors* **12** (2012).

31. Smith, J., Brown, A., DeMerchant, M. & Bao, X. Simultaneous distributed strain and temperature measurement. *Appl. Opt.* **38** (1999).

32. Gao, S., Baker, C., Chen, L. & Bao, X. High-Sensitivity Temperature and Strain Measurement in Dual-Core Hybrid Tapers. *IEEE Photonics Technology Letters* **30** (2018).

33. Chen, C. *et al.* Sensitivity of photonic crystal fiber modes to temperature, strain and external refractive index. *Opt. Express* **16** (2008).

34. Becker, T., Ziemann, O., Engelbrecht, R. & Schmauss, B. Optical Strain Measurement with Step-Index Polymer Optical Fiber Based on the Phase Measurement of an Intensity-Modulated Signal. *Sensors* **18** (2018).

35. Forghieri, F., Tkach, R. W. & Chraplyvy, A. R. *Optical Fiber Telecommunications IIIA (Third Edition)* Third Edition (1997).

36. Singh, S. & Singh, N. Nonlinear effects in optical fibers: Origin, management and applications. *Progress in Electromagnetics Research-pier* **73** (2007).

37. Gonzalez-Herraez, M. & Sylvestre, T. *Advanced Fiber Optics* (2011).

38. Armstrong, J. A. Theory of Interferometric Analysis of Laser Phase Noise. *Journal of the Optical Society of America* **56** (1966).

39. Fan, X., Koshikiya, Y. & Ito, F. Phase-noise-compensated optical frequency domain reflectometry with measurement range beyond laser coherence length realized using concatenative reference method. *Optics Letters* **32** (2007).

40. Fock, L.-S., Kwan, A. & Tucker, R. Reduction of semiconductor laser intensity noise by feedforward compensation: experiment and theory. *J. Lightwave Technol.* **10** (1992).

41. Li, C. *et al.* All-optical frequency and intensity noise suppression of single-frequency fiber laser. *Opt. Lett.* **40** (2015).

42. Drever, R. W. P. *et al.* Laser phase and frequency stabilization using an optical resonator. *Appl. Phys. B* **31** (1983).

43. Yuan, Q., Wang, F., Liu, T., Zhang, Y. & Zhang, X. Using an Auxiliary Mach–Zehnder Interferometer to Compensate for the Influence of Laser-Frequency-Drift in Φ-OTDR. *IEEE Photonics Journal* **11** (2019).

44. Zhao, R. *et al.* Frequency drift mitigation of Φ-OTDR using difference-fitting method. *Appl. Opt.* **60** (2021).

45. Souza, K. D. Significance of coherent Rayleigh noise in fibre-optic distributed temperature sensing based on spontaneous Brillouin scattering. *Meas. Sci. Technol.* **17** (2006).

46. Martins, H. F. *et al.* Coherent Noise Reduction in High Visibility Phase-Sensitive Optical Time Domain Reflectometer for Distributed Sensing of Ultrasonic Waves. *Journal of Lightwave Technology* **31** (2013).

47. Afshar V., S., Ferrier, G. A., Bao, X. & Chen, L. Effect of the finite extinction ratio of an electro-optic modulator on the performance of distributed probe-pump Brillouin sensorsystems. *Optics Letters* **28** (2003).

48. Iribas, H. *et al.* Effects of pump pulse extinction ratio in Brillouin optical time-domain analysis sensors. *Optics Express* **25** (2017).

49. Du, J. & He, Z. Sensitivity enhanced strain and temperature measurements based on FBG and frequency chirp magnification. *Optics express* **21** (2013).

50. Du, J., Li, L., Fan, X., Liu, Q. & He, Z. Sensitivity Enhancement for Fiber Bragg Grating Sensors by Four Wave Mixing. *Photonics* **2** (2015).

51. Du, J. *et al.* Improving fiber optic sensing by all-optical signal processing. *Optoelectronics Global Conference* (2015).
52. Uyar, F. *et al.* A Direct Detection Fiber Optic Distributed Acoustic Sensor With a Mean SNR of 7.3 dB at 102.7 km. *IEEE Photonics J.* **11** (2019).
53. Gerrard, A. & Burch, J. Introduction to Matrix Methods in Optics John Wiley & Sons, Ltd. (1975).
54. Krohn, D. A., MacDougall, T. & Mendez, A. Fiber optic sensors: fundamentals and applications 4. ed. *SPIE PM* **247** (2014).
55. Lu, P., Men, L., Sooley, K. & Chen, Q. Tapered fiber Mach–Zehnder interferometer for simultaneous measurement of refractive index and temperature. *Appl. Phys. Lett.* **94** (2009).
56. Black, R. J. & Moslehi, B. High Temperature Fiber Bragg Gratings for Spacecraft Application. *26th International Conference on Optical Fiber Sensors* (2018).
57. Aldaba, A. L. *et al.* Microstructured optical fiber sensor for soil moisture measurements. *26th International Conference on Optical Fiber Sensors* (2018).
58. Yin, S., Ruffin, P. & Yu, F. Fiber Optic Sensors (2017).
59. Onoufriou, A., Kalli, K. & Kohnke, G. Fiber Bragg Gratings: Fundamentals and Applications in Telecommunications and Sensing. *Physics Today* **53** (2000).
60. Thévenaz, L. Advanced Fiber Optics: Concepts and Technologies 1st (2011).
61. Hill, K. O., Fujii, Y., Johnson, D. C. & Kawasaki, B. S. Photosensitivity in optical fiber waveguides: Application to reflection filter fabrication. *Applied Physics Letters* **32** (1978).
62. Li, L., Xia, L., Xie, Z. & Liu, D. All-fiber Mach-Zehnder interferometers for sensing applications. *Opt. Express* **20** (2012).
63. Hui, R. & O'Sullivan, M. *Fiber Optic Measurement Techniques* (Boston, 2009).
64. Hui, R. *Introduction to Fiber-Optic Communications* (2020).
65. Kaminow, I. Polarization in optical fibers. *IEEE Journal of Quantum Electronics* **17** (1981).
66. Woliński, T. R., Lesiak, P. & Domański, A. W. Polarimetric optical fiber sensors of a new generation for industrial applications. *Bulletin of the Polish Academy of Sciences Technical Sciences* (2008).
67. Yataki, M. S., Payne, D. N. & Varnham, M. P. All-fibre polarising beamsplitter. *Electronics Letters* **21** (1985).
68. Yokohama, I., Okamoto, K. & Noda, J. Fibre-optic polarising beam splitter employing birefringent-fibre coupler. *Electronics Letters* **21** (1985).
69. Perrin, F. Polarization of Light Scattered by Isotropic Opalescent Media. *The Journal of Chemical Physics* **10** (1942).
70. Bohren, C. F. & Huffman, D. R. Absorption and Scattering of Light by Small Particles (2008).

71. Jones, R. C. A New Calculus for the Treatment of Optical SystemsI. Description and Discussion of the Calculus. *J. Opt. Soc. Am.* **31** (1941).

72. Parke, N. G. Optical Algebra. *Journal of Mathematics and Physics* **28** (1949).

73. Cedilnik, G., Hunt, R. & Lees, G. Advances in Train and Rail Monitoring with DAS. *26th International Conference on Optical Fiber Sensors* (2018).

74. Filograno, Riziotis & Kandyla. A Low-Cost Phase-OTDR System for Structural Health Monitoring: Design and Instrumentation. *Instruments* **3** (2019).

75. Beisenova, A., Issatayeva, A., Molardi, C., Dukenbayev, K. & Tosi, D. Distributed Fiber Optic Strain-Sensing Catheter for Assisted Delivery of Epidural Anesthesia. *26th International Conference on Optical Fiber Sensors* (2018).

76. Bao, X., Zhou, D.-P., Baker, C. & Chen, L. Recent Development in the Distributed Fiber Optic Acoustic and Ultrasonic Detection. *Journal of Lightwave Technology* **35** (2017).

77. Awwad, E. *et al.* Large Bandwidth Phase-Sensitive DAS with Novel Polarization-Multiplexed Probing Technique. *26th International Conference on Optical Fiber Sensors* (2018).

78. Wang, Y. *et al.* A Comprehensive Study of Optical Fiber Acoustic Sensing. *IEEE Access* **7** (2019).

79. Dong, Y., Chen, L. & Bao, X. High-Spatial-Resolution Time-Domain Simultaneous Strain and Temperature Sensor Using Brillouin Scattering and Birefringence in a Polarization-Maintaining Fiber. *IEEE Photonics Technology Letters* **22** (2010).

80. Dong, Y., Chen, L. & Bao, X. Time-division multiplexing-based BOTDA over 100km sensing length. *Optics Letters* **36** (2011).

81. Yang, Z., Soto, M. A. & Thévenaz, L. 200 km fiber-loop Brillouin distributed fiber sensor using bipolar Golay codes and a three-tone probe. *24th International Conference on Optical Fibre Sensors* **9634** (2015).

82. Fu, Y. *et al.* 175km repeaterless BOTDA with hybrid 2nd- and 3rd- order Raman random fiber laser amplification. *26th International Conference on Optical Fiber Sensors* (2018).

83. Hecht, E. Optics 5 ed (2017).

84. Juarez, J. C. & Taylor, H. F. Distributed fiber optic intrusion sensor system for monitoring long perimeters (2005).

85. Gifford, D., Soller, B., Wolfe, M. & Froggatt, M. Distributed fiber-optic temperature sensing using Rayleigh backscatter. *31st European Conference on Optical Communication* **3** (2005).

86. Hill, W., Kübler, J. & Fromme, M. Single-mode distributed temperature sensing using OFDR. *Fourth European Workshop on Optical Fibre Sensors* **7653** (2010).

87. Koyamada, Y., Imahama, M., Kubota, K. & Hogari, K. Fiber-Optic Distributed Strain and Temperature Sensing With Very High Measurand Resolution Over Long Range Using Coherent OTDR. *Journal of Lightwave Technology* **27** (2009).

88. Masoudi, A., Belal, M. & Newson, T. P. A distributed optical fibre dynamic strain sensor based on phase-OTDR. *Meas. Sci. Technol.* **24** (2013).

89. Zhang, Z. & Bao, X. Continuous and Damped Vibration Detection Based on Fiber Diversity Detection Sensor by Rayleigh Backscattering. *Journal of Lightwave Technology* **26** (2008).

90. Zhang, Z. & Bao, X. Distributed optical fiber vibration sensor based on spectrum analysis of Polarization-OTDR system. *Opt. Express* **16** (2008).

91. Iizuka, K. Elements of Photonics (2002).

92. Hui, R. & O'Sullivan, M. S. Fiber optic measurement techniques (2009).

93. Bao, X. & Wang, Y. Recent Advancements in Rayleigh Scattering-Based Distributed Fiber Sensors. *Advanced Devices & Instrumentation* **2021** (2021).

94. Agrawal, G. P. Fiber-optic communication systems (2002).

95. Brinkmeyer, E. Analysis of the backscattering method for single-mode optical fibers. *Journal of the Optical Society of America* **70** (1980).

96. Derickson, D. Fiber optic test and measurement (1998).

97. Wójcik, A. Signal statistics of phase dependent optical time domain reflectometry (2007).

98. Taylor, H. F. & Lee, C. E. US5194847A (1993).

99. Juarez, J. C. & Taylor, H. F. Field test of a distributed fiber-optic intrusion sensor system for long perimeters. *Appl. Opt.* **46** (2007).

100. Seo, W. Fiber Optic Intrusion Sensor Investigation. PhD thesis (Texas A&M University., 1994).

101. Ren, M., Lu, P., Chen, L. & Bao, X. Theoretical and Experimental Analysis of O-OTDR Based on Polarization Diversity Detection. *IEEE Photonics Technology Letters* **28** (2016).

102. Putra, A. W. S., Yamada, M., Tsuda, H. & Ambran, S. Theoretical Analysis of Noise in Erbium Doped Fiber Amplifier. *IEEE Journal of Quantum Electronics* **53** (2017).

103. Lu, X. & Krebber, K. Characterizing detection noise in phase-sensitive optical time domain reflectometry. *Opt. Express* **29** (2021).

104. Lu, Y., Zhu, T., Chen, L. & Bao, X. Distributed Vibration Sensor Based on Coherent Detection of Phase-OTDR. *Journal of Lightwave Technology* **28** (2010).

105. He, X. *et al.* Phase-sensitive optical time-domain reflectometry with heterodyne demodulation (2017).

106. Yang, S., Zou, W., Long, X. & Chen, J. Pulse-compression optical time domain reflectometer (2014).

107. Lu, B. *et al.* Pulse compression phase sensitive optical time domain reflectometer with sub-meter resolution (2017).

108. Lu, B. *et al.* High spatial resolution phase-sensitive optical time domain reflectometer with a frequency-swept pulse. *Optics Letters* **42** (2017).

109. Strickland, D. & Mourou, G. Compression of amplified chirped optical pulses. *Optics Communications* **55** (1985).

110. Pastor-Graells, J. *et al.* SNR enhancement in high-resolution phase-sensitive OTDR systems using chirped pulse amplification concepts. *Opt. Lett.* **42** (2017).

111. Fan Zhu, Yixin Zhang, Lan Xia, Xuelin Wu & Xuping Zhang. Improved Φ-OTDR Sensing System for High-Precision Dynamic Strain Measurement Based on Ultra-Weak Fiber Bragg Grating Array. *Journal of Lightwave Technology* **33** (2015).

112. Wang, C. *et al.* Distributed OTDR-interferometric sensing network with identical ultra-weak fiber Bragg gratings. *Optics Express* **23** (2015).

113. Ren, M., Zhou, D.-P., Chen, L. & Bao, X. Influence of finite extinction ratio on performance of phase-sensitive optical time-domain reflectometry. *Optics Express* **24** (2016).

114. Morsali, A., Lecler, S., Pelletier, P. M. & Pfeiffer, P. Significance of high extinction ratio laser pulse generation in coherent optical time domain reflectometry. *Optical Sensing and Detection VI* (2020).

115. Snoddy, J., Li, Y., Ravet, F. & Bao, X. Stabilization of electro-optic modulator bias voltage drift using a lock-in amplifier and a proportional-integral-derivative controller in a distributed Brillouin sensor system. *Appl. Opt.* **46** (2007).

116. Li, Z. *et al.* Enhanced phase stability in passive analog photonic links with coherent Rayleigh noise reduction. *Opt. Express* **23** (2015).

117. Shimizu, K., Horiguchi, T. & Koyamada, Y. Characteristics and reduction of coherent fading noise in Rayleigh backscattering measurement for optical fibers and components. *Journal of Lightwave Technology* **10** (1992).

118. Baker, C., Vanus, B., Wuilpart, M., Chen, L. & Bao, X. Enhancement of optical pulse extinction-ratio using the nonlinear Kerr effect for phase-OTDR. *Optics Express* **24** (2016).

119. Stolen, R. H. & Lin, C. Self-phase-modulation in silica optical fibers. *Phys. Rev. A* **17** (1978).

120. Finot, C. & Fatome, J. Experimental demonstration of an ultrafast all-optical bit-error indicating scheme. *Microw. Opt. Technol. Lett.* **53** (2011).

121. Finot, C. & Fatome, J. All-optical fiber-based ultrafast amplitude jitter magnifier. *Opt. Express* **18** (2010).

122. Baker, C. & Bao, X. Displacement sensor based on Kerr induced phase-modulation of orthogonally polarized sinusoidal optical signals. *Optics Express* **22** (2014).

123. Lu, Y., Baker, C., Chen, L. & Bao, X. Chromatic-Dispersion Monitor Based on a Differential Phase-Shift Method Using a Kerr Phase-Interrogator. *IEEE Photonics Journal* **7** (2015).

124. Lu, Y., Baker, C., Chen, L. & Bao, X. Group-Delay-Based Temperature Sensing in Linearly-Chirped Fiber Bragg Gratings Using a Kerr Phase-Interrogator. *Journal of Lightwave Technology* **33** (2015).

125. Boskovic, A., Chernikov, S. V., Taylor, J. R., Gruner-Nielsen, L. & Levring, O. A. Direct continuous-wave measurement of n_2 in various types of telecommunication fiber at 1.55 μm. *Optics Letters* **21** (1996).

126. Dandridge, A., Tveten, A. & Giallorenzi, T. Homodyne demodulation scheme for fiber optic sensors using phase generated carrier. *IEEE Journal of Quantum Electronics* **18** (1982).

127. Spano, P., Piazzolla, S. & Tamburrini, M. Phase noise in semiconductor lasers: A theoretical approach. *IEEE Journal of Quantum Electronics* **19** (1983).

128. Daino, B., Spano, P., Tamburrini, M. & Piazzolla, S. Phase noise and spectral line shape in semiconductor lasers. *IEEE Journal of Quantum Electronics* **19** (1983).

129. Shao, Y. *et al.* Distributed Vibration Sensor With Laser Phase-Noise Immunity by Phase-Extraction φ-OTDR. *Photonic Sens* **9** (2019).

130. Pastor-Graells, J. *et al.* Impact of the laser phase noise on chirped-pulse phase-sensitive OTDR. *25th Optical Fiber Sensors Conference* (2017).

131. Uyar, F. *et al.* 94.8 km-Range Direct Detection Fiber Optic Distributed Acoustic Sensor. *Conference on Lasers and Electro-Optics* (2019).

132. Domdei, N. *et al.* Ultra-high contrast retinal display system for single photoreceptor psychophysics. *Biomedical Optics Express* **9** (2018).

133. Kanno, A., Honda, S., Yamanaka, R., Sotobayashi, H. & Kawanishi, T. Ultrafast and broadband frequency chirp signal generation using a high-extinction-ratio optical modulator. *Opt. Lett.* **35** (2010).

134. Hadfield, R. H. Single-photon detectors for optical quantum information applications. *Nature Photonics* **3** (2009).

135. Cova, S., Longoni, A. & Andreoni, A. Towards picosecond resolution with single-photon avalanche diodes. *Review of Scientific Instruments* **52** (1981).

136. Ribordyt, G., Guinnard, O., Stuckis, D., Wegmullers, M. & Zbindens, H. Photon counting at telecom wavelengths with commercial InGaAslInP avalanche photodiodes: current performance (2009).

137. Morton, G. A. *Advances in Electronics and Electron Physics* (1952).

138. Ripamonti, G., Ghioni, M. & Vanoli, S. Photon timing OTDR: a multiphoton backscattered pulse approach. *Electronics Letters* **26** (1990).

139. Eraerds, P., Legre, M., Zhang, J., Zbinden, H. & Gisin, N. Photon Counting OTDR: Advantages and Limitations. *Journal of Lightwave Technology* **28** (2010).

140. Wegmuller, M., Scholder, F. & Gisin, N. Photon-Counting OTDR for Local Birefringence and Fault Analysis in the Metro Environment. *Journal of Lightwave Technology* **22** (2004).

141. Voisin, V., Caucheteur, C., Kinet, D., Megret, P. & Wuilpart, M. Self-Referenced Photon Counting OTDR Technique for Quasi-Distributed Fiber Bragg Gratings Sensors. *IEEE Sensors Journal* **12** (2012).